

Università degli studi di Milano Bicocca

Dipartimento di Fisica "Giuseppe Occhialini"

Corso di Laurea magistrale in Fisica



Development of superconductive qubits for resonant cavities

Supervisor:
Prof. Andrea Giachero

Candidate:
Emanuele Palumbo

External supervisor:
Dr. Claudio Gatti

Student Number:
825945

Co-supervisor:
Dr. Marco Faverzani

Phone Number:
+39 3382198067

Co-supervisor:
Dott. Danilo Labranca

ACADEMIC YEAR: 2022/2023

GRADUATION SESSION: 20 MARCH 2024

Development of superconductive qubits for resonant cavities

Emanuele Palumbo

Abstract

The qubit, short for quantum bit, is the basic unit of information storage and processing in quantum systems. It consists of a two-level system that exists in a superposition of states 0 and 1 simultaneously. The optimization of these devices makes a significant contribution to the field of quantum sensing, in which qubits act as extremely sensitive sensors used in fundamental physics research. In particular, this work is part of the Qub-IT project, which aims to develop a microwave single-photon counter for the search for light dark matter.

The specific type of qubit used is the superconducting qubit, constructed from superconducting materials and operated at extremely low temperatures. We analyze a precise superconductive qubit called transmon qubit, known for its relatively long coherence times, which are crucial for performing quantum operations accurately. The transmon qubit is composed of two conductive pads coupled with a Josephson junction. This configuration forms an anharmonic oscillator, enabling the isolation of the two-level system. Despite their advantages, transmon qubits are still susceptible to various sources of noise and decoherence, such as electromagnetic losses due to interactions with the environment. These losses contribute to the decrease of the qubit coherence time, particularly the relaxation time T_1 .

The aim of this work is to develop a design of a transmon qubit that minimizes electromagnetic losses and therefore maximizes the coherence of the qubit when it is coupled with a resonant cavity. As a starting point, we conduct a complete characterization of a transmon qubit produced at the Technology Innovation Institute in Abu Dhabi coupled with a 3D resonant cavity. This is performed with a transmon spectroscopy and a time domain characterization, from which we extract the principal parameters describing the system such as the capacity between the pads $C^{exp} = 46 \pm 5$ fF, the critical current of the junction $I_0^{exp} = 25 \pm 1$ nA, the qubit-cavity coupling $g_{01}^{exp}/2\pi = 93 \pm 1$ MHz and the lifetime $T_1^{exp} = 8.7 \pm 0.7$ μ s.

Exploiting electromagnetic simulations, it is possible to provide quantitative estimations of the losses experienced. These electromagnetic losses are described by the sum of the participation ratios contributions from different spatial regions. We compare the results of the experimental analysis with electromagnetic simulations using the ANSYS simulation software, from which we estimate the principal parameters: the pads capacity $C^{sim} = 56$ fF, the qubit-cavity coupling $g_{01}^{sim}/2\pi = 97$ MHz and the lifetime $T_1^{sim} = 42$ μ s. The simulations results indicated a good match for the capacity and coupling, while the lifetime appeared to be overestimated, possibly due to limitations in the numerical mesh resolution of the simulations.

However, this is a promising result that allows us to study different transmon designs to improve its performances. The next steps involve modifying the shape and size of the pads composing the qubit, starting with the Abu Dhabi qubit geometry, which features rectangular pads of dimensions $144 \times 556 \mu\text{m}^2$. We adjust the parameters describing the rectangular geometry and explore other simple geometric shapes of the pads with different parameters, aiming to estimate the electromagnetic losses and find the design that minimizes them. A geometry with two circular pads of radius $500 \mu\text{m}$ is selected. The larger dimensions of the pads allow for a greater distribution of the electromagnetic field, resulting in a significant reduction in losses. The new design present a simulated loss $P_{(\text{new})} = 0.3 \cdot P_{(\text{Abu-Dhabi})}$ and a simulated lifetime of $T_{1(\text{new})}^{\text{sim}} = 63 \mu\text{s}$. This design is used to fabricate new devices at the CNR-IFN in Rome.

The development of the qubit is also carried out preparing the experimental setup for the characterization of the Josephson junctions. In particular, we extract the critical current of four junctions produced at the CNR-IFN in Rome through direct current measurements. The estimated values are of the order of few μA for all the junctions. The same measurement is made for two qubits fabricated with the new design developed in this work.

Publication list:

Some of the contents of this thesis may also be found in the following publication:

D'Elia A., Alfakes B., Alkhazaleh A., Banchi L., Beretta M. M., Carrazza S., Chiarello F., Di
Gioacchino D., Giachero A., Henric F., Piedjou Komnang A. S., Ligi C., Maccarrone G.,
Macucci M., **Palumbo E.**, Pasquale A., Piersanti L., Ravaux F., Rettaroli A., Robbiati M.,
Tocci S., Gatti C. (2024).

**“Characterization of a Transmon Qubit in a 3D Cavity for Quantum Machine
Learning and Photon Counting”**

Applied Science.

DOI: <https://doi.org/10.3390/app14041478>.

Contents

1	Introduction	9
2	Theory	11
2.1	Josephson junction	11
2.1.1	The Josephson equations	12
2.1.2	I-V characteristic	13
2.1.3	Resistively and capacitively shunted Josephson junction (RCSJ)	14
2.1.4	Titled-washboard model	17
2.2	Qubit	19
2.2.1	Quantization of a LC circuit	19
2.2.2	The transmon qubit	21
2.2.3	Block sphere	25
2.3	Resonant cavity	26
2.3.1	Cavity 1D	27
2.3.2	Rectangular 3D cavity	29
2.3.3	Quality factor	31
2.4	Coupling of a transmon qubit and a cavity in dispersive regime . . .	32
2.4.1	Capacity matrix	37
2.4.2	Coupling strength	39
2.5	Qubit driving	40
2.5.1	Dynamics of a driven qubit	40
2.5.2	Dynamics in presence of dissipation	43
2.5.3	Loss participation ratios	45
2.6	Scattering parameters	47
2.7	Devices Fabrication	48
2.7.1	Josephson junctions fabricated at CNR-IFN.	49
2.7.2	Transmon qubit fabricated at TII in Abu-Dhabi	51
2.7.3	Transmon qubit fabricated at CNR-IFN	53
3	Disegn qubit 3D	55
3.1	Simulation Design	55
3.2	Qubit Simulation in Resonant Cavity	56

3.3	Loss qubit optimization and circular design	61
3.3.1	Pad Geometries	61
3.3.2	Designs analysis	62
3.3.3	Circular design	66
3.3.4	Mesh resolution	67
4	Measurement	71
4.1	Cryogenics	71
4.1.1	Dilution refrigerator operation	71
4.1.2	Cryostat	72
4.2	Transmon qubit characterization	72
4.2.1	Experimental setup	73
4.2.2	Transmon spectroscopy characterization	75
4.2.3	Time domain transmon characterization	78
4.3	DC characterization of Josephson junctions	84
4.4	DC characterization of the circular qubit	89
5	Conclusion	93
	Bibliography	95

Chapter 1

Introduction

Quantum sensing is one of the most interesting fields of research in recent years. Quantum sensors can achieve sensitivity levels far beyond those of classical sensors and provide measurements with extremely high precision. This allows for the detection of very weak signals with relevant applications in fundamental research.

The main component of quantum sensing is the qubit, short for quantum bit, the basic unit of information storage and processing in a quantum system. It is a two-level system that exists in a superposition of states 0 and 1 simultaneously. The most widely used qubits are the superconducting qubits, known for their coherence and scalability properties [1]. They exhibit long coherence times, meaning they can maintain their quantum states for relatively long periods, crucial for making measurements over extended periods without losing quantum information. Superconducting qubits are also relatively easy to manufacture and scale up because they are compatible with existing semiconductor fabrication techniques.

The most promising superconducting qubit in terms of performance and simplicity of design is the transmon qubit. It is composed of two conductive pads coupled with a Josephson junction, a superconducting device used for many applications like microwave photon detection [2–4]. This configuration forms an anharmonic oscillator, enabling the isolation of the two-level system[5]. The best performance of a transmon in terms of coherence time is $T_1 = 500 \mu s$ [6]. Despite their good performance, transmon qubits are still susceptible to various sources of noise and decoherence, such as electromagnetic losses due to interactions with the environment, which contribute to the decrease of the qubit coherence time.

In this thesis, we analyzed the data of characterization measurements of a transmon qubit produced at the Technology Innovation Institute in Abu Dhabi coupled with a 3D resonant cavity. We investigated the loss mechanisms and found a method to give a quantitative estimation of the principal parameters of a qubit, using electromagnetic simulations with ANSYS simulation software. The next step was to optimize the design of the Abu Dhabi qubit in order to minimize electromagnetic losses and improve the coherence time. This was achieved by

modifying the shape and size of the pads composing the qubit and exploring other simple geometric shapes of the pads. This led to the selection of a new design, used to fabricate new devices at the CNR-IFN in Rome. In parallel, we studied the main features of Josephson junctions, particularly extracting the critical current of four junctions produced at the CNR-IFN in Rome through direct current measurements. After making the same measurement for two qubits fabricated with the new design developed in this work. All the measurements are carried out at the National Laboratories of INFN in Frascati.

The thesis is structured as follows. In Chapter 2, we introduce the necessary theoretical background for examining superconducting devices. In Chapter 3, we show the principal mechanisms of parameters extraction from ANSYS simulations and the development of qubit designs optimizing the losses. In Chapter 4, we propose the results for the transmon characterization of the Abu Dhabi qubit and for the direct current measurements of the Josephson junction and the qubit fabricated at CNR-IFN. Finally, Chapter 5 concludes the study with a summary of the results and a discussion of future research in the field

Chapter 2

Theory

2.1 Josephson junction

The Josephson junction (JJ) is the principal component of a superconducting qubit. In this section the principal features and behavior of this device are presented. The Josephson junction is composed of two islands of superconductor metals separated by a insulating layers. At the core of the Josephson junction's operation is the physical phenomenon of the Cooper pair tunneling effect between the superconductors.

If the temperature is sufficiently high, above the critical temperature of the superconductors, the junction behaves like a resistance R following Ohm's law. Below the critical temperature T_0 , the normal metal becomes a superconductor made of Cooper pairs, behaving like a condensate of bosons [7]. The superconductor is describable by a macroscopic wavefunction of the form:

$$\psi = \sqrt{\rho}e^{i\phi} \tag{2.1}$$

where ρ is the density of Cooper pairs and ϕ is the phase common to all the Cooper pair in each superconducting island.

To visualize the energy level of a superconductor we use the Bose condensation representation (figure 2.1). At zero temperature, Cooper pairs only occupy a single ground level, since they behave as bosons. Above absolute zero some pairs break up and individual electrons are excited to the conduction band, populating it in a small fraction. The electrons in this band are called quasiparticles, so the conduction band is also called quasiparticles state. The binding energy of a Cooper pair E_g is shared by the two electrons, a single electron has a binding energy $\frac{E_g}{2} = \Delta$, with Δ the energy gap between the Cooper pair level and the conduction band. In a Josephson junction, quasiparticles move between the two superconductors if the applied potential exceed the value $V_{gap} = \frac{2\Delta}{e}$ (Figure 2.1(b)).

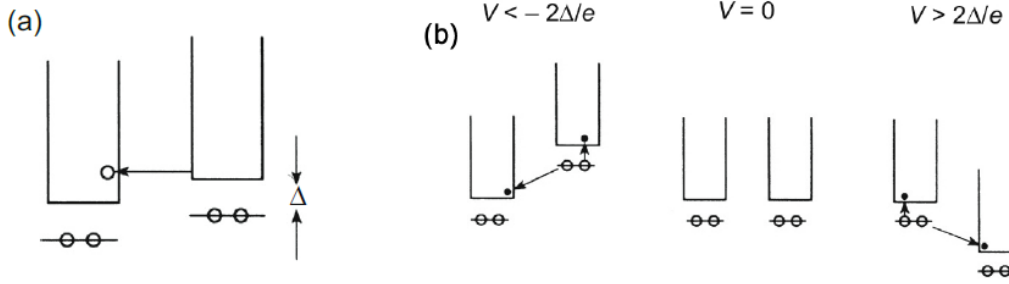


Figure 2.1: a) Tunneling of the two superconductors of a JJ. b) Tunneling between the JJ superconductors in presence of external voltage at zero temperature.

2.1.1 The Josephson equations

The first Josephson equation relates the current I flowing through the junction with the phase difference $\delta = \phi_1 - \phi_2$ between the superconductors 1 and 2:

$$I = I_0 \sin \delta \quad (2.2)$$

This equation states that the superconducting current flows up to a maximum current I_0 , called critical current.

The second Josephson equation relates the voltage V drop across the junction with the time derivative of the superconducting phase difference:

$$V(t) = \frac{\hbar}{2e} \frac{\partial \delta}{\partial t} = \frac{2\pi}{\Phi_0} \frac{\partial \delta}{\partial t} \quad (2.3)$$

with $\Phi_0 = \frac{h}{2e} = 2.07 \cdot 10^{-15}$ Wb is the quantum flux.

Another important relation is the Ambegaokar-Baratoff formula, indeed there is a strong connection between the critical current I_0 and the tunnel resistance R_n , that comes out from the BCS theory [8]:

$$I_0(T) = \frac{\pi \Delta(T)}{2e R_n} \tanh \frac{\Delta(T)}{2k_B T} \quad (2.4)$$

with Δ the energy gap of the two superconductors and T the temperature. The expression is valid if the dimensions of the junctions are small compared to the so-called Josephson length (order of tens of micrometers).

The Josephson junction acts as a non-linear inductance L_J . To obtain the value of L_J we substitute the second Josephson relation (equation 2.3) inside the derivative of the first one (equation 2.2) in the superconductive regime $I < I_0$:

$$\frac{dI}{dt} = I_0 \cos \delta \frac{d\delta}{dt} = I_0 \frac{q}{\hbar} V(t) \cos \delta = \frac{2\pi I_0}{\Phi_0} V(t) \cos \delta \quad (2.5)$$

therefore we can define the non-linear inductance depending on the Josephson current:

$$L(I) = \frac{\Phi_0}{2\pi I_0 \cos \delta} = \frac{L_0}{\cos \delta} = \frac{L_0}{\sqrt{1 - \sin^2 \delta}} = \frac{L_0}{\sqrt{1 - \left(\frac{I}{I_0}\right)^2}} \quad (2.6)$$

with $L(0) = L_0 = \frac{\Phi_0}{2\pi I_0}$ the characteristic parameter of the junction called Josephson inductance.

The energy collected from this inductor is defined as

$$E_J = \int_{-\infty}^t I(t') V dt' = \frac{I_0 \Phi_0}{2\pi} \int_0^{\delta(t')} \sin \delta d\delta = L_0 I_0^2 (1 - \cos \delta) = E_{J0} (1 - \cos \delta) \quad (2.7)$$

in which

$$E_{J0} = L_0 I_0^2 = \frac{\hbar}{2e} I_0 = \frac{\Phi_0 I_0}{2\pi} \quad (2.8)$$

is the Josephson energy.

2.1.2 I-V characteristic

The principal features of a Josephson junction can be described analyzing the I-V characteristics (IVC). The IVC of a Josephson junction is antisymmetric in the origin, therefore for simplicity we consider only the positive part. An example of a real IVC from a DC current measurement is shown in Figure 2.2. We summarize the different behaviors.

1. For the branch A to B, we have a potential $V \gg \frac{2\Delta}{e}$, defining a normal state characterized by the motion of electrons. The current is proportional to the voltage as $I = \frac{V}{R}$, with R being the normal resistance.
2. In the branch B to C, the applied voltage is $V > \frac{2\Delta}{e}$, above the Cooper pairs breaking voltage. This results in a tunneling given by single electrons in the quasiparticle state.
3. The branch C to D the potential is $V < \frac{2\Delta}{e}$. It is characterized by motions of quasiparticles, since some individual electrons already occupy the conduction band due to a non-zero temperature.
4. In the branch D to E, the voltage is $V < \frac{2\Delta}{e}$ or null, and we have only supercurrent with the motion of Cooper pairs between the superconductors, defined by the two Josephson effects in Equations 2.2 and 2.3. This is called also zero-voltage stage.
5. Increasing the bias current, we have a jump from point E with $V < \frac{2\Delta}{e}$ or null, to point F with $V > \frac{2\Delta}{e}$, since the current exceeds the critical current of the junction.

6. The branch F to A is equivalent to A to B in the normal state.

The IVC presents two important effects: the presence of a *retrapping current* I_r , since the current in the branch C to D never goes exactly to zero, and the presence of *self-heating* due to the electrical components. This is evidenced by a small curve towards higher potential in the B to C branch of the IVC. This effect is taken into account by measuring the value of the critical potential V_c , which corresponds to the critical current of the JJ.

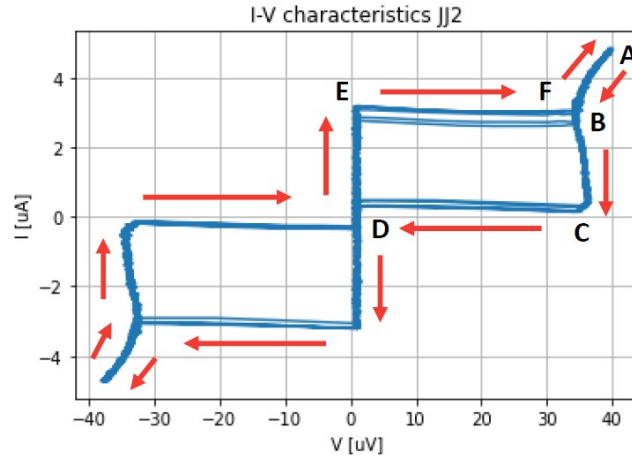


Figure 2.2: I-V characteristics for a real Josephson junction. The red arrows indicate the succession of the IVC during a current swap.

2.1.3 Resistively and capacitively shunted Josephson junction (RCSJ)

A real Josephson junction can be modeled with a circuit as described in the resistively and capacitively shunted Josephson junction (RCSJ) model [9]. The RCSJ model allow us to study the response of a Josephson junction to external driving sources quantitatively and to give a better description of the IVC of a JJ. In this case, we want to study a JJ crossed by an external DC current I with potential V across the JJ. The circuit that represents this model is shown in Figure 2.3. It is composed by the ideal junction J in parallel with a resistance R , a capacitance C and a current noise source I_F . Each component represents a different contribution of the driving current:

- The resistance represents a *dissipation current* I_R , due to conduction currents and quasiparticle tunneling currents. The resistance is voltage and temperature dependent, for the RSCJ model we consider it constant.
- The capacity represents the *displacement current* I_C due to the finite capacitance C between the junction between the two superconductors. The DC

current that causes a variation of the potential V across the JJ influence the charge distribution at the interface layers ($\frac{\partial V}{\partial t} \neq 0$).

- The current noise source represents the *fluctuation current* I_F , due to the thermal motion.

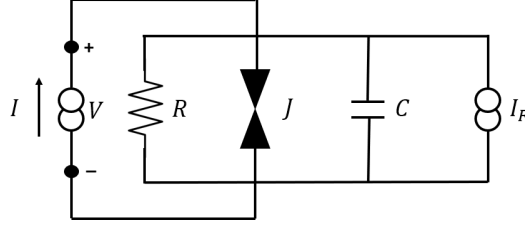


Figure 2.3: The resistively and capacitively shunted Josephson junction circuit driven by a current.

The total current given by the Kirchhoff law is composed by the three terms of the electronic components of the circuit:

$$I = I_R + I_C + I_J = \frac{V}{R} + C \frac{\partial V}{\partial t} + I_J \quad (2.9)$$

in which ϕ the phase of the superconductor. Substituting the two Josephson relations (Equations 2.2 and 2.3) the formula becomes

$$I = \frac{\hbar}{2e} C \frac{\partial^2 \phi}{\partial t^2} + \frac{\hbar}{2e} \frac{1}{R} \frac{\partial \phi}{\partial t} + I_0 \sin(\phi) \quad (2.10)$$

with I_0 the critical current of the junction. To describe the circuit, we manipulate the formula introducing the plasma frequency ω_p and the quality factor Q of the junction:

$$\frac{I}{I_0} = \frac{\partial^2 \phi}{\partial \tau^2} + \frac{1}{Q} \frac{\partial \phi}{\partial \tau} + \sin(\phi) \quad (2.11)$$

with $\tau = \omega_p t$ a dimensionless parameter. The plasma frequency for $I = 0$ is

$$\omega_p = \sqrt{\frac{2eI_0}{\hbar C}} \quad (2.12)$$

The quality factor is $Q = \omega_p RC$, it gives a quantitative indication of the dissipation. In general, two different solutions of equation 2.11 always exist for every value of Q : For $I < I_0$, when $\frac{d\phi}{dt} = 0$, the solution is $I = I_0 \sin(\phi)$, corresponding to having only supercurrent. For $I \gg I_0$, the solution is $I = \frac{V}{R}$, indicating only normal current.

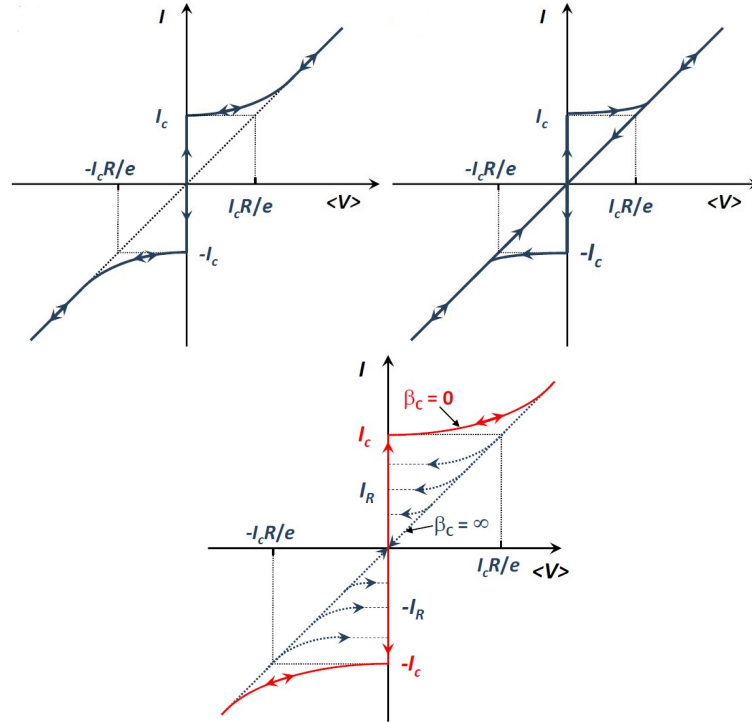


Figure 2.4: I-V characteristic for an ideal junction in overdamped (*up-left*), underdamped (*up-right*) and intermediate (*down*) regime. β_c is the Stewart-McCumber parameter, equal to Q^2 . Figures from [9].

The intermediate solutions depend on the value of Q , with the upper and lower limits corresponding to the overdamped and underdamped regimes, as shown in Figure 2.4. These regimes are determined by the capacitance (C) and resistance (R) components, which define the characteristics of the JJ.

- **Overdamped regime:** This regime is reached for $Q \ll 1$, corresponding to small capacitance and/or resistance values. The IVC of this regime is shown in Figure 2.4 (upper-left). It exhibits a single branch with no hysteretic behaviors: for both decreasing or increasing the current from zero, the curve smoothly transitions between the zero-voltage state and the finite voltage.
- **Underdamped regime:** It is reached for $Q \gg 1$, corresponding to large capacitance and/or resistance. The IVC is presented in Figure 2.4(up-right). Increasing the current, the junction remains in the zero-voltage stage until it jumps to the finite voltage. But decreasing the current, the curve follows the diagonal line into the origin.
- **Intermediate regime:** For $Q \geq 1$, we have an intermediate case. As shown in Figure 2.4(down), the IVC presents a hysteretic curve similar to

the underdamped regime, but in this case, decreasing the current, the curve goes to $V = 0$ smoothly, reaching a retrapping current I_r .

For a complete description of the IVC of a JJ, we must consider the dependence of the resistance on voltage and temperature. In general, the formula of the resistance for quasiparticles is given by [10]:

$$R_{qp} = R \cdot e^{\frac{\Delta}{k_B T}} \quad (2.13)$$

with Δ being the energy gap and T the temperature. This equation shows that R_{qp} becomes extremely high at low temperatures, since the quasiparticle density exponentially decreases with temperature.

We assume the RCSJ-model working with two different resistances, R for $V > \frac{2\Delta}{e}$ and R_{sg} for $V < \frac{2\Delta}{e}$, as we see in Figure 2.5. In which R is the normal resistance and R_{sg} the subgap-resistance, i.e. the resistance in the superconductive regime. This is given by the slope of the voltage dependence for currents just after the critical current.

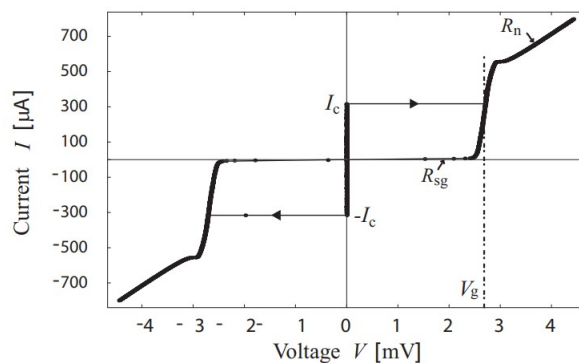


Figure 2.5: I-V characteristic of a JJ considering R_{sg} . Figure from [10].

2.1.4 Titled-washboard model

To better understand the Josephson junction behavior and mechanisms, we compare the RCSJ model to a mechanical analogue model: the tilted-washboard model. The differential equation that describe the RCSJ circuit has the same features of a forced pendulum in classical mechanics with mass M , damping η and potential energy U . The forced pendulum is described by equation

$$M \frac{d^2 x}{dt^2} + \eta \frac{dx}{dt} + \nabla U = 0 \quad (2.14)$$

while the RCSJ equation 2.11 can be rewrite showing the potential term:

$$\frac{\hbar}{2e} C \frac{\partial^2 \phi}{\partial t^2} + \frac{\hbar}{2e} \frac{1}{R} \frac{\partial \phi}{\partial t} + I_0 \left(\sin(\phi) - \frac{I}{I_0} \right) = 0 \quad (2.15)$$

therefore

$$\frac{\hbar}{2e} C \frac{\partial^2 \phi}{\partial t^2} + \frac{\hbar}{2e} \frac{1}{R} \frac{\partial \phi}{\partial t} + \frac{\partial}{\partial \phi} \left[E_J \left(1 - \cos(\phi) - \frac{I}{I_0} \right) \right] = 0 \quad (2.16)$$

with E_J the Josephson energy (from Eq. 2.7). Comparing the equation 2.16 with the 2.14, on the first two terms are the acceleration of the phase (instead of the position in the classical oscillator) and the dissipation term due to the capacitance with $M = \frac{\hbar}{2e} \cdot C$ and $\eta = \frac{\hbar}{2e} \cdot \frac{1}{R}$. The last term is the force potential U (without constant terms):

$$U(\phi, I) = -E_J \left(\cos(\phi) + \frac{I}{I_0} \right) \quad (2.17)$$

This potential is called the washboard potential. A plot of the potential as a function of the phase ϕ for different driving currents is shown in Figure 2.6. The driving current gives different inclinations of the potential corresponding to different mechanisms of the junction. In this analogue, the overdamped regime corresponds to small mass ($M \propto C$) and large damping ($\eta \propto \frac{1}{R}$), while the underdamped regime has large mass and small damping.

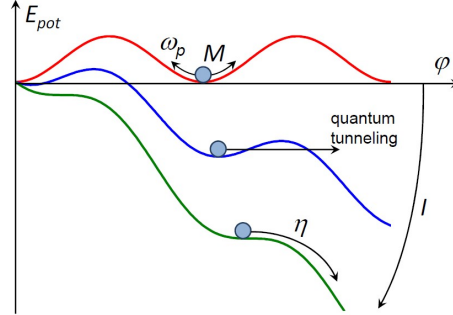


Figure 2.6: Washboard potential for different driving currents. Image from [9]

In the following, we make a discussion about the motion of the phase (treated as a massive particle) on the potential when the driving current I into the junction increases and decreases [9].

Decreasing the current: The first case is applying a current larger than the critical current $I > I_0$ and moving it down to zero. The strong tilt of the potential moves the particle freely down the potential, but reducing the current reduces the tilt of the potential until at $I < I_0$ local minima are obtained.

In a regime near overdamping, the particle will immediately stop its motion and will be trapped in one of the local minima. The junction voltage goes to zero immediately when the applied current is reduced below I_0 . But for a regime near

underdamping, the massive particle has sufficient kinetic energy and can easily move down the potential well even if there are local minima. To stop the particle, the potential is almost horizontal, meaning that we have to reduce the current almost to zero to have zero voltage.

Increasing the current: The second situation consists of starting with $I = 0$ and increasing the current over I_0 . In both overdamped and underdamped cases, the voltage remains zero until the critical current is reached. The reason is that the kinetic energy of the particle is zero, therefore it doesn't move down the potential. For values above the critical current, the behavior is different again: near overdamping, the particle is moving slowly, and in the underdamped case, the particle immediately accelerates to an average velocity.

2.2 Qubit

A qubit, short for quantum bit, is the basic unit of quantum information in quantum computing, analogous to a classical bit in classical computing. The qubit is a two-level system that can exist in a superposition of states 0 and 1 simultaneously, unlike classical bits that can only be in one of them.

The superconducting qubit is a type of qubit engineered from superconducting materials, cooled to extremely low temperatures. There are several types of superconducting qubits, in this work we analyze the transmon qubit. It is known for its relatively long coherence times which are crucial to perform quantum operations accurately.

The transmon qubit is composed by a Josephson junction set between two conductive pads. It is possible to analyze a superconductive qubit from a circuit point of view, this technique is called circuit QED (cQED). The qubit is modeled as a LC circuit, with a non-linear inductance given by the Josephson junction and a capacity given by the two conductors.¹

An LC circuit can be treated as a harmonic oscillator in quantum mechanics, defined by distinct energy levels that are uniformly spaced from each other. To create a two-level system it is necessary to introduce anharmonicity in the energy levels to distinguish the ground state from the first excited one. In this section we explain how this is achieved specifically for a transmon qubit [11].

2.2.1 Quantization of a LC circuit

Initially, we quantize a classical LC circuit (Figure 2.7) as an harmonic oscillator with a Lagrangian description [12]. The energy stored in the capacitance C and

¹It is important to notice that also the Josephson junction has a finite capacity but comparing it with the capacity of the pads, it is negligible for a transmon qubit.

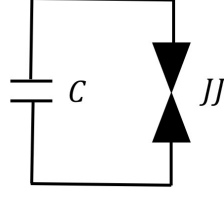


Figure 2.7: The qubit circuit that consist of a capacity in parallel with an inductance. We start quantizing a LC circuit (at start JJ is a lineal inductance L) and after we substitute it with the Josephson junction JJ, to create anharmonicity.

inductance L depends on the flux variable defined as:

$$\Phi(t) = \int_{-\infty}^t dt' V(t') = LI \quad (2.18)$$

in which $I = \frac{dQ}{dt}$ is the current and Q the charge. The energy is given by ($\delta E = V\delta Q$):

$$E(t) = \int_{-\infty}^t dt' V(t') I(t') \quad (2.19)$$

that for the single components is:

$$\text{Capacity: } E_C = \int_{-\infty}^t dt' V \frac{dV}{dt'} = \frac{C}{2} V^2 = \frac{Q^2}{2C}, \quad (2.20)$$

$$\text{Inductance: } E_L = \int_{-\infty}^t dt' L \frac{dI}{dt'} I = \frac{L}{2} I^2 \equiv \frac{\Phi^2}{2L}. \quad (2.21)$$

In a classic discussion we interpret the term relating to capacity as a kinetic energy while that relating to inductance as potential energy. In this context we write the classical Lagrangian of the system:

$$\mathcal{L} = E_C - E_L = \frac{Q^2}{2C} - \frac{\Phi^2}{2L} = \frac{C}{2} V^2 - \frac{\Phi^2}{2L} = \frac{1}{2} C \dot{\phi}^2 - \frac{\phi^2}{2L} \quad (2.22)$$

Applying the Eulero-Lagrange equations:

$$\frac{d}{dt} \left(\frac{\partial \mathcal{L}}{\partial \dot{\Phi}} \right) - \frac{\partial \mathcal{L}}{\partial \Phi} = 0,$$

we obtain the equation of motion:

$$C\ddot{\Phi} + \frac{\Phi}{L} = 0,$$

which is the equation of motion of a harmonic oscillator:

$$\ddot{\Phi} + \omega^2 \Phi = 0, \quad \text{where } \omega = \frac{1}{\sqrt{LC}}.$$

with ω the pulse frequency of the oscillator. To move to a quantum description of the system, we pass to the Hamiltonian formalism. Let's calculate the conjugate momentum:

$$\Pi = \frac{\delta L}{\delta \dot{\Phi}} = C\dot{\Phi} = CV = Q,$$

thus we calculate the Legendre transform:

$$H = \Pi\dot{\Phi} - L = \frac{Q^2}{C} - \left(\frac{Q^2}{2C} - \frac{\Phi^2}{2L} \right) = \frac{Q^2}{2C} + \frac{\Phi^2}{2L}; \quad (2.23)$$

now impose canonical quantization. We promote $(\Phi, Q) \rightarrow (\hat{\Phi}, \hat{Q})$ to operators and express them in terms of the creation and annihilation operators:

$$\hat{\Phi} = \sqrt{\frac{\hbar}{2C\omega}} (\hat{a} + \hat{a}^\dagger),$$

$$\hat{Q} = \frac{\sqrt{2C\omega\hbar}}{2i} (\hat{a} - \hat{a}^\dagger).$$

imposing the following commutation rules:

$$[\hat{\Phi}, \hat{Q}] = i\hbar, \quad \Rightarrow \quad [\hat{a}, \hat{a}^\dagger] = 1.$$

The Hamiltonian of the LC harmonic oscillator is

$$H = \hbar\omega \left(\hat{n} + \frac{1}{2} \right) \quad (2.24)$$

where \hat{n} is the number operator $\hat{n} = \hat{a}^\dagger \hat{a}$ and the eigenstates $|n\rangle$ follow the relations:

$$a|n\rangle = \sqrt{n}|n-1\rangle \quad a^\dagger|n\rangle = \sqrt{n+1}|n+1\rangle, \quad (2.25)$$

2.2.2 The transmon qubit

The next step is define the Hamiltonian for a qubit. The qubit has a Josephson junction with energy given by the equation 2.7. We write the Lagrangian for a qubit as:

$$\mathcal{L} = E_C - E_J = \frac{1}{2}C\dot{\phi}^2 + E_{J0}(1 - \cos \hat{\delta}) \quad (2.26)$$

with δ the phase difference between the superconductors of the JJ. The conjugate variable is:

$$Q = \frac{\partial \mathcal{L}}{\partial \dot{\phi}} = C\dot{\phi}$$

The Hamiltonian $H = Q\dot{\phi} - \mathcal{L}$ is:

$$H = \frac{Q^2}{2C} - E_{J0}(1 - \cos \delta) \quad (2.27)$$

Now, we write the Hamiltonian considering that the qubit is in a superconductive system:

$$H = 4E_C n^2 + E_{J0}(1 - \cos \delta) \quad (2.28)$$

in which

$n = \frac{\hat{Q}}{2e}$ is the number of Cooper pairs passing through the junction;

$\delta = \frac{2\pi}{\Phi_0} \Phi$ is the phase difference of the superconductors;

$E_C = \frac{e^2}{2C}$ is the energy required to add an extra electron to the circuit's capacitance;

A transmon qubit works in the limit where $E_{J0}/E_C \gg 1$. In this limit, the system is less sensitive to charging noise. Furthermore, the eigenstates of the phase operator are first-order eigenstates of energy. Expanding for small delta:

$$V(\delta) = E_{J0}(1 - \cos \delta) = \frac{E_{J0}}{2!} \delta^2 - \frac{E_{J0}}{4!} \delta^4 + \frac{E_{J0}}{6!} \delta^6 + O(\delta^8);$$

note that the first term generates the harmonic potential. Truncating the expansion at the second term, the resulting transmon qubit Hamiltonian is:

$$H = 4E_C n^2 + \frac{E_{J0} \delta^2}{2} - \frac{E_{J0} \delta^4}{24} \quad (2.29)$$

We promote the operators $(n, \delta) \rightarrow (\hat{n}, \hat{\delta})$ and, as in last section, we write the terms with the creation and annihilation operators:

$$\hat{\delta} = \sqrt{\frac{\zeta}{2}}(a + a^\dagger), \quad \hat{n} = -\frac{i}{\sqrt{2\zeta}}(a - a^\dagger), \quad \zeta = \sqrt{\frac{8E_C}{E_{J0}}} \quad (2.30)$$

With these definitions, the first two terms of equation 2.29 correspond to $\hat{H}_0 = \hbar\omega_0 (\hat{a}^\dagger \hat{a} + \frac{1}{2})$ of a quantum harmonic oscillator, that oscillate at frequency ω_0 . The third term of the Hamiltonian is the anharmonic correction.

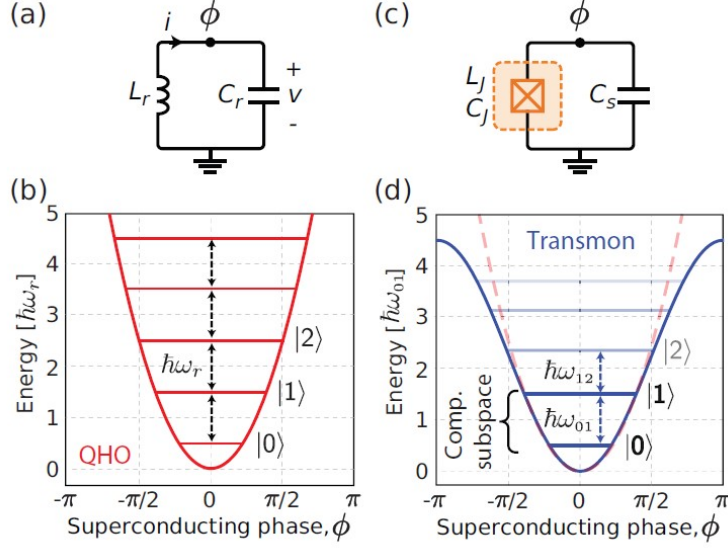


Figure 2.8: (a) Circuit for LC-oscillator, with inductance L in parallel with capacitance C . The superconducting phase on the island is denoted ϕ , referencing ground as zero. (b) Energy potential for the QHO, where energy levels are equidistantly spaced $\sim \omega_r$ apart. (c) Josephson qubit circuit, where the nonlinear inductance L_J (represented with the Josephson-subcircuit in the dashed orange box) in parallel with a capacitance C_s . (d) The Josephson inductance reshapes the quadratic energy potential (dashed red) into sinusoidal (solid blue), which yields non-equidistant energy levels. This allows us to isolate the two lowest energy levels $|0\rangle$ and $|1\rangle$. Figure from [11].

For a transmon, the eigenvalues are no longer equidistant: in Figure 2.8, we notice that the states $|0\rangle$ and $|1\rangle$ are separated by an energy $\hbar\omega_{01}$, while the states $|1\rangle$ and $|2\rangle$ by an energy $\hbar\omega_{12} = \hbar\omega_{01} + \alpha$ with $\alpha < 0$. If $\hbar\omega_{01}$ is reasonably large, we can consider only the states $|0\rangle$ and $|1\rangle$.

We explicitly express the operator definitions from Equation 2.30 in the Hamiltonian 2.29, resulting in:

$$\hat{H} = \hbar\omega_0 \left(\hat{a}^\dagger \hat{a} + \frac{1}{2} \right) - \frac{E_C}{12} (\hat{a} + \hat{a}^\dagger)^4 \quad (2.31)$$

To simplify the situation, we consider the free Hamiltonian moved to a rotating system. Here we keep only the interaction terms that evolve slowly over time (rotating wave approximation RWA). The operator that performs the rotation is then:

$$\hat{U} = e^{i\hat{H}_0 t},$$

which, applied to the creation and annihilation operators, generates a time-dependent

phase:

$$\hat{a} \rightarrow e^{-i\omega_0 t} \hat{a}, \quad \hat{a}^\dagger \rightarrow e^{i\omega_0 t} \hat{a}^\dagger.$$

This means that all terms that have a different number of \hat{a} and \hat{a}^\dagger in $\hat{a} + \hat{a}^\dagger$ are on average zero, only the terms with an equal number survive. Considering the commutation relation $[a, a^\dagger] = 1$ we obtain:

$$(\hat{a} + \hat{a}^\dagger)^4 = 6\hat{a}^\dagger \hat{a}^\dagger \hat{a} \hat{a} + 6\hat{a}^\dagger \hat{a} + 3 \quad (2.32)$$

Finally, substituting this result in 2.31 the Hamiltonian for a transmon qubit is:

$$H = \hbar\omega_T a^\dagger a + \frac{\alpha}{2} a^\dagger a^\dagger a a, \quad (2.33)$$

where ω_T is the transmon frequency:

$$\hbar\omega_T = \hbar\omega_0 - E_c = \sqrt{8E_{J0}E_c} - E_c. \quad (2.34)$$

The anharmonicity α ($\alpha < 0$) and the relative anharmonicity α_r are defined as:

$$\alpha = E_{12} - E_{01} = -E_c \quad \alpha_r = \alpha/E_{01} \simeq -\sqrt{\frac{E_c}{8E_{J0}}} \quad (2.35)$$

with $E_{ij} = \hbar\omega_{ij}$ the energy difference between the consecutive states i and j , depending on the difference of the relative pulse frequencies $\omega_{ij} = \omega_j - \omega_i$.

This results are valid for a transmon considering only the first anharmonic term, the more general solution for $|n\rangle$ states is given by time independent perturbation theory. We obtain the same results perturbing the Hamiltonian 2.31 at the first order:

$$\begin{aligned} E_n &= E_n^0 - \frac{E_c}{12} \langle n | (a + a^\dagger)^4 | n \rangle \\ |n\rangle_1 &= |n\rangle - \frac{E_c}{12} \sum_{k \neq n} \frac{\langle k | (a + a^\dagger)^4 | n \rangle}{\hbar\omega_0(n - k)} \end{aligned} \quad (2.36)$$

with E_n is the energy of state n and $|n\rangle_1$ the state at the first order of the perturbation theory. Using the relations 2.25, the energy of the state n is given by:

$$E_n = \hbar\omega_0 \left(n + \frac{1}{2} \right) - \frac{E_c}{12} \langle n | (a + a^\dagger)^4 | n \rangle \quad (2.37)$$

from this equation we find the same solutions of the RWA approach. In general the energy difference $E_{n,n+1}$ between consecutive levels $|n\rangle$ and $|n+1\rangle$ is:

$$E_{n,n+1} = \hbar\omega_{n,n+1} = E_{n+1} - E_n = \hbar\omega_0 - (n+1)E_c \quad (2.38)$$

The first energy levels of the Hamiltonian are the following:

$$\begin{aligned}\hat{H} |0\rangle &= 0, \\ \hat{H} |1\rangle &= \hbar\omega_T |1\rangle, \\ \hat{H} |2\rangle &= (2\hbar\omega_T + \alpha) |2\rangle;\end{aligned}$$

In some context, for simplicity, we can consider a transmon circuit as a two-level system which can be described as a pseudo-spin with the Pauli operator $\sigma_z = \begin{pmatrix} 1 & 0 \\ 0 & -1 \end{pmatrix}$:

$$\hat{H}_q = -\frac{\hbar\omega_q}{2}\sigma_z \quad (2.39)$$

where $\omega_T = \omega_q = \omega_{01}$ is the lowest transition frequency in the transmon circuit.

The eigenstates are $\{|0\rangle = \begin{pmatrix} 1 \\ 0 \end{pmatrix}, |1\rangle = \begin{pmatrix} 0 \\ 1 \end{pmatrix}\}$ with eigenvalues $\{E_{|0\rangle,|1\rangle} = \mp \frac{\hbar\omega_q}{2}\}$.

2.2.3 Block sphere

First we introduce a geometric representation of the space of a two level quantum system useful to visualize the transmon dynamics: the Bloch sphere (Figure 2.9). A qubit state $|\psi\rangle$ can be written as the complex superposition of two the states $|0\rangle$ and $|1\rangle$, which form an orthonormal basis for the Hilbert space:

$$|\psi\rangle = \cos\left(\frac{\theta}{2}\right)|0\rangle + i \sin\left(\frac{\theta}{2}\right)e^{i\phi}|1\rangle, \quad (2.40)$$

We introduce the following unit vector in 3 dimensions $\vec{a} = (\sin\theta \cos\phi, \sin\theta \sin\phi, \cos\theta)$, and we draw the sphere in R^3 ; in this way, the generic state is identified by a single point univocal on the sphere and it is determined by the angles θ and ϕ . The three Pauli matrices parameterize the spin and the three axes of the Bloch sphere can be associated with the spin. The spin vector is given by $\vec{\sigma} = (\sigma_x, \sigma_y, \sigma_z)$. Considering the generic state, we define the spin along a generic direction $\vec{\sigma} \cdot \vec{a}$:

$$\vec{\sigma} \cdot \vec{a} = \cos\phi \sin\theta \sigma_x + \sin\phi \sin\theta \sigma_y + \cos\theta \sigma_z;$$

$|\psi\rangle$ is an eigenstate of $\vec{\sigma} \cdot \vec{a}$ with eigenvalue 1, that is, $\vec{\sigma} \cdot \vec{a} |\psi\rangle = |\psi\rangle$. A representation of the Bloch sphere is shown in Figure 2.9.

There exists a class of unitary operator that implements a rotation of angle λ around the direction identified by \vec{a} . They are given by

$$R_{\vec{a}}(\lambda) = e^{-i\frac{\lambda}{2}(\vec{a} \cdot \vec{\sigma})} = \cos\left(\frac{\lambda}{2}\right) I - i \sin\left(\frac{\lambda}{2}\right) \vec{\sigma} \cdot \vec{a} \quad (2.41)$$

with I the 2×2 identity matrix.

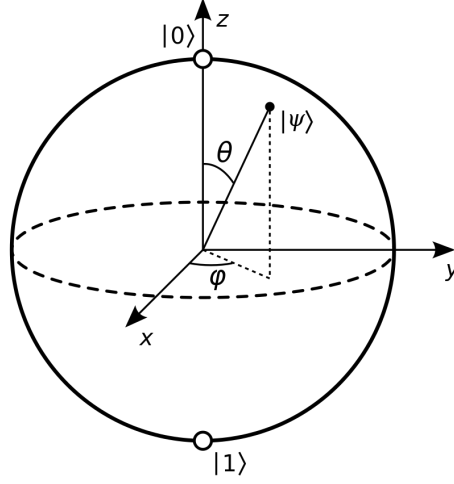


Figure 2.9: The Bloch sphere that represent a qubit in a 3D space. The $|\psi\rangle$ is a generic state of the qubit.

This representation is useful to visualize the dynamics of a qubit. In particular, we introduce the density matrix to give a description of the qubit interacting with the environment. The density matrix is defined as

$$\rho = \sum_i p_i |\psi_i\rangle \langle \psi_i| \quad (2.42)$$

with p_i the probability of being in state $|\psi_i\rangle$. If the matrix has only one state it is called a pure state $|\psi\rangle = \alpha |0\rangle + \beta |1\rangle$ and the density matrix is

$$\rho = |\psi\rangle \langle \psi| = \begin{pmatrix} |\alpha|^2 & \alpha\beta^* \\ \alpha^*\beta & |\beta|^2 \end{pmatrix} \quad (2.43)$$

2.3 Resonant cavity

A resonant cavity is a closed conductor containing electromagnetic waves reflecting back and forth between the cavity walls. The electromagnetic field inside the cavity can be excited and can take on different configurations, called resonant modes. These modes are determined by the cavity's geometry and boundary conditions.

Transmission lines consisting of two or more conductors can support transverse electromagnetic (TEM) waves. While waveguides consisting of a single conductor, support transverse electric (TE) and/or transverse magnetic (TM) waves, characterized by the presence of longitudinal magnetic or electric field components. A rectangular cavity is constructed from closed sections of waveguide, short circuited at both ends in order to form a closed box. Each mode has its own resonance frequency, the cavity support multiple modes simultaneously.

2.3.1 Cavity 1D

We first introduce cavities in one dimension. The electromagnetic modes of a cavity are described by Maxwell's equations. For a one-dimensional cavity, we consider a pair of infinite perfect conducting walls separated by the distance L along the z -direction, so that fields only depend on the z -coordinate. For an empty cavity with no external source the Maxwell equations are[13]:

$$\nabla \times \vec{E} = -\frac{\partial \vec{B}}{\partial t} \rightarrow \frac{\partial E_x(z, t)}{\partial z} = -\frac{\partial B_y(z, t)}{\partial t} \quad (2.44)$$

$$\nabla \times \vec{B} = \epsilon_0 \mu_0 \frac{\partial \vec{E}}{\partial t} \rightarrow -\frac{\partial B_y(z, t)}{\partial z} = \epsilon_0 \mu_0 \frac{\partial E_x(z, t)}{\partial t} \quad (2.45)$$

$$\nabla \cdot \vec{E} = 0 \rightarrow \frac{\partial E_x(z, t)}{\partial x} = 0 \quad (2.46)$$

$$\nabla \cdot \vec{B} = 0 \rightarrow \frac{\partial B_y(z, t)}{\partial y} = 0 \quad (2.47)$$

with $\vec{E} = (E_x, E_y, E_z)$ and $\vec{B} = (B_x, B_y, B_z)$ the electric and magnetic fields and μ_0 and ϵ_0 the vacuum permeability and permittivity. Applying the boundary conditions $E_x(z = 0, t) = 0$ and $E_x(z = L, t) = 0$, the solution of electric and magnetic fields inside the cavity are:

$$E_x(z, t) = E_{cl} q(t) \sin(kz) \quad (2.48)$$

$$B_y(z, t) = E_{cl} \frac{\mu_0 \epsilon_0}{k} \dot{q}(t) \cos(kz). \quad (2.49)$$

with E_{cl} the normalization constant, given by: $E_{cl} = \sqrt{\frac{2\omega_c^2}{\epsilon_0 V}}$. The parameter V is the effective volume of the cavity and $k = \frac{m\pi}{L}$ is the wave number corresponding to the frequency $\omega_c = \frac{k}{\sqrt{\mu_0 \epsilon_0}}$. The number m is an integer and define a specific mode of the cavity. A representation of the electric and magnetic field is shown in Figure 2.10.

The aim is quantize the electromagnetic field, promoting the promoting canonical position q and canonical momentum p to operators. The total electromagnetic energy (per unit of volume) stored in one mode can be written as:

$$H = \frac{1}{V} \int_V \left(\frac{\epsilon_0}{2} |E_x(z, t)|^2 + \frac{1}{2\mu_0} |B_y(z, t)|^2 \right) dV \quad (2.50)$$

by substituting Equations 2.48 and 2.49 into 2.50, the total energy is equal to:

$$H = \frac{1}{2} (p^2(t) + \omega_c^2 q^2(t))$$

where $p(t) = \dot{q}(t)$, the energy of a mode is analogous to the energy of a classical harmonic oscillator. The quantize Hamiltonian is defined by promoting the

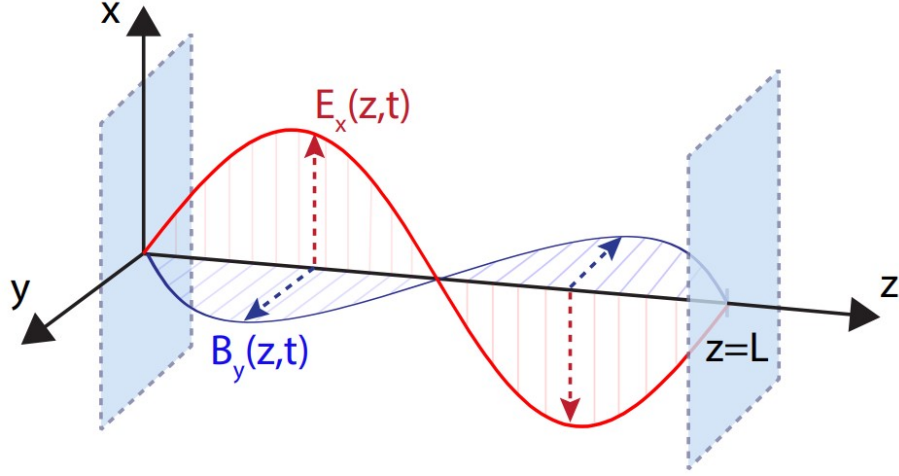


Figure 2.10: Schematic representation of a 1D cavity composed by two infinite walls and the relative electric (red line) and magnetic (blue line) fields. Figure from [13]

canonical parameters to be operators ($p, q \rightarrow \hat{p}, \hat{q}$). The transition to a quantum mechanical description results in quantization of the energy spectrum for each mode. We can define operators \hat{b} and \hat{b}^\dagger , the annihilation and creation operators for a photon in the corresponding mode of the cavity ($\hbar = 1$):

$$\hat{b}^\dagger = \frac{1}{\sqrt{2\omega_c}}(\omega_c \hat{q} + i\hat{p}) \quad (2.51)$$

$$\hat{b} = \frac{1}{\sqrt{2\omega_c}}(\omega_c \hat{q} - i\hat{p}) \quad (2.52)$$

with the commutation relation $[\hat{b}, \hat{b}^\dagger] = 1$. The solution for electric and magnetic field results:

$$\hat{E}_x(z, t) = E_0(\hat{b} + \hat{b}^\dagger) \sin(kz) \quad (2.53)$$

$$\hat{B}_y(z, t) = E_0 \frac{\mu_0 \epsilon_0}{k} (\hat{b} - \hat{b}^\dagger) \cos(kz) \quad (2.54)$$

with $E_0 = \sqrt{\frac{\hbar \omega_c}{2\epsilon_0 V}}$ the normalization constant. The Hamiltonian is the harmonic oscillator:

$$\hat{H} = \hbar \omega_c (\hat{b}^\dagger \hat{b} + \frac{1}{2}) = \hbar \omega_c (\hat{n} + \frac{1}{2}), \quad (2.55)$$

$$\hat{H}|n\rangle = E_n|n\rangle, \quad (2.56)$$

with n the number operator, that define the number of photon inside the cavity. The energy eigenstate for a single-mode cavity are $\{|n\rangle\}$ and the corresponding eigenvalues are $\{E_n = \hbar \omega_c (n + \frac{1}{2})\}$.

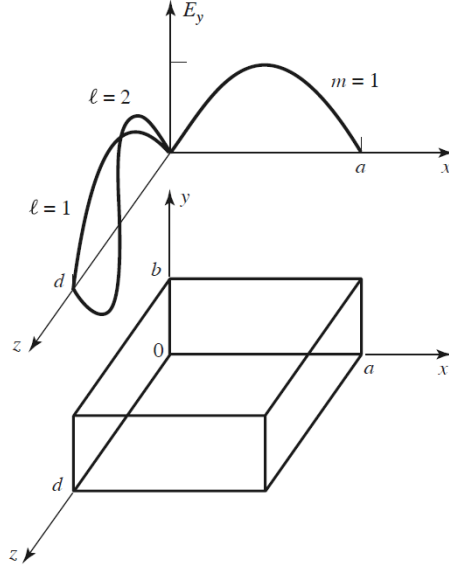


Figure 2.11: rectangular cavity resonator, and the electric field variations for the TE₁₀₁ and TE₁₀₂ resonant modes.

2.3.2 Rectangular 3D cavity

We consider a cavity formed by a length d of rectangular waveguide shorted at both ends ($z = 0, z = d$), with dimensions a , b , and d in the x , y , and z directions of the reference frame, as depicted in Figure 2.11. The cavity modes begin with the TE or TM waveguide modes, as they already satisfy the necessary boundary conditions on the side walls ($x = 0, a$ and $y = 0, b$) of the cavity.

The transverse electric fields (E_x, E_y) of the $TE_{m,n}$ or $TM_{m,n}$ rectangular waveguide modes can be expressed as [14]:

$$\tilde{E}(x, y, z) = \tilde{E}(x, y) (A^+ e^{-j\beta_{mn}z} + A^- e^{j\beta_{mn}z}),$$

where $\tilde{E}(x, y)$ is the transverse variation of the mode, and A^+ and A^- are the amplitudes of the forward and backward traveling waves. The propagation constant of the m, n th TE or TM mode is given by:

$$\beta_{mn} = \sqrt{k^2 - \left(\frac{m\pi}{a}\right)^2 - \left(\frac{n\pi}{b}\right)^2},$$

where $k = \omega\sqrt{\mu_0\epsilon_0}$, and μ_0 and ϵ_0 are the vacuum permeability and permittivity.

Applying the condition for reflection from a conducting wall, $\tilde{E} = 0$ at $z = 0$ implies $A^+ = -A^-$. Then, the condition $\tilde{E} = 0$ at $z = d$ leads to the equation:

$$\tilde{E}(x, y, d) = -\tilde{E}(x, y)A^+2j \sin(\beta_{mn}d) = 0.$$

The only nontrivial ($A^+ \neq 0$) solution occurs when:

$$\beta_{mn}d = \pi \text{ for } \pi = 1, 2, 3, \dots,$$

implying that the cavity must be an integer multiple of a half-guide wavelength long at the resonant frequency. No nontrivial solutions are possible for other lengths or frequencies apart from the resonant frequencies.

The resonance wave number for the rectangular cavity can be defined as:

$$k_{mnl} = \sqrt{\left(\frac{m\pi}{a}\right)^2 + \left(\frac{n\pi}{b}\right)^2 + \left(\frac{l\pi}{d}\right)^2}.$$

We then refer to the TE_{mnl} or TM_{mnl} resonant mode of the cavity. Each mode is described by a set of integers, that are described in $\vec{n} = (n, m, l)$. It indicates the number of variations in the standing wave pattern in the the vector direction $\vec{r} = (x, y, z)$. The resonant frequency of the TE_{mnl} or TM_{mnl} mode is given by²:

$$\nu_{mnl} = \frac{\omega_{mnl}}{2\pi} = \frac{ck_{mnl}}{2\pi\sqrt{\mu_0\epsilon_0}} = \frac{c}{2\pi\sqrt{\mu_0\epsilon_0}} \sqrt{\left(\frac{m\pi}{a}\right)^2 + \left(\frac{n\pi}{b}\right)^2 + \left(\frac{l\pi}{d}\right)^2}.$$

If $b < a < d$, the dominant resonant mode, corresponding to the lowest resonant frequency, is the TE_{101} mode. In this mode, the electric field profile has one anti-node in x and z directions, and the electric field oscillations are maximum at the center of the cavity. In figure 2.12, the first two cavity modes for a 3D cavity are shown.

As in the 1D case, the electric field of a cavity is quantized as

$$\hat{E}(x, y, z) = E_0(\hat{b} + \hat{b}^\dagger) \quad (2.57)$$

with the term E_0 that defines the amplitudes of the fields:

$$E_0 = \sqrt{\frac{\hbar\omega_r}{2\epsilon_0 V_{\text{mode}}}} \quad (2.58)$$

The mode volume V_{mode} of a 3D cavity refers to the spatial region where an electromagnetic mode is confined, in which most of the energy associated is concentrated. It depends on the electric field $E(\vec{r})$ inside the cavity:

$$V_{\text{mode}} = \frac{\int_V \epsilon_0(\vec{r})|E(\vec{r})|^2 d\vec{r}}{\max(|E(\vec{r})|^2)} \quad (2.59)$$

²The cavity is in vacuum, a material inside the cavity changes the frequencies of a factor depending on the relative magnetic permeability and the relative permittivity of the medium.

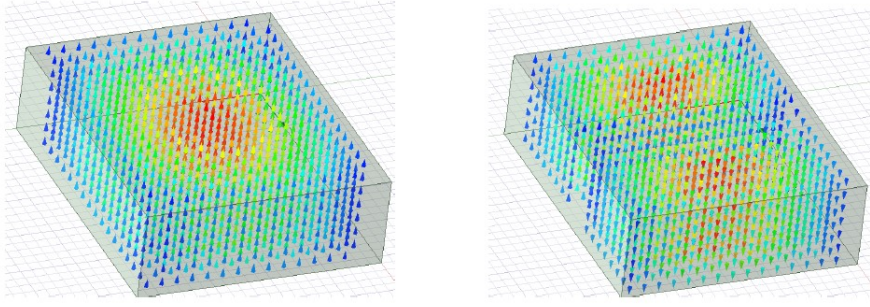


Figure 2.12: The first two modes of a 3D rectangular cavity, the TE_{101} (left) and TE_{201} (right)

2.3.3 Quality factor

The quality factor Q_0 is a parameter that quantifies the electromagnetic losses, it is defined as the ratio of the energy stored in the cavity and the power dissipated by it. Higher Q_0 implies lower energy dissipation, which means the resonator can store energy for longer periods. In a resonant cavity, we define the quality factor on a mode as

$$Q_0 = \frac{\nu_c}{\Delta\nu} = \frac{\omega_c}{\Delta\omega} \quad (2.60)$$

where ν_c is the resonant frequency, $\Delta\nu$ is the resonance width or full width at half maximum (FWHM) i.e. the bandwidth BW over which the power of vibration is greater than half the power at the resonant frequency. The resonator pulse frequency is $\omega_c = 2\pi\nu_c$ and $\Delta\omega$ is the half-power bandwidth.

From an experimental point of view, we have also the dissipation due to external source of noise, therefore we have to distinguish to different quality factor:

- Unloaded quality factor Q_0 : this refers to the quality factor of the resonator when it is isolated from external influences, so represents the intrinsic losses of the resonator itself.
- Loaded quality factor Q_{load} : it takes into account the effects of external components or coupling with the resonator. This includes any losses introduced by the connecting elements or materials surrounding the resonator.

Since powers are additive quantities, so are the inverse of the quality factors, and the loaded Q can be expressed as:

$$\frac{1}{Q_{\text{load}}} = \frac{1}{Q_0} + \frac{1}{Q_{\text{ext}}} \quad (2.61)$$

with Q_{ext} is the external quality factor, which accounts for losses due to factors external to the resonator itself. From the measurements we obtain the loaded Q , this is adjusted modifying the coupling of the cavity to the external devices.

2.4 Coupling of a transmon qubit and a cavity in dispersive regime

In this section we describe the principal behaviors of a transmon interacting with a 3D cavity resonator. A representation of the cavity-qubit system is made in figure 2.13.

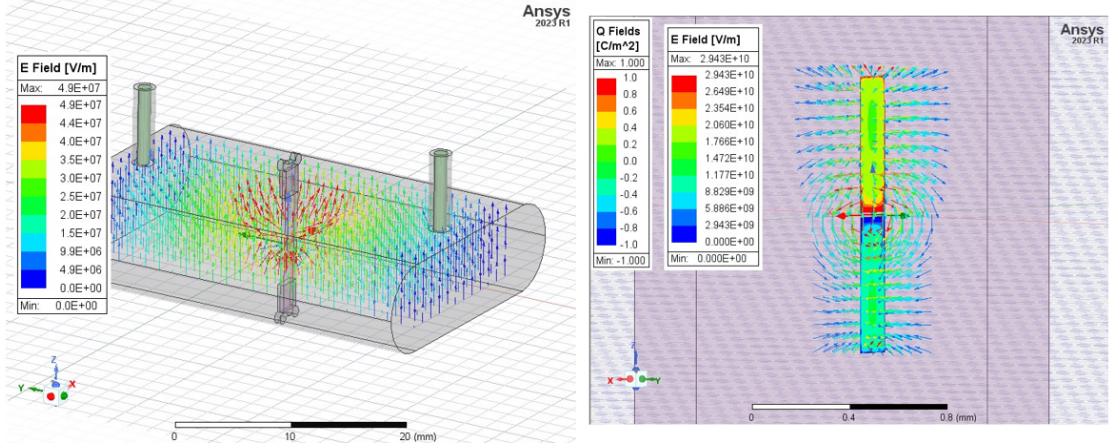


Figure 2.13: (Right) An ANSYS simulation of the system analyzed in this work. We see the qubit in the center of the cavity and the electric field of the first mode of the cavity TE_{101} . (left) a zoom of the qubit inside the cavity.

We consider only the first two qubit levels $|0\rangle$ and $|1\rangle$, corresponding to large anharmonicity α . The hamiltonian of the qubit is $\hat{H}_q = -\frac{\hbar\omega_q}{2}\sigma_z$, with ω_q the qubit frequency. We consider the cavity in the lowest mode (TE_{101}), as the dimension of the cavity ensure that the frequencies of the higher modes are significantly separated from the lowest frequency. The qubit is placed at the center of the cavity, where the field is maximum. The dimension of the qubit is much smaller than the dimension of the cavity therefore, with a good approximation, the qubit only interacts with the electromagnetic field at the center: $\vec{r} = (\frac{L_x}{2}, \frac{L_y}{2}, \frac{L_z}{2})$. For the TE_{101} , we have $\vec{n} = (1, 0, 1)$, the electric field of the cavity describe in equation 2.57 is $\hat{E} = E_0(\hat{b} + \hat{b}^\dagger)$. The Hamiltonian for the single mode of the cavity is $\hat{H} = \hbar\omega_c(\hat{b}^\dagger\hat{b} + \frac{1}{2})$, with ω_c the pulse frequency of the cavity. The operators \hat{b} and \hat{b}^\dagger destroy and create a photon inside the cavity.

The qubit interacts via its electric dipole \hat{d} (Figure 2.14), the interaction Hamiltonian is:

$$\hat{H}_{int} = \hat{d} \cdot \hat{E} \quad (2.62)$$

defining d as the magnitude of the qubit dipole aligned with electric field of the cavity. The effective dipole operator is represented as $\hat{d} = d\sigma_x = d(\sigma_+ + \sigma_-)$. where

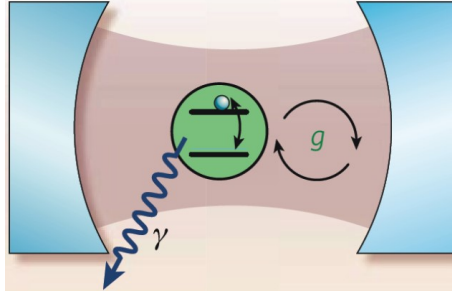


Figure 2.14: Scheme of the qubit interacting with the electric field via its electric dipole d . The purple color describes the electromagnetic field, the qubit state is colored in green. The interaction between cavity and qubit is indicated by the coupling constant g . Image from [13]

σ_x define a generic position on the block sphere. The operators σ_+ and σ_- acts as lowering and rising operator of the qubit state: $\hat{\sigma}_+ |1\rangle = |0\rangle$ and $\hat{\sigma}_- |0\rangle = |1\rangle$.

The interaction Hamiltonian is therefore

$$H_{int} = \hbar g_{01} (\hat{b} + \hat{b}^\dagger) (\sigma_+ + \sigma_-) \quad (2.63)$$

in which g_{01} quantify the interaction strength of qubit-cavity coupling energy. The indices 0 and 1 refers to the coupling with the two computational level of the qubit, but in general we can define the coupling strength g_{ij} between any two consecutive energy levels i and j of the qubit. Multiplying we have four terms

$$\hat{H}_{int} = \hbar g_{01} \left(\underbrace{\hat{\sigma}_+ \hat{b}^\dagger}_1 + \underbrace{\hat{\sigma}_- \hat{b}}_2 + \underbrace{\hat{\sigma}_+ \hat{b}}_3 + \underbrace{\hat{\sigma}_- \hat{b}^\dagger}_4 \right) \quad (2.64)$$

these terms define the energy exchange between the qubit and the cavity, in particular

1. The qubit emits a photon and consequently the energy state becomes excited.
2. The qubit absorbs a photon and consequently the energy state becomes excited.
3. Absorption of a photon and de-excitation of the qubit: energy $2\omega_q$ is supplied.
4. Emission of a photon and excitation of the qubit: energy $-2\omega_q$ is removed.

The last two terms are suppressed in perturbation theory because they have a small probability of occurring. Hence, unless ω_c and ω_q are too far apart, we neglect the last two processes.³

³This can be see in a formal way using a rotating wave approximation (RWA), with the rotating operator $\hat{U}(t) = e^{i\hat{H}_q t}$

The total Hamiltonian that describes a transmon qubit coupled with a cavity resonator is the **Jaynes-Cumming Hamiltonian**, this includes the qubit and cavity Hamiltonian and the interaction term:

$$H = \hbar\omega_c \left(\hat{b}^\dagger \hat{b} + \frac{1}{2} \right) + \frac{\hbar\omega_q}{2} \sigma_z + \hbar g_{01} \left(\hat{b}^\dagger \sigma_- + \hat{b} \sigma_+ \right) \quad (2.65)$$

This Hamiltonian is diagonalized as a block diagonal matrix. The total Hilbert space is infinite-dimensional as it is the result of the product $\mathcal{H}_q \otimes \mathcal{H}_r$, where $\dim \mathcal{H}_c = \infty$ (infinite oscillators). The interaction terms transforms these states into each other $|1, n\rangle \leftrightarrow |0, n+1\rangle$ as

$$\begin{aligned} \hat{a}^\dagger \hat{\sigma}_+ |1, n\rangle &= \sqrt{n+1} |0, n+1\rangle, \\ \hat{a} \hat{\sigma}_- |0, n+1\rangle &= \sqrt{n+1} |1, n\rangle, \end{aligned}$$

Considering that \hat{H}_0 is diagonal, while \hat{H}_I is off-diagonal, the Hamiltonian in matrix form becomes ($\hbar = 1$ for simplicity)

$$\hat{H} = \frac{1}{2}\omega_c I + \begin{pmatrix} -\frac{1}{2}\omega_q & & & & & \\ & \begin{pmatrix} \omega_c - \frac{1}{2}\omega_q & g_{01} \\ g_{01} & \frac{1}{2}\omega_q \end{pmatrix} & & & & \\ & & \dots & & & \\ & & & \begin{pmatrix} (n+1)\omega_c - \frac{1}{2}\omega_q & g_{01}\sqrt{n+1} \\ g_{01}\sqrt{n+1} & n\omega_c + \frac{1}{2}\omega_q \end{pmatrix} & & \\ & & & & & \dots \end{pmatrix} \begin{matrix} |0, 0\rangle \\ |0, 1\rangle \\ |1, 0\rangle \\ |0, n+1\rangle \\ |1, n\rangle \end{matrix}$$

where the initial term represents the zero-point energy and I is the 2x2 identity matrix. The **detuning** is defined as $\Delta = \omega_q - \omega_c$, we rewrite the generic block of the previous matrix as

$$\begin{pmatrix} (n+1)\omega_c - \frac{1}{2}\Delta & g_{01}\sqrt{n+1} \\ g_{01}\sqrt{n+1} & (n+1)\omega_c + \frac{1}{2}\Delta \end{pmatrix}$$

For a single block, the spectrum of the Hamiltonian is given by the following eigenvalues and eigenvectors:

$$\begin{aligned} E_+ &= (n+1)\omega_c + \frac{1}{2}\sqrt{\Delta^2 + 4(n+1)}, & |n_+\rangle &= \sin\theta_n |0, n+1\rangle + \cos\theta_n |1, n\rangle, \\ E_- &= (n+1)\omega_c - \frac{1}{2}\sqrt{\Delta^2 + 4(n+1)}, & |n_-\rangle &= \cos\theta_n |0, n+1\rangle - \sin\theta_n |1, n\rangle; \end{aligned}$$

with the addition of the single state $|0, 0\rangle$ with energy $E_0 = -\frac{\Delta}{2}$. The states $|n_-\rangle$ and $|n_+\rangle$ are called **dressed states**, and the angle θ_n is defined as

$$\tan 2\theta_n = \frac{2\sqrt{n+1}}{\Delta}.$$

quantifies the hybridization of the $|n_+\rangle$ and $|n_-\rangle$ states.

The temporal evolution of the system realizes oscillation on the pair of dressed states: each state behaves like a two-level system that coherently oscillates in cycles of photon absorption and emission. This oscillations are called **Rabi oscillations**.

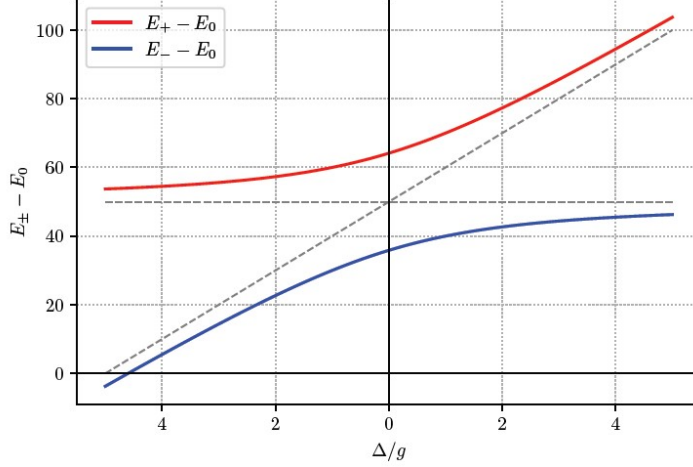


Figure 2.15: Difference in energy of dressed states with the ground state as a function of detuning ($\Delta = \Delta_d$). Note that the minimum energy difference between E_+ and E_- is found at $\Delta = 0$, while the greatest difference is given when Δ diverges. The horizontal asymptote is found in correspondence of limits: $\lim_{\Delta \rightarrow -\infty} (E_+ - E_0) = \lim_{\Delta \rightarrow +\infty} (E_- - E_0) = (n + 1)\omega_c$. In this case, the following values were set: $\omega_c = 25$, $g = 10$, $n = 1$.

For $\Delta = 0$ ($\omega_c = \omega_q$) we have the **resonance regime** where $\theta_n = \frac{\pi}{4}$, so $\cos \theta_n = \sin \theta_n = \frac{1}{\sqrt{2}}$. There is maximum hybridization of the states since

$$|n_{\pm}\rangle = \frac{|0, n + 1\rangle \pm |1, n\rangle}{\sqrt{2}};$$

The energy difference is the smallest possible and depends on n :

$$E_{\pm} = (n + 1)\omega_c \pm g_{01}\sqrt{n + 1}.$$

The opposite case is the interesting one: the **dispersive regime**. It is reached for $\Delta \gg g$ and $\theta_n \ll 1$ and corresponds to the minimum hybridization. The original states remain almost unchanged except for small corrections.

$$\begin{aligned} |n_-\rangle &= |0, n + 1\rangle + \dots, \\ |n_+\rangle &= |1, n\rangle + \dots; \end{aligned}$$

we notice that this behavior is expected since $\frac{\Delta}{g} \rightarrow \infty$ equivalently means that $\Delta = \text{const}$ and $g \simeq 0$: we are close to the free case where the qubit and the

electromagnetic radiation are almost decoupled. Keeping small corrections in the states $|n_+\rangle$ and $|n_-\rangle$, we expand the square root in $\frac{g^2}{\Delta^2}$, we have

$$\begin{aligned} E_{\pm} &= (n+1)\omega_c \pm \frac{1}{2}\sqrt{\Delta^2 + 4g_{01}^2(n+1)} \\ &= (n+1)\omega_c \pm \frac{\Delta}{2}\sqrt{1 + \frac{4g_{01}^2}{\Delta^2}(n+1)} \\ &= (n+1)\omega_c \pm \frac{\Delta}{2}\left(1 + \frac{2g_{01}^2}{\Delta^2}(n+1) + \dots\right) \\ &= (n+1)\omega_c \pm \left(\frac{\Delta}{2} + \frac{g_{01}^2}{\Delta}(n+1) + \dots\right); \end{aligned}$$

In this way, we built an effective Hamiltonian that describes the system.

$$\hat{H}_{\text{eff}} = \omega_c \left(\hat{b}^\dagger \hat{b} + \frac{1}{2}\right) - \frac{\omega_q}{2} \hat{\sigma}_z - \frac{g_{01}^2}{\Delta} \left(\hat{b}^\dagger \hat{b} + \frac{1}{2}\right) \hat{\sigma}_z + \frac{g_{01}^2}{2\Delta} I \quad (2.66)$$

indeed solving this Hamiltonian for the dressed states, we find the energy we expect in the dispersive regime:

$$\begin{aligned} \hat{H}_{\text{eff}} |0, n+1\rangle &= \omega_c \left(n+1 + \frac{1}{2}\right) - \frac{\omega_q}{2} - \frac{g_{01}^2}{\Delta}(n+1) |0, n+1\rangle \\ &\Rightarrow \omega_c(n+1) - \frac{\Delta}{2} - \frac{g_{01}^2}{\Delta}(n+1) \equiv E_-, \\ \hat{H}_{\text{eff}} |0, n\rangle &= \omega_c \left(n + \frac{1}{2}\right) + \frac{\omega_q}{2} + \frac{g_{01}^2}{\Delta} \left(n + \frac{1}{2}\right) + \frac{g_{01}^2}{2\Delta} |1, n\rangle \\ &\Rightarrow \omega_c(n+1) + \frac{\Delta}{2} + \frac{g_{01}^2}{\Delta}(n+1) \equiv E_+. \end{aligned}$$

This Hamiltonian is created considering only $|0\rangle$ and $|1\rangle$ qubit state, ignoring the higher non-computational energy levels. This is a good approximation to understand the cavity-qubit behavior, but generally there is an influence of the other levels and it is useful consider its. A more general solution is obtained from second-order perturbation theory, where we also consider the third energy level. The Hamiltonian of a dispersively coupled system is [15]:

$$\hat{H} = \hbar(\omega'_c - \chi\sigma_z)b^\dagger b + \frac{\hbar}{2}\omega'_{01}\sigma^z \quad (2.67)$$

where ω'_c and ω'_{01} are the frequencies of the cavity and the qubit renormalized by the interaction terms (in this notation $\omega_q = \omega_{01}$).

$$\omega'_c = \omega_c - \frac{\chi_{12}}{2} \quad \omega'_{01} = \omega_{01} + \chi_{01} \quad (2.68)$$

The term χ is the total dispersive shift and is defined as

$$\chi = \chi_{01} - \frac{\chi_{12}}{2} \quad (2.69)$$

with coupling χ_{ij} given by

$$\chi_{ij} = \frac{g_{ij}^2}{\Delta_{ij}} \quad (2.70)$$

with $\Delta_{ij} = \omega_{ij} - \omega_c$. The terms g_{ij} and $\omega_{ij} = \omega_i - \omega_j$ are the coupling and the pulse frequency difference between two consecutive qubit levels i and j .

The dispersive regime is necessary for working on a qubit because it is needed to decouple the qubit from external systems and keep the relaxation time unchanged. We can also implement a quantum non-demolition measurement. It consist of a measure of the state of a qubit without modifying it: we can determine the qubit's state by measuring the cavity's frequency. This is seen in the Hamiltonian since the cavity energy depends on a frequency that is shifted by a constant χ depending on the qubit's state.

Similarly, ω_q is redefined following the interaction with the electromagnetic field. Also the number of photons inside the cavity influence the qubit frequency. This is due to the term proportional to the σ_z and $\hat{b}^\dagger \hat{b}$, modifying the number of photon $\hat{b}^\dagger \hat{b}$ we modify the qubit state σ_z .

2.4.1 Capacity matrix

In a transmon qubit we define the total capacitance of the system from the Maxwell capacity matrix. A schematic of the capacitance network of the device is shown in Figure 2.16. The Maxwell capacity matrix is defined considering the capacitances between the different component of the qubit. It is defined as

$$C^M = \begin{pmatrix} C_{11} & C_{12} \\ C_{21} & C_{22} \end{pmatrix} \quad (2.71)$$

in which the components are given by:

$$C_{12} = C_{21} = C_{\text{pads}}, \quad C_{11} = C_{\text{up}} + C_{\text{pads}}, \quad C_{22} = C_{\text{down}} + C_{\text{pads}}. \quad (2.72)$$

where C_{up} and C_{down} are the capacitances between the single pads and an infinite ground plane while C_{pads} is the capacity between the two pads.

The system total capacity is derived from the Maxwell capacity matrix as follow. The relation between the charge and the potential is $\mathbf{Q} = \mathbf{C}^M \mathbf{V}$:

$$\begin{pmatrix} Q_1 \\ Q_2 \end{pmatrix} = \begin{pmatrix} C_{11} & C_{12} \\ C_{21} & C_{22} \end{pmatrix} \begin{pmatrix} V_1 \\ V_2 \end{pmatrix}, \quad (2.73)$$

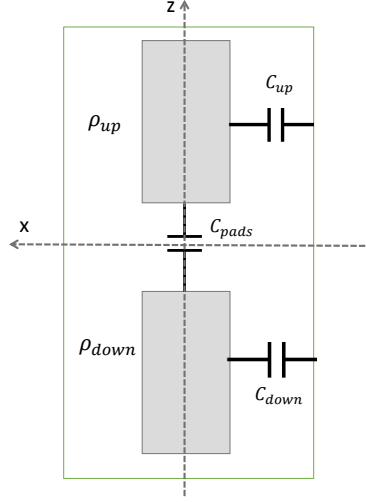


Figure 2.16: Scheme of the capacitances and the charge density distribution of the transmon qubit. The two rectangles represent the upper pad (1) and the bottom pad (2) of the qubit. The charge of the pads is $Q_1 = -Q_2 = Q$ for the symmetry of the system, with a charge distribution $\rho(\vec{r}) = \rho_{up}(\vec{r}) + \rho_{down}(\vec{r})$. The green rectangle represents an infinite ground plane. The capacitances between the pads and this plane are C_{up} and C_{down} , while the capacitance between the two pads is C_{pads} .

where Q_1 and Q_2 are the charges of the pad up and pad down respectively and V_1 and V_2 are the corresponding charge potentials. Defining the inverse matrix $\mathbf{E} = (\mathbf{C}^M)^{-1}$, the relation become:

$$\begin{pmatrix} V_1 \\ V_2 \end{pmatrix} = \begin{pmatrix} E_{11} & E_{12} \\ E_{21} & E_{22} \end{pmatrix} \begin{pmatrix} Q_1 \\ Q_2 \end{pmatrix} \quad (2.74)$$

with the corresponding equation:

$$\begin{cases} V_1 = E_{11}Q_1 + E_{12}Q_2 \\ V_2 = E_{21}Q_1 + E_{22}Q_2 \end{cases} \quad (2.75)$$

The voltage difference between the pads is:

$$\Delta V = V_1 - V_2 = (E_{11} - E_{12} + E_{22} - E_{21})Q \quad (2.76)$$

considering $Q = Q_1 = -Q_2$ due to the symmetry of the system. The current flowing between the pads is given by $I = -\frac{dQ}{dt}$, therefore $\frac{dI}{dt} = -\frac{d^2Q}{dt^2}$. Considering a linear inductance L between the pads, the voltage is:

$$\Delta V = L \frac{d^2Q}{dt^2} \quad (2.77)$$

Combining 2.76 and 2.77, results in

$$\frac{d^2Q}{dt^2} = \frac{E_{11} - E_{12} + E_{22} - E_{21}}{L} Q \quad (2.78)$$

As the transmon in the first approximation is an LC harmonic oscillator, we compare it with 2.78 and see that

$$C = (E_{11} - E_{12} + E_{22} - E_{21})^{-1} \quad (2.79)$$

The formula 2.79 is written depending on the components of the Maxwell capacity matrix \mathbf{C}^M , obtaining the relation for the effective total capacity for the transmon:

$$C = \frac{C_{11}C_{22} - C_{12}C_{21}}{C_{11} + C_{12} + C_{21} + C_{22}} \quad (2.80)$$

2.4.2 Coupling strength

For a transmon qubit we define a formula to calculate the coupling constant g_{01} [15, 16]. For the TE_{110} mode of the cavity⁴, the electric field \vec{E} is oriented parallel to the z-axis of figure 2.16. The corresponding electric potential is given by $V_0(\vec{r}) = \hat{E} \cdot z$. The interaction Hamiltonian is given by the interaction between the electric field and the charges. Considering the charge of the pads $Q_1 = -Q_2 = Q$ for the symmetry of the system, with a charge distribution $\rho(\vec{r}) = \rho_{\text{up}}(\vec{r}) + \rho_{\text{down}}(\vec{r})$, we write the Hamiltonian as

$$H_{\text{int}} = \int \rho(\vec{r}) V_0(\vec{r}) d\vec{r} = -\hat{E} \cdot Q \cdot d_{\text{eff}} \quad (2.81)$$

where we define the effective distance as

$$d_{\text{eff}} = \int_{A_{\text{up}}} \left(\frac{\rho_{\text{up}}(\vec{r})}{|Q|} \right) \cdot z d\vec{r} + \int_{A_{\text{down}}} \left(\frac{\rho_{\text{down}}(\vec{r})}{|Q|} \right) \cdot z d\vec{r} \quad (2.82)$$

with A_{up} and A_{down} are the areas of the upper and lower pads. The effective distance is the geometrical distance between the center of the two pads taking into account the charges distribution.

Considering the quantize electric field, the Hamiltonian 2.81 is:

$$H = 2e\hat{n} \cdot d_{\text{eff}} \cdot E_0(\hat{b}^\dagger + \hat{b}) \quad (2.83)$$

This Hamiltonian is compared to the interaction part of the Jaynes-Cumming Hamiltonian

$$H_{\text{int}} = \hbar g_{01} \left(\hat{b}^\dagger \sigma^- + \hat{b} \sigma^+ \right) \quad (2.84)$$

⁴Notice that in literature the first mode is TE_{101} , in this case is TE_{110} only because we invert the y and z axis, both in Figure 2.16 and in the next chapter

in both case we want to compute $\langle 1|H|0\rangle$, with $|1\rangle$ and $|0\rangle$ the two states of the qubit. We consider the operators $\sigma^- = |0\rangle\langle 1|$ and $\sigma^+ = |1\rangle\langle 0|$ and $\hat{n} = a^\dagger a$ with the relations $a|n\rangle = \sqrt{n}|n-1\rangle$ and $a^\dagger|n\rangle = \sqrt{n+1}|n+1\rangle$. Equalizing the solutions of the two Hamiltonians we obtain the value of the coupling constant:

$$g_{01} = \frac{2e \cdot d_{\text{eff}} \cdot E_0}{\hbar} \frac{1}{\sqrt{2}} \left(\frac{E_J}{8E_C} \right)^{\frac{1}{4}}. \quad (2.85)$$

with E_0 , E_J and E_C are defined respectively in equations 2.58, 2.7 and 2.20.

2.5 Qubit driving

In this section, we discuss the dynamics of a qubit driven continuously with a coherent control signal. Since the signal can be seen as a classical oscillating electric field, we use a semi-classical approach considering only the qubit dynamics, ignoring the cavity. This is a good approximation because we assume that the qubit drive is off-resonant with the cavity transition.

2.5.1 Dynamics of a driven qubit

When the qubit is in contact with the electromagnetic field given by the signal, it begins to oscillate at the same frequency. In terms of the Bloch sphere it involves moving this system along the surface of the sphere.

We consider again the two-level Hamiltonian of the qubit $\hat{H}_q = -\frac{\hbar\omega_q}{2}\sigma_z$ and the interaction given by the electric dipole moment as defined in equation 2.62: $\hat{H}_{\text{int}} = -\vec{E}(t) \cdot \hat{d}$. The electric field of a classical oscillating signal is $\vec{E}(t) = E_{\text{amp}} \cos(\omega_d t + \phi)$, with E_{amp} the amplitude of the signal. The total Hamiltonian is

$$\hat{H} = \hat{H}_q - \vec{E}(t) \cdot \hat{d} = -\frac{\hbar\omega_q}{2}\sigma_z - \Omega \cos(\omega_d t + \phi)\sigma_x \quad (2.86)$$

where ω_d is driving frequency of the qubit and $\Omega = E_{\text{amp}} \cdot d$ is a 2x2 matrix that quantifies the strength of the interaction. To solve the Hamiltonian, we use again a rotating wave approximation: we move from the lab frame to a rotating frame and cancel the time-dependent terms.

The rotation is given by the operator $U = e^{-i\frac{\hbar\omega_d}{2}t}$, the Hamiltonian in the rotating frame \hat{H}_{rf} is evaluated with the following formula:

$$\hat{H}_{\text{rf}} = U H U^\dagger - iU\dot{U}^\dagger \quad (2.87)$$

with \dot{U} the time derivative of the operator. Removing the oscillating terms for the RWA, we find a time independent Hamiltonian given by:

$$\hat{H}_{\text{rf}} = -\frac{\hbar\Delta_d}{2}\sigma_z - \left(\frac{\Omega}{2}e^{i\phi}\sigma_+ + \frac{\Omega}{2}e^{-i\phi}\sigma_- \right) \quad (2.88)$$

where $\Delta_d = \omega_q - \omega_d$ is the detuning between the drive frequency of the signal and the qubit frequency. $\Delta_d = 0$ corresponds to the resonance.

The aim is to connect the time evolution of a state to the rotation of the state of the qubit on the Bloch sphere. Even though the Hamiltonian is time independent, the time evolution of a state in the rotating frame is given by

$$|\tilde{\psi}(t)\rangle = e^{-i\hat{H}_{\text{eff}}t} |\tilde{\psi}(0)\rangle. \quad (2.89)$$

with $|\tilde{\psi}(t)\rangle$ the state in the rotating frame and $U(t) = e^{-iHt}$ the time evolution operator. The Hamiltonian 2.88 can be written as:

$$\tilde{H}_{\text{rf}} = -\frac{1}{2} (\hbar\Delta_d\sigma_z + \Omega \cos\phi\sigma_x - \Omega \sin\phi\sigma_y) \equiv -\frac{\tilde{\Omega}}{2} \vec{a} \cdot \vec{\sigma},$$

where

$$\vec{a} = \frac{1}{\tilde{\Omega}} (\Omega \cos\phi, -\Omega \sin\phi, \hbar\Delta_d) \quad \text{with} \quad \tilde{\Omega} = \sqrt{\Omega^2 + \Delta_d^2} \quad (2.90)$$

where $\tilde{\Omega} = \sqrt{\Omega^2 + \Delta_d^2}$ is called the **Rabi frequency** and control the qubit oscillation. Therefore the time evolution operator is rewrite as:

$$U(t) = e^{-i\hat{H}t} = e^{i\frac{\tilde{\Omega}}{2}(\vec{a}\cdot\vec{\sigma})t} = I \cos\left(\frac{\tilde{\Omega}t}{2}\right) - i \sin\left(\frac{\tilde{\Omega}t}{2}\right) (\vec{\sigma} \cdot \vec{a}); \quad (2.91)$$

this operator corresponds to a rotation of the qubit along the Bloch sphere: the temporal evolution $R_{\vec{a}}(-\Omega t)$ performs a rotation of angle $-\Omega t$ around the direction identified by the vector \vec{a} . The parameters that describe the details of the interaction with the external oscillating radiation are Δ_d , $\tilde{\Omega}$, and ϕ .

Now we calculate the probability that at time t , the qubit undergoes a transition $|0\rangle \rightarrow |1\rangle$. Supposing the system in the initial state $|\psi(0)\rangle = |0\rangle$, the probability is:

$$P(t)_{0 \rightarrow 1} = \left| \langle 1 | e^{-i\hat{H}t} | 0 \rangle \right|^2 = \left| \langle 1 | \cos\left(\frac{\tilde{\Omega}t}{2}\right) + i \sin\left(\frac{\tilde{\Omega}t}{2}\right) \vec{\sigma} \cdot \vec{a} | 0 \rangle \right|^2$$

the first term is zero, while the second, $\sigma_x |0\rangle = |1\rangle$ and $\sigma_y |0\rangle = i |1\rangle$, receives contributions only from σ_x and σ_y . Thus, we write

$$\begin{aligned} P(t)_{0 \rightarrow 1} &= \left| i \sin\left(\frac{\tilde{\Omega}t}{2}\right) \frac{\Omega}{\tilde{\Omega}} e^{-i\phi} \right|^2 \\ &= \frac{\Omega^2}{\tilde{\Omega}^2} \sin^2\left(\frac{\tilde{\Omega}t}{2}\right), \end{aligned}$$

where in the second line we used the components of \vec{a} in equation 2.90. Inserting the expression for $\tilde{\Omega}$, we obtain the **Rabi formula**:

$$P(t)_{0 \rightarrow 1} = \frac{\Omega^2}{\Omega^2 + \Delta_d^2} \sin^2 \left(\frac{\sqrt{\Omega^2 + \Delta_d^2}}{2} t \right). \quad (2.92)$$

This equation defines the probability at time t that applying an external oscillating perturbation with frequency ω_d , amplitude Ω and detuning Δ_d results in a transition $|0\rangle \rightarrow |1\rangle$. The qubit driven by an external signal at pulse ω_d makes continuous oscillations called **Rabi oscillation**. As we see in Figure 2.17, the qubit oscillates at the Rabi frequency $\tilde{\Omega}$. The amplitude is defined by Ω and the detuning Δ_d .

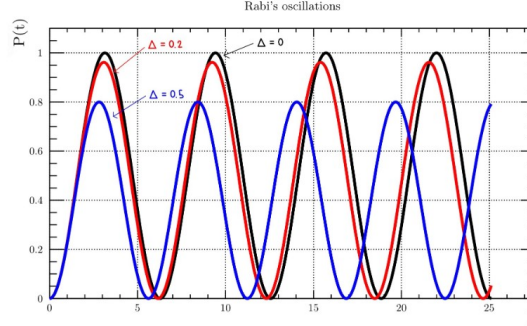


Figure 2.17: Rabi oscillations for $\Omega = 1$. It is evident how the probability of the system oscillates over time. The closer the system is to resonance ($\Delta_g = 0$), the closer the peaks will be to 1, and therefore the greater the probability of finding the system in $|1\rangle$.

In general we discuss the dynamics of the qubit on the Bloch sphere. We write the state in the initial frame $|\psi(t)\rangle$ with the relation:

$$|\psi(t)\rangle = e^{\frac{i}{2}\hbar\omega_d\sigma_3 t} R_{\vec{n}}(-\Omega t)|\tilde{\psi}(0)\rangle$$

when there is no oscillating field ($\omega_d = 0$), the vector $\vec{a} = (0, 0, \Delta_d/\tilde{\Omega})$, this means that the state continues to have a precession z with the qubit's natural frequency on the lab frame. This is removed going to the rotating frame.

In resonance condition ($\Delta = 0$), we have $\vec{a} = (\cos \phi, -\sin \phi, 0)$. In the rotating frame, the qubit rotates with frequency $\tilde{\Omega}$ in the plane perpendicular to \vec{a} , continuously oscillating between $|0\rangle$ and $|1\rangle$. In the lab frame, the qubit precesses along the sphere, as we see in Figure 2.18(a). However, for $\Delta \neq 0$, the vector \vec{a} has three non-zero components. Consequently, starting from $|0\rangle$, the qubit in the rotating frame forms a circle that never reaches state $|1\rangle$. Also in the lab frame the qubit precesses never going to state $|1\rangle$ (Figure 2.18(b)).

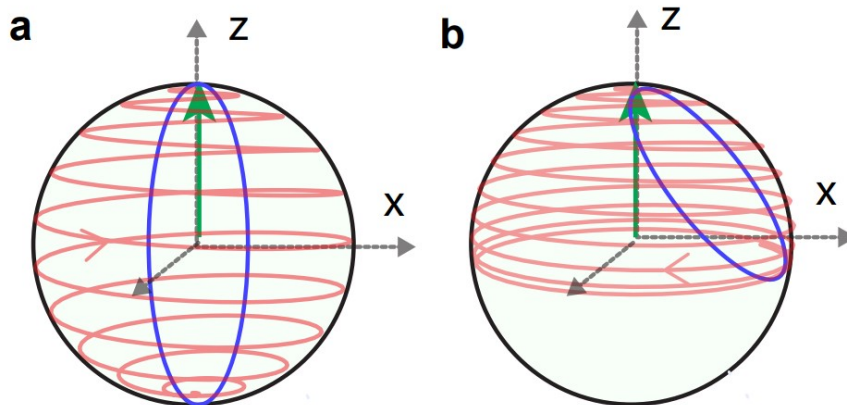


Figure 2.18: Driven qubit state evolution in the Bloch sphere. The red (blue) line shows the evolution of a driven qubit in the lab frame (rotating frame of the drive) for an on-resonant drive (a) and for a detuned drive (b). Figure from [13].

From an experimental point of view, the temporal evolution is used to control the individual qubit and move it on the Bloch sphere. This technique is really useful for time-domain characterization experiments made in Chapter 4. We can drive the qubit for a precise time, generating a pulse that brings the qubit to some precise state positions. Two pulse that we send to a qubit are the π -pulse and the $\frac{\pi}{2}$ -pulse. The π -pulse brings the state from $|0\rangle$ to $|1\rangle$, from the top to the bottom of the sphere. The $\frac{\pi}{2}$ -pulse brings the state from $|0\rangle$ into the superposition $|\psi\rangle = \frac{|0\rangle + i|1\rangle}{\sqrt{2}}$ where $|0\rangle$ and $|1\rangle$ contribute equally (Figure 2.19). This corresponds going from the top to the center of the the block sphere.

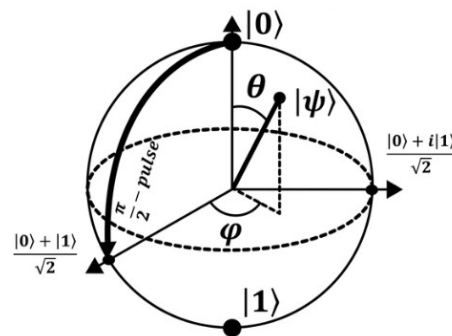


Figure 2.19: Scheme of a $\frac{\pi}{2}$ -pulse, the π -pulse takes the state from $|0\rangle$ to $|1\rangle$.

2.5.2 Dynamics in presence of dissipation

In the last section we assumed that the qubit is an ideal closed system that undergoes unitary evolution given by the Schrodinger equation. In a real case the qubit

is an open systems, that interacts with the environment, generating dissipative process. For quantum systems, this interaction results in energy dissipation and decoherence. In order to account for non-unitary and dissipative processes in qubit dynamics, we consider the Heisenberg picture where the evolution of the system is described by the evolution of a density matrix.

We study the total system of the qubit H_q interacting with the environment H_E , the total Hamiltonian is given by $\tilde{H} = H_q \otimes H_E$. We define $\tilde{\rho}$ as the total density matrix of \tilde{H} . The term $\tilde{\rho} = \rho \otimes \rho_E$, where ρ is the density matrix of the qubit and ρ_E describe the environment.

In general the evolution of density matrix $\rho = \begin{pmatrix} |\alpha|^2 & \alpha\beta^* \\ \alpha^*\beta & |\beta|^2 \end{pmatrix}$ for a state $|\psi\rangle$ that evolves with a unitary operator U is described by:

$$\rho = |\psi\rangle\langle\psi| \rightarrow U |\psi\rangle\langle\psi| U^\dagger = U\rho U^\dagger$$

We express the evolution of the total system with the density matrix

$$\mathcal{E}(\rho) = \text{Tr}_E[U(\rho \otimes \rho_E)U^\dagger] \quad (2.93)$$

which provides an effective description of the qubit with dissipation due to environment. The term Tr_E is the partial trace, it is needed to ignore the degrees of freedom of the environment and focusing on the physics of the qubit.

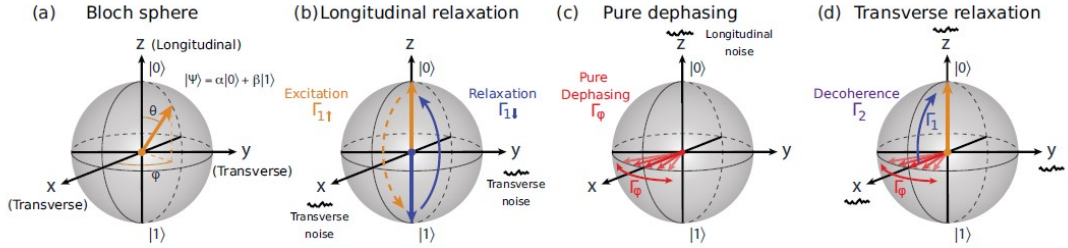


Figure 2.20: Transverse and longitudinal noise represented on the Bloch sphere. (a) Bloch sphere for a generic state. (b) Longitudinal relaxation results from energy exchange between the qubit and its environment. (c) Pure dephasing in the transverse plane arises from longitudinal noise along the z axis that fluctuates the qubit frequency. (d) Transverse relaxation that results in a loss of coherence due to a combination of energy relaxation and pure dephasing.

The dissipation process that described by two relaxation rates, that correspond to a longitudinal and transversal damping on the block sphere [11].

- **Longitudinal relaxation rate Γ_1 :** The longitudinal relaxation rate describes depolarization along the qubit quantization axis. Depolarization occurs due to energy exchange with the environment, generally leading to both

an up transition rate Γ_1^- (excitation from $|0\rangle$ to $|1\rangle$), and a down transition rate Γ_1^+ (relaxation from $|1\rangle$ to $|0\rangle$). Together, these form the longitudinal relaxation rate Γ_1 :

$$\Gamma_1 = \frac{1}{T_1} = \Gamma_1^+ + \Gamma_1^-. \quad (2.94)$$

the term T_1 is the longitudinal relaxation time, called also **lifetime of the qubit**. We work with the qubit in cold environment, enough cold to neglect excitation ($\Gamma_1^- = 0$).

- **Transversal relaxation rate Γ_2** It is given by

$$\Gamma_2 = \frac{1}{T_2} = \frac{\Gamma_1}{2} + \Gamma_\varphi \quad (2.95)$$

with T_2 the transversal relaxation time, called also **decoherence time**. The formula depends on pure dephasing rate and on transverse noise already described. The pure dephasing rate describes depolarization in the xy plane of the Bloch sphere. The **dephasing time** is defined as $T_\varphi = \frac{1}{\Gamma_\varphi}$ and does not depend on energy exchange.

The complete dynamic of a qubit interacting with the environment is described by the Bloch-Redfield density matrix:

$$\rho = \begin{pmatrix} |\alpha|^2 & \alpha\beta^* \\ \alpha^*\beta & |\beta|^2 \end{pmatrix} \rightarrow \mathcal{E}_{\text{BR}}(\rho) = \begin{pmatrix} 1 + (|\alpha|^2 - 1)e^{-\Gamma_1 t} & \alpha\beta^* e^{i\Delta\omega t} e^{-\Gamma_2 t} \\ \alpha^*\beta e^{-i\Delta\omega t} e^{-\Gamma_2 t} & |\beta|^2 e^{-\Gamma_1 t} \end{pmatrix} \quad (2.96)$$

with the longitudinal decay function $\exp(-\Gamma_1 t)$, which accounts for longitudinal relaxation of the qubit and the transverse decay function $\exp(-\Gamma_2 t)$, which accounts for transverse decay of the qubit. The term $e^{i\Delta\omega t}$ depends on the driving frequency and it is relevant only when the qubit frequency ω_q differs from the driving frequency ω_d . This matrix is valid for $t \gg (T_1, T_2)$, in the assumption that the environmental temperature is low enough that thermal excitations of the qubit from the ground to excited state rarely occur. In chapter 4, we will see how to calculate the T_1 and T_2 from the qubit characterization.

2.5.3 Loss participation ratios

We see that the lifetime T_1 is the spontaneous relaxation time of the qubit from the excited state to the ground state in presence of energy exchange. For the transmon qubit we have two main phenomena that contributes to the lifetime [17–19]. The first are the losses of the electromagnetic field in the dielectric media around the qubit, corresponding to an intrinsic lifetime T_{int} . The second are losses via a coupling to the cavity corresponding to a lifetime T_{purcell} . The value of the lifetime is

$$T_1^{-1} = T_{\text{int}}^{-1} + T_{\text{purcell}}^{-1} \quad (2.97)$$

The losses over the cavity due to the Purcell effect are given by [15]:

$$T_{purcell} = \frac{\Delta^2}{g_{01}^2 \kappa} \quad (2.98)$$

where $\Delta = \omega_c - \omega_q$ is the difference in resonance frequency of the cavity and qubit and $\kappa = \omega_r/2Q_{cav}$ is the decay rate of the resonator where Q_{cav} is the quality factor of the cavity.

The dielectric losses are described in terms of an intrinsic quality factor

$$Q_{int} = \omega_q T_{int} \quad (2.99)$$

of the transmon with contributions from different spatial regions i , like the silicon substrate and the layers of oxide on the surfaces [18]:

$$Q_{int}^{-1} = \sum_i P_i \tan \delta_i. \quad (2.100)$$

where P_i are the participation ratios and $\tan \delta_i$ are the material-specific loss tangents. Due to a much larger loss tangent of the surface oxide layers compared to the silicon substrate and aluminium [18], only the surface layers were considered in our analysis. As they are only about 5 nm thick, the electric field is approximated as constant over their thickness.

The participating ratios are therefore given by:

$$P_i = \frac{\epsilon_0 \epsilon_i}{2W} \int_{A_i} d\vec{r} \tau_i |E(\vec{r})|^2 = \frac{\epsilon_0 \epsilon_i \tau_i C_{tot}}{q^2} \int_{A_i} d\vec{r} |E(\vec{r})|^2 \quad (2.101)$$

where ϵ_i are the dielectric constants, τ_i is the thickness of the layer and A_i the layer surface. The participation ratio is normalized by the total capacitor energy $W = \frac{q^2}{2C_{tot}}$, with q the charge of a single pad. The $E(\vec{r})$ is the electric field on the surface A_i that is the sum of a parallel and a perpendicular component $E(\vec{r})^2 = E(\vec{r})_{\parallel}^2 + E(\vec{r})_{\perp}^2$.

The surface layers considered are the metal-air (MA), metal-substrate (MS) and substrate-air (SA), the following contributions are derived [17]:

$$P_{MS} = \frac{\epsilon_0 \epsilon_S^2}{\epsilon_{MS}} t_{MS} \frac{C_{tot}}{q^2} \int_{MS} d\vec{r} |E_{0\perp}|^2 \quad (2.102)$$

$$P_{MA} = \frac{\epsilon_0}{\epsilon_{MA}} t_{MA} \frac{C_{tot}}{q^2} \int_{MA} d\vec{r} |E_{0\perp}|^2 \quad (2.103)$$

$$P_{SA} = \epsilon_0 t_{SA} \frac{C_{tot}}{q^2} (\epsilon_{SA} \int_{SA} d\vec{r} |E_{0\parallel}|^2 + \epsilon_{SA}^{-1} \int_{SA} d\vec{r} |E_{0\perp}|^2) \quad (2.104)$$

where E_0 is the electric field in air and considering the dielectric constant of air as $\epsilon = \epsilon_0$. To calculate these contributions we used the boundary conditions of the electric field for the perpendicular and parallel components at the interface:

$$E_{1\parallel} = E_{2\parallel} \quad (2.105)$$

$$\epsilon_1 E_{1\perp} = \epsilon_2 E_{2\perp} \quad (2.106)$$

with 1 and 2 the two materials that constitute the interface.

2.6 Scattering parameters

In order to characterize a network in radio-frequency we introduce the scattering matrix formalism [14]. In our set-up we have a resonant RF cavity connected to a Virtual Network analyzer (VNA). The VNA introduce an electromagnetic signals inside the cavity that interacts with the cavity and the devices inside it. Using the VNA, we measures the power delivered to and from the cavity. Two antennas are coupled with the cavity, creating a two port network. The scattering matrix relates the amplitudes of the incident waves with the ones of the reflected waves from the ports.

We define the scattering matrix for a two port network. We consider a signal given by the following plane waves for voltages and currents, considering z as the direction of propagation:

$$V(z) = V_0^+ e^{-j\beta z} + V_0^- e^{j\beta z}; \quad (2.107)$$

$$I(z) = I_0^+ e^{-j\beta z} - I_0^- e^{j\beta z}; \quad (2.108)$$

where V_0^+ and I_0^+ are complex amplitudes of the incident wave, and V_0^- and I_0^- are complex amplitudes of the reflected wave. $\beta = 2\pi/\lambda$ is the propagation constant (or wave number) and λ the wavelength.

The idea is that the voltage outgoing from a port is due to a fraction of the incident wave into the same port and a fraction of the incident waves entering the network from the other port. The scattering matrix S define the relation of the voltage between the outgoing and the incident waves:

$$\begin{pmatrix} V_1^- \\ V_2^- \end{pmatrix} = \begin{pmatrix} S_{11} & S_{12} \\ S_{21} & S_{22} \end{pmatrix} \begin{pmatrix} V_1^+ \\ V_2^+ \end{pmatrix} \quad (2.109)$$

with V the voltage, 1 or 2 the number of the port and $-$ or $+$ the outgoing or the incident wave. The elements of the matrix S_{ij} are the scattering parameters of the ports i and j . The values of the parameters are

$$S_{ij} = \frac{V_i^-}{V_j^+}$$

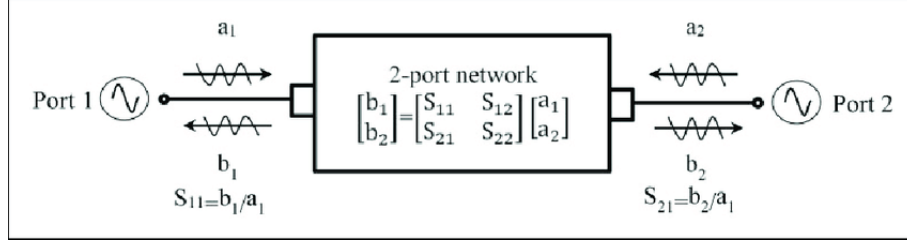


Figure 2.21: A scheme of the scattering matrix and parameters, b_i refers to the output wave of the port i and a_i to the input one.

A scheme of the scattering matrix and scattering parameters is shown in Figure 2.21. In particular, we have four scattering parameters:

- **S11:** The reflection coefficient, it represents the ratio of the reflected wave voltage to the incident wave voltage when only one port of a two-port network is excited.
- **S22:** Similar to S11, but it represents the reflection coefficient when the other port of the two-port network is excited.
- **S21:** This is the forward transmission coefficient, representing the ratio of the transmitted wave voltage to the incident wave voltage when one port is excited and the other is terminated with its characteristic impedance.
- **S12:** Similar to S21, but it represents the transmission coefficient when the other port is excited.

2.7 Devices Fabrication

In this section, we present the fabrication procedures of the devices studied in this thesis. The first device includes several Josephson junctions fabricated at CNR-IFN in Rome. These junctions are characterized with DC current measurements in Chapter 4. The second device is the transmon qubit fabricated at the Technology Innovation Institute (TII) in Abu Dhabi. The design of the qubit is used for performing electromagnetic simulations via ANSYS software in Chapter 3, while a complete characterization of the qubit is made in Chapter 4.

The final device is the transmon qubit fabricated at CNR-IFN. We develop the design of this qubit in Chapter 3 with ANSYS simulations, and we perform a DC current characterization in Chapter 4.

2.7.1 Josephson junctions fabricated at CNR-IFN.

The processes involved in the fabrication of a Josephson junction are various and depend on machinery and on specific construction parameters. In this section explain the essential steps to fabricate at the CNR-IFN in Rome the JJ analyzed in this work. The optical image of the analyzed chip, as described in chapter 4, is shown in figure 2.22.

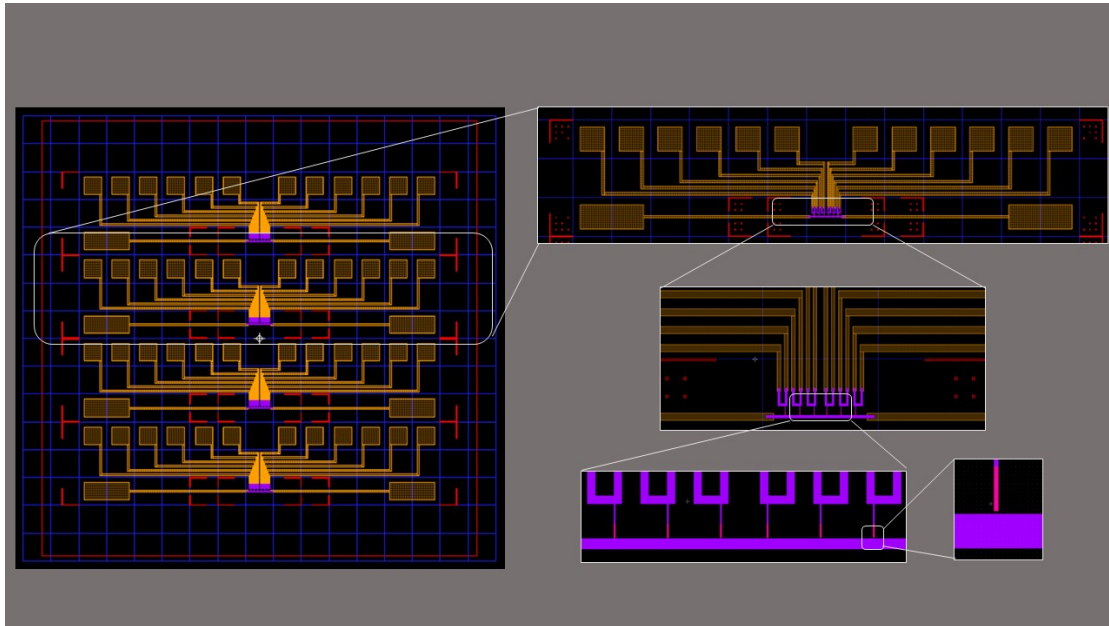


Figure 2.22: This is an optical image of the chip. There are various zooms of the image up to the last figure which represents the JJ. A real image of the chip is presented in Chapter 4.

On the right of figure 2.22 there is a zoom of a single JJ. The junction has dimension of $2 \times 2 \mu\text{m}^2$, it is structured as two aluminum superconductor layer with an aluminum oxide as insulator in between. The key processes of the fabrication of a single JJ are outlined in figure 2.23 and include electron-beam lithographic etching (Step 1), development (Step 2), aluminum evaporation (Steps 3 and 5) with oxidation in between (Step 4), and lift off (Step 6).

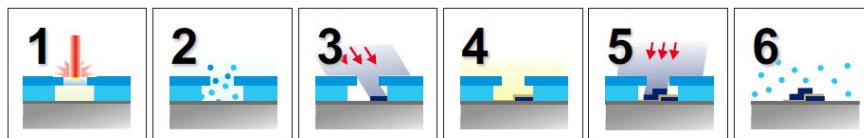


Figure 2.23: Fabrication steps of a Josephson junction.

The initial stage involves preparing the silicon chip substrate. It is done spinning two resist layers, which serve as the mask necessary for the later two-angle shadow evaporation. This process entails placing the wafer on a hot plate, where the two layers are spun one at a time. The mask is composed by two layers represented by the blue solids in figure 2.24, on the bottom the material is COP 33 10% AR-P 617.10 of 1031 nm thickness and on the top PMMA 6% AR-P 669.06 of 1720 nm thickness.

After that, the sequential processes depicted in Steps 1 to 6 of Figure 2.23 are carried out.

1. Initially, the design of the structure intended is designed by a software and the file loaded to the machine. Therefore, the electron beam lithography (EBL) is improved, in which the electron beam etches the bilayer allowing us to make the evaporation procedures.
2. The development is done in a mixture of two chemicals, isopropanol and methyl isobutyl ketone (MIBK) in this case, necessary to produce the undercut for the evaporation processes.
3. The evaporation is done with an electron gun evaporator. The evaporation and oxidation procedures specifically for our junctions are depicted in figure 2.24. The Al source is prepared and the evaporation chamber is pumped down. Then, the source is evaporated at an angle of 155° creating an aluminum layer of dimension 600 \AA .
4. The oxidation is performed immediately after the first evaporation, since the evaporation chamber remains in vacuum. Oxygen is injected at a pressure of 1 mbar for 5 minutes and then evacuated. Note that these are the parameters defining the thickness of the junction barrier and its capacity.
5. The chip is subsequently rotated to assume an angle of 90° and the second Al layer is deposited with the same evaporation process as step 3, the thickness of this second layer is 300 \AA .
6. The lift off consist of removing the resist from the wafer, leaving only the junction. This is done with warm acetone that dissolve the resist.

At the end of this procedures, the chip is rinsed into isopropanol and dried with a nitrogen gun.

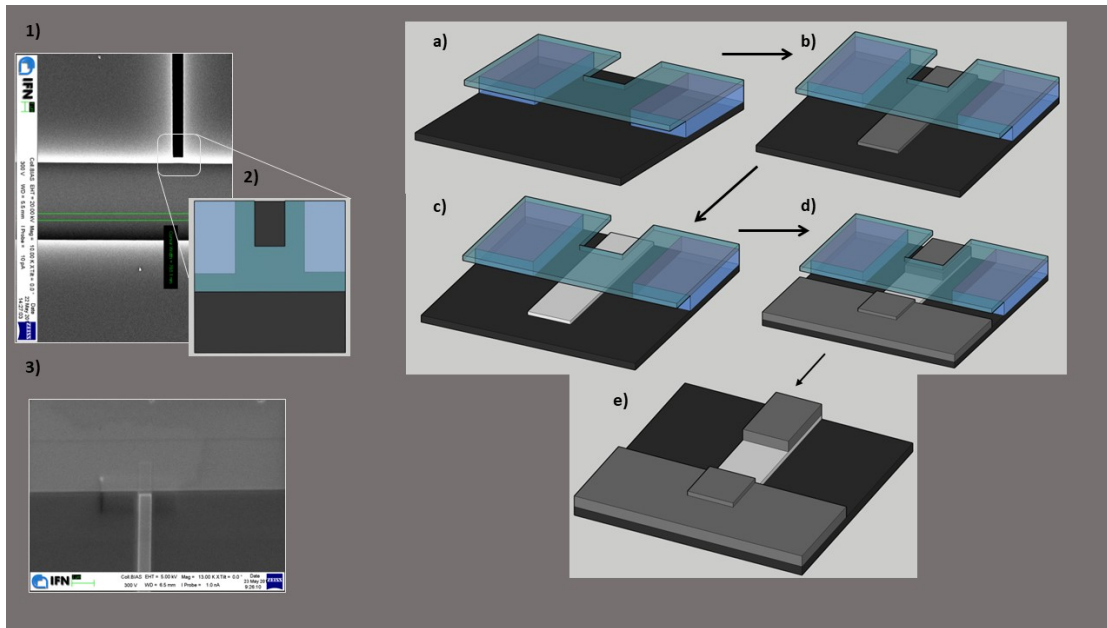


Figure 2.24: The figure represents on the left the real image of a JJ before 1) and after 3) the lift-off. Figure 2) is a schematic representation of the junction with the bilayer mask, defined by the blue boxes. The images on the right are the different steps of the fabrication: a) the holder with the masks, b) the first evaporation at 155° that forms the first aluminum layer, c) the oxidation, d) the evaporation at 90° for the second aluminum layer and e) after the lift-off where the mask is removed.

2.7.2 Transmon qubit fabricated at TII in Abu-Dhabi

The fabrication of the transmon qubit was made at the Technology Innovation Institute in Abu Dhabi. An optical image of the device is shown in figure 2.25(right). The fabrication process involves several steps:

1. Wafer Cutting: The qubit is made from a specific type of silicon with high resistivity ($> 20\text{k}\Omega\cdot\text{cm}$). The silicon wafer was cut into small square pieces, each measuring $22 \times 22 \text{ mm}^2$. Half-cuts were made on the backside of each piece, measuring $2 \times 14 \text{ mm}^2$.
2. Cleaning: The individual pieces were cleaned in a solution of Acetone and IPA using sonication for 5 minutes to remove any contaminants.
3. Layer Application: Two layers of resist were applied onto the silicon pieces using a spin coater. The bottom layer, 500 nm thick, was made of Kayaku PMGI SF9, while the top layer, 200 nm thick, was made of Allresist GmbH AR-P 6200.9 (CSAR).

4. Pattern Writing: Specific patterns for the transmon qubit and shunting capacitors were written onto the resist layers using an electron beam lithography system (Raith eLINE Plus).
5. Development: After exposure, the resist was developed using specific chemicals, revealing the desired patterns on the silicon pieces.
6. Metal Deposition: Aluminum (Al) was deposited onto the patterned areas using e-beam evaporation. A layer of 35 nm Al was first deposited, followed by oxidation at 0.625 mbar pressure for 25 minutes, and then a second deposition of 55 nm Al.
7. Liftoff: Excess Al was removed using a bath of N-Methylpyrrolidone at 70°C, leaving behind only the aluminum patterns on the silicon pieces.

The fabricated qubits were tested for their room temperature resistance using specialized equipment. As a final inspection, an optical image of the transmon qubit within the resonator along with the fabricated device, was captured for documentation and analysis.

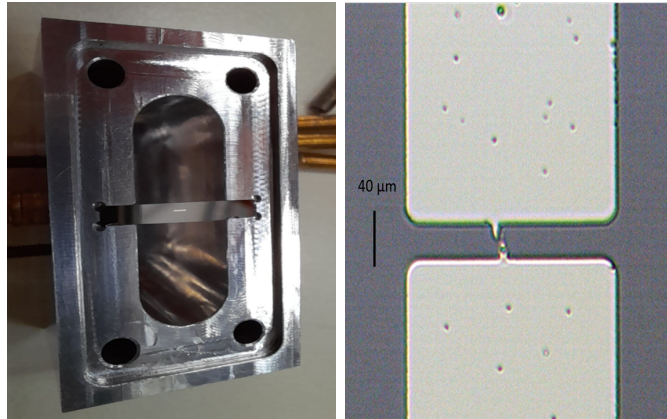


Figure 2.25: Left: Al cavity hosting the transmon chip. Right: optical image of the transmon shunt capacitance pads acquired with a 100x magnification. The JJ is not observable since is roughly $200 \times 200 \text{ nm}^2$, but it is located between the pads, in proximity of the two observable metal extensions.

The transmon qubit is placed in a resonant cavity for the full characterization. The resonant cavity is made of Al alloy 6061 with a rectangular parallelepiped shape of dimensions $L_x \times L_y \times L_z = 26 \times 36 \times 8 \text{ mm}^3$. An image of the cavity is shown in figure 2.25(Left). The silicon chip with the qubits is hosted in the middle of the $x - y$ plane with pads parallel to the z axis to couple to the mode TE_{110} . Two holes allow the insertion of the antennas for control and readout of the qubit state.

2.7.3 Transmon qubit fabricated at CNR-IFN

For the fabrication of the transmon qubit at CNR-IFN we implement the same technique used for the JJ. An image of the qubit is shown in figure 2.26, on the right there is the zoom of the JJ at the center, depicted by the blue rectangle.

The qubit has two pads of radius $500 \mu\text{m}$ and a distance between the junction and the circumference of the pad of $243 \mu\text{m}$, while the junction has dimension of approximately $150 \times 450 \text{ nm}^2$. The lower layer of the junction is of the left pad, it is composed by 600 \AA of aluminum, evaporated at angle 155° . The oxidation is performed injecting the oxygen for 5 minutes at 1 mbar pressure. The upper layer of the junction corresponds to the right pad and is formed by the evaporation of 600 \AA of aluminum at angle 155° . Also here the resist of the mask is removed with warm acetone.

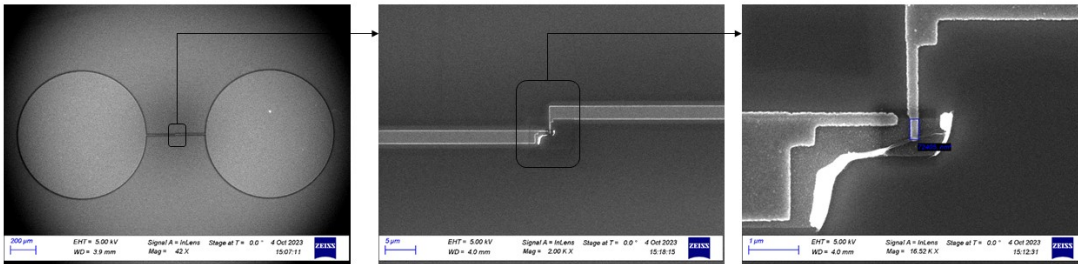


Figure 2.26: This is an image of circular qubit with different zooms, from the first figure with the entire qubit to the last with a zoom of the JJ, the blue rectangle in the last figure define where is located the JJ.

Chapter 3

Design qubit 3D

In this chapter, we conduct electromagnetic field simulations for various transmon qubit designs coupled with a 3D resonant cavity using ANSYS simulation software. We develop a method that provides a comprehensive description of the system, extracting key parameters directly from the simulations. This method is used in this section to improve the design of 3D transmon qubits, in particular the lifetime T_1 and in the next section to analyze the data from an experimental characterization of a real qubit.

3.1 Simulation Design

The simulation design comprises the 3D resonator cavity and the qubit laid on a silicon substrate. The qubit consists of the conductive pads and the Josephson junction. In ANSYS software, the components are defined as follows (Figure 3.1):

- The pads are represented by two 2D structures¹ with different shapes, with the boundary condition set as ‘Perfect E’ (perfect metal). The dimensions and shapes of the pads depend on the model considered.
- The substrate is in the center of the cavity, and the qubit is laid on it. The material is silicon (with dielectric constant $\epsilon_r = 11.9$), and the dimensions are $13 \times 2 \times 0.35 \text{ mm}^3$.
- The Josephson junction is set in the middle of the two pads in a 2D configuration. It is modeled as a Lumped LC, with the inductance (L) set around 5 to 10 nH and an intrinsic JJ capacitance (C) of 0.8 fF. We use a linear approximation for the inductance of the JJ.
- The 3D cavity, where all the components are placed. The cavity material is aluminum, and its dimensions are $36 \times 26 \times 8 \text{ mm}^3$ with rounded edges.

¹In general, we also consider 3D structures in our analysis, noting only small differences in the parameter extraction. For this reason, all the following geometries present 2D dimensions.

- On the upper part, two antennas are placed to couple the cavity with the external signals. We can set the position of the antennas to define different coupling powers. In the following simulations, there is no coupling with external signals.

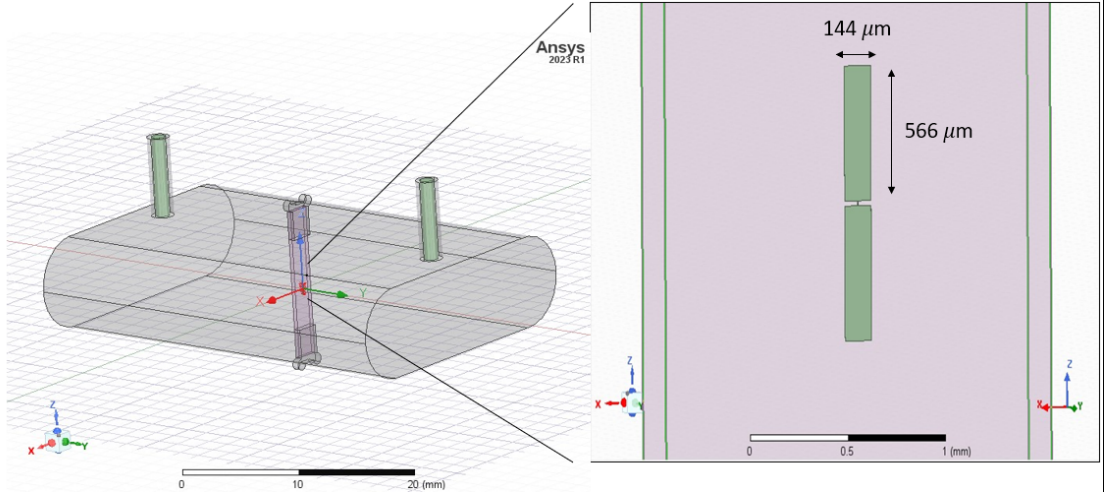


Figure 3.1: This is the simulation design of the resonant cavity with the Abu-Dhabi qubit.

3.2 Qubit Simulation in Resonant Cavity

In this section, we implement the method to estimate the principal parameters from electromagnetic simulations for the TII qubit fabricated at Abu Dhabi.

The geometry of the pads is a 2D rectangle with sides $a_p = 144 \mu\text{m}$ and $b_p = 566 \mu\text{m}$, and the distance between a single pad and the center of the junction is $d = 10 \mu\text{m}$. The inductance of the junction is set to $L = 10 \text{ nH}$. This value was determined during the fabrication process and is defined by the thickness of the oxide layer between the conductive pads of the junction. An experimental estimation of L is given in the next chapter. Figure 3.2 shows a simulation of the EM fields in the cavity and close to the qubit on the right. The qubit is coupled with the first mode of the cavity TE_{110} , as described in section 2.4.

In the following we discuss how to estimate the fundamental parameters of the qubit, listed in Table 3.1. The parameters are the total capacitance of the qubit C , the coupling constant g_{01} , and the qubit lifetime T_1 . Some calculations are done directly inside the ANSYS environment, using the ANSYS Calculator [20]. An example is shown in Figure 3.3.

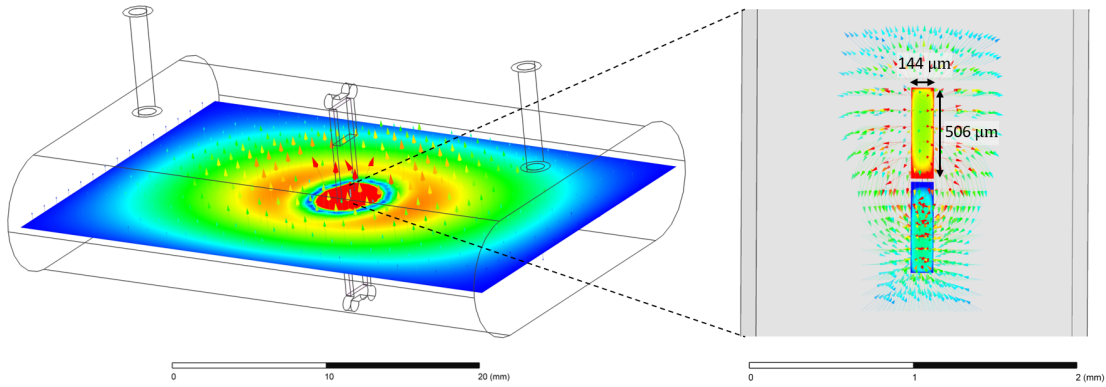


Figure 3.2: Simulation of the electromagnetic field in the TE_{110} mode with the Abu Dhabi qubit.

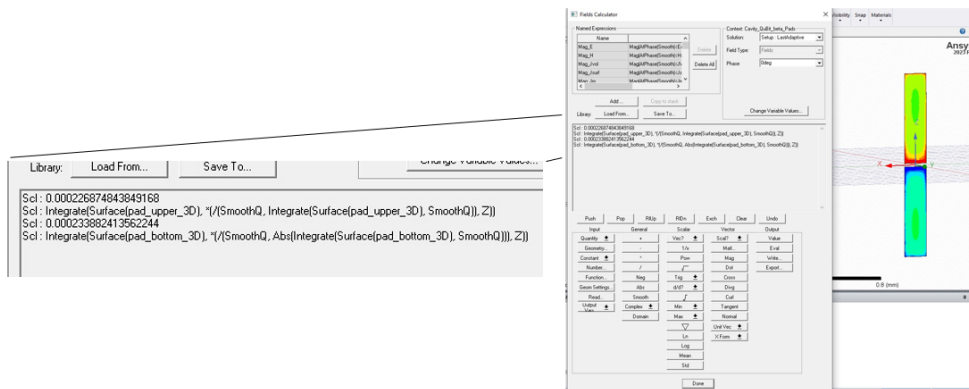


Figure 3.3: Screenshot of the ANSYS Calculator tool with the implemented effective distance formula.

Total Capacitance

In section 2.4.1, we explain how to derive the total capacitance of the qubit from the Maxwell capacitance matrix, defined in Equation 2.71:

$$C^M = \begin{pmatrix} C_{11} & C_{12} \\ C_{21} & C_{22} \end{pmatrix}$$

with the matrix components reported in Equation 2.72 and described in Figure 2.16. The total capacitance value is given by the Equation 2.80:

$$C = \frac{C_{11}C_{22} - C_{12}C_{21}}{C_{11} + C_{12} + C_{21} + C_{22}}$$

The matrix is derived from ANSYS-Q3D software and the total capacitance is

estimated by implementing the formula 2.80 within the ANSYS calculator. We find the value of the capacitance $C^{sim} = 56$ fF.

Coupling Constant

In section 2.4.2, we discussed how to relate the coupling g_{01} to the qubit geometrical proprieties. This is given by Equation 2.85:

$$g_{01} = \frac{2e \cdot d_{\text{eff}} \cdot E_0}{\hbar} \frac{1}{\sqrt{2}} \left(\frac{E_{J0}}{8E_C} \right)^{\frac{1}{4}}$$

where d_{eff} represents the effective distance, E_0 denotes the field amplitude of the cavity mode, E_J stands for the Josephson energy, and E_C refers to the charging energy of the qubit.

The value E_0 , as defined in Equation 2.58, is dependent on the cavity mode frequency ν_c and the mode volume V_{mode} . The cavity mode frequency $\nu_c = \omega_c/2\pi = 7.27$ GHz is estimated from ANSYS-HFSS simulations. The mode volume refers to the spatial region where the cavity mode is confined, in which most of the energy associated is concentrated. It is given by Equation 2.59:

$$V_{\text{mode}} = \frac{\int_V \varepsilon_0(\vec{r}) |E(\vec{r})|^2 d\vec{r}}{\max(|E(\vec{r})|^2)}$$

This formula is implemented on the ANSYS Calculator, integrating the electric field calculated by ANSYS-HFSS software. The value estimated is $V_{\text{mode}} = 1.6 \cdot 10^{-6}$ m³. The field amplitude E_0 is calculated as:

$$E_0 = \sqrt{\frac{\hbar\omega_c}{2\varepsilon_0 V_{\text{mode}}}} = 4.12 \cdot 10^{-4} \text{ V/m.}$$

The value of E_{J0} depends on the critical current $I_0 = \frac{\Phi_0}{2\pi L} = 33$ nA and is given by Equation 2.7:

$$\frac{E_{J0}}{\hbar} = \frac{\Phi_0 I_0}{2\pi\hbar} = 163 \text{ GHz.}$$

Similarly, E_C depends on the total capacitance, which was calculated earlier, and is given by Equation 2.20:

$$\frac{E_C}{\hbar} = \frac{e^2}{2Ch} = 0.35 \text{ GHz.}$$

The effective distance d_{eff} is the geometric distance between the center of the two pads, weighted by the distribution of charges. It is given by equation 2.82:

$$d_{\text{eff}} = \int_{A_{\text{up}}} \left(\frac{\rho_{\text{up}}(\vec{r})}{|q|} \right) \cdot z d\vec{r} + \int_{A_{\text{down}}} \left(\frac{\rho_{\text{down}}(\vec{r})}{|q|} \right) \cdot z d\vec{r}$$

with q the charge of a single pad, $\rho(\vec{r}) = \rho_{\text{up}}(\vec{r}) + \rho_{\text{down}}(\vec{r})$ the charge density and A_{up} and A_{down} the areas of the upper and lower pads. The value is estimated integrating the charges distribution calculated by ANSYS-HFSS software. This operation is done directly inside the ANSYS Calculator, obtaining $d_{\text{eff}} = 440 \mu\text{m}$.

Considering these results, we find the value of the coupling $g_{01}^{\text{sim}}/2\pi = 97 \text{ MHz}$.

Lifetime of the Qubit

In section 2.5.3, we define the relaxation time of the qubit T_1 from two contributions: the losses of the electromagnetic field in the dielectric media around the qubit (T_{int}) and via coupling to the cavity (T_{purcell}). The relaxation time is calculated by Equation 2.97:

$$T_1^{-1} = T_{\text{int}}^{-1} + T_{\text{purcell}}^{-1}$$

The Purcell time T_{purcell} is given by Equation 2.98:

$$T_{\text{purcell}} = \frac{\Delta^2}{g_{01}^2 \kappa}$$

with $\Delta = \omega_c - \omega_q$ the difference between the cavity and qubit resonance frequency. The qubit frequency is obtained inverting the Equation 2.34:

$$\frac{\omega_q}{2\pi} = \frac{\sqrt{8E_C E_{J0}} - E_C}{2\pi\hbar} = 6.38 \text{ GHz},$$

Considering the cavity frequency just calculated, we estimate $\Delta = \omega_c - \omega_q = 5.6 \text{ GHz}$. The decay rate of the cavity is $\kappa = \omega_c/2Q_{\text{cav}} = 0.54 \text{ MHz}$, in which the quality factor of the cavity $Q_{\text{cav}} = 42055$ is given from the experimental analysis in Chapter 4. From these results, we obtain the Purcell time $T_{\text{purcell}} = 156 \mu\text{s}$.

The intrinsic lifetime T_{int} is defined in terms of an intrinsic quality factor, as described in Equation 2.100: $Q_{\text{int}} = \omega_q T_1^{\text{int}}$. The value of Q_{int} depends on the participation ratios from different spatial regions. This is given by Equation 2.100:

$$Q_{\text{int}}^{-1} = \sum_i P_i \tan \delta_i.$$

with the participation ratios defined by the formulas reported below. Equation 2.102 for the surface between the pads and the silicon substrate (MS), Equation 2.103 for the pad surface in air (MA), and Equation 2.104 for the part of the substrate in contact with air (SA):

$$\begin{aligned} P_{\text{MS}} &= \frac{\epsilon_0 \epsilon_S^2}{\epsilon_{\text{MS}}} t_{\text{MS}} \frac{C_{\text{tot}}}{q^2} \int_{\text{MS}} d\vec{r} |E_{0\perp}|^2 \\ P_{\text{MA}} &= \frac{\epsilon_0}{\epsilon_{\text{MA}}} t_{\text{MA}} \frac{C_{\text{tot}}}{q^2} \int_{\text{MA}} d\vec{r} |E_{0\perp}|^2 \\ P_{\text{SA}} &= \epsilon_0 t_{\text{SA}} \frac{C_{\text{tot}}}{q^2} (\epsilon_{\text{SA}} \int_{\text{SA}} d\vec{r} |E_{0\parallel}|^2 + \epsilon_{\text{SA}}^{-1} \int_{\text{SA}} d\vec{r} |E_{0\perp}|^2) \end{aligned}$$

with E_0 is the electric field in air and q the charge of the pad. For MS and MA, only the perpendicular contribution is considered, and for SA, only the parallel one. A representation of the three spatial regions of the qubit is shown in Figure 3.4.

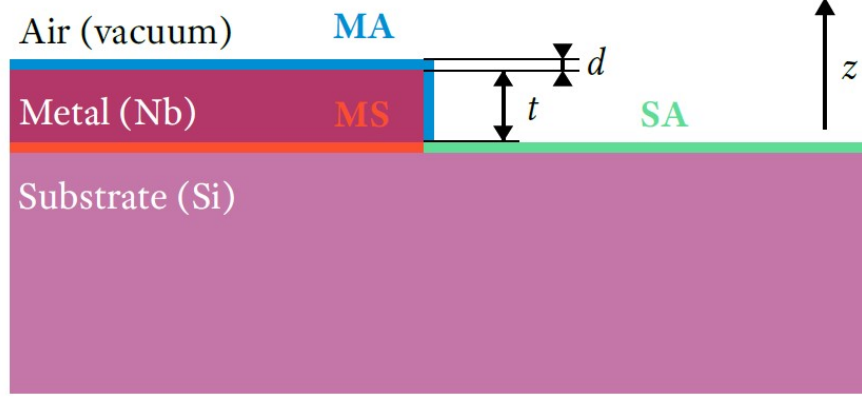


Figure 3.4: Representation of the spatial regions in the participation ratios calculation. The metal surface represents qubit pad that for the TII qubit is made of Aluminum. The regions considered are metal-air (MA), metal-substrate (MS), and substrate-air (SA).

We determinate the participation ratio values by integrating the electric field calculated by HFSS-ANSYS software using the ANSYS Calculator. The constant values set for the calculations are as follows. Aluminum oxide: $\epsilon_{MS} = \epsilon_{MA} = 9.8$, Silicon dioxide: $\epsilon_{SA} = 3.8$, Silicon substrate: $\epsilon_S = 11.8$ Loss tangent: $\delta_i = \delta = 0.002$, Thickness: $t_i = 5$ nm. The value of the ϵ_i are typical and taken from [18], the loss tangent is taken from [17] and the value of the thickness is an approximation.

We estimate the total loss as $P_{tot} = P_{MS} + P_{SA} + P_{MA} = 2.18 \times 10^{-4}$, with the major contribution from P_{MS} , which is hundreds of times higher than the other two contributions. Considering a constant δ , the value of the intrinsic quality factor directly depends on P_{tot} :

$$Q_{int} = \left(\sum_i P_i \tan \delta_i \right)^{-1} = (P_{tot} \tan \delta)^{-1} = 2.29 \cdot 10^6,$$

Thus the intrinsic lifetime is:

$$T_{int} = \frac{Q_{int}}{\omega_q} = 57 \mu s.$$

From these results, we estimate the qubit lifetime as:

$$T_1 = \left(\frac{1}{T_{int}} + \frac{1}{T_{purcell}} \right)^{-1} = 42 \mu s.$$

Table 3.1: Simulated parameters for the Abu-Dhabi qubit coupled with the cavity.

Variables	Values
I_0 [nA] / L_0 [nH]	33 / 10
a_p [μm]	144
b_p [μm]	556
d [μm]	10
P_{tot}	$2.18 \cdot 10^{-4}$
$T_{purcell}$ [μs]	156
T_{int} [μs]	57
T_1 [μs]	42
C_{tot} [fF]	56
d_{eff} [μm]	440
$g_{01}/2\pi$ [MHz]	97

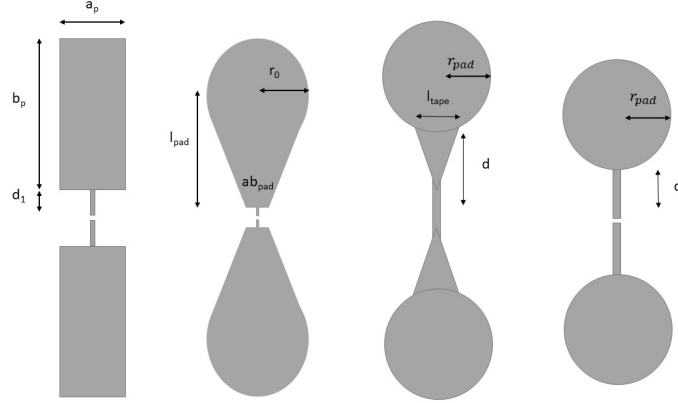
3.3 Loss qubit optimization and circular design

In this section, we apply the method developed in the last section to evaluate various transmon designs. The aim is to improve the geometrical parameters values in order to reduce the total losses on the qubit and increase its lifetime T_1 .

3.3.1 Pad Geometries

In our optimization process we consider different pads geometries. These are obtained by modifying the size and shape of the two pads. Each pad geometry has a component that connects the pad to the Josephson junction, which can be a straight or inclined line. Four geometries of the qubit pads are taken into account (see Figure 3.5), each described with different parameters:

- **Rectangular Geometry:** This geometry consists of two rectangular pads. The principal parameters are a_b and b_p , the dimensions of the rectangle, and d , the distance between the pad and the center of the JJ.
- **Pear Geometry:** The second geometry is defined by two pads of composed by a circle linked by a trapezoid. The geometrical parameters are the radius of the circle r_0 , the distance between the center of the JJ and the trapezoid small base l_{pad} , and the length of the small base ab_{pad} .
- **Circular Tapered Geometry:** In the third geometry, the pad is composed of a circle joined to the JJ by a tapered structure. The geometrical parameters are the radius of the circle r_{pad} , the distance between the center of the JJ and the nearest part of the circle d , and a variable that denotes the level of tapering l_{tape} .



4 4

Figure 3.5: The considered pad geometries: rectangular pad (first), pear pad (second), circular tapered pad (third), and circular pad (fourth).

- **Circular Geometry:** The fourth geometry is the same as the third one but without tapering, i.e., with only rectangular structures connecting the pads with the JJ. Therefore, the only two parameters are r_{pad} and d .

3.3.2 Designs analysis

The starting point of our T_1 optimization analysis is the geometry of the transmon qubit produced in Abu Dhabi, with the parameters reported in Table 3.1. The value of the total loss $P_{tot} = 2.18 \cdot 10^{-4}$ is taken as the reference P_0 . As we already see, the lifetime of a qubit depends on T_{int} , due to the losses of the EM field around the qubit, and $T_{purcell}$, due to the losses via the coupling to the cavity, as described by Equation 2.97:

$$T_1^{-1} = T_{int}^{-1} + T_{purcell}^{-1}$$

In particular we have:

- The value of $T_{purcell} = \frac{\Delta^2}{g_{01}^2 \kappa}$ (Equation 2.98) depends on $\kappa = \omega_c/2Q_{cav} = 0.54$ MHz, fixed by the cavity features as calculated in the last section, and on the ratio $|\Delta/g_{01}|$. The latter depends on the qubit frequency ω_q (since $\Delta = \omega_c - \omega_q$) and on the coupling strength of the qubit. The coupling strength is given by Equation 2.85 and depends mostly on the effective distance variation d_{eff} (since E_0 is fixed by the cavity parameters and $(\frac{E_{J0}}{8E_C})^{\frac{1}{4}}$ is almost constant). For the qubit produced in Abu Dhabi, the value of the ratio is $|\Delta/g_{01}| = 6.8$.
- The value of $T_{int} = Q_{int}/\omega_q$ (Equation 2.99) depends on the qubit frequency and on the intrinsic quality factor, given by the sum of the participation

ratios P_{tot} for the different spatial regions (Equation 2.101): metal-air (MA), metal-substrate (MS) and substrate-air (SA).

For the qubit produced in Abu Dhabi, the value of the $T_{purcell} = 156 \mu s$, is higher than the $T_{int} = 57 \mu s$, therefore T_{int} gives the higher contribution for the qubit decoherence, that brings lower T_1 . In this section, we focus on improving the value of the T_{int} , with keeping the ratio $|\Delta/g_{01}|$ almost constant, in order to not invalidate the $T_{purcell}$.

To achieve this, we modify the designs by conducting an iterative study of the geometrical parameters of the qubit pads, using the ‘Optimetrics’ tool in ANSYS. For every configuration, we estimate the capacitance C , the effective distance d_{eff} and the total loss P_{tot} from ANSYS software in order to evaluate the losses and calculate the ratio $|\Delta/g_{01}|$, as described in the last section for the qubit of Abu Dhabi.

The formula of the losses contribution, given by Equation 2.101:

$$P_i = \frac{\epsilon_0 \epsilon_i \tau_i C}{q^2} \int_{A_i} d\vec{r} |E(\vec{r})|^2$$

depends on the total capacitor energy $W = \frac{q^2}{2C}$, with q the charge of a single pad, but also on the distribution of the electric field E_0 on the different contribution surfaces A_i . Higher electric fields distributed in small areas lead to an increase in total electromagnetic losses.

Analyzing the distribution of the electromagnetic field of the design of the Abu Dhabi qubit (Figure 3.6(left)), we notice that a significant portion of the field concentrates on the corners of the rectangular pads, increasing the losses. To avoid this, we perform two different operations:

1. A smoothing of the pad corners.
2. An addition of tapered lines, i.e., tilted lines that connect the pads to the junction.

with the aim of achieving a better distribution of the field.

Before trying new pads geometries we make an evaluation of the variations in losses by modifying the geometrical parameters of the rectangular design. The ranges are $a_p = (50, 800) \mu m$, $b_p = (200, 1400) \mu m$, and $d = (4, 20) \mu m$. As we expected the capacity increases with the pad dimensions and decreases with increasing distance d . The effective distance is directly proportional to a_p , b_p , and d . In general the losses values remains high, comparable to P_0 . The same thing applies for the pear geometry: the capacitance increase with the pads areas and decrease moving the pads further from the junction. The losses are still high due to the fields that stands on the corners of the trapezoid base ab_{pad} .

The losses decrease significantly trying the new design with circle pads and tapered lines, where a complete analysis is presented in Figure 3.7. This figure

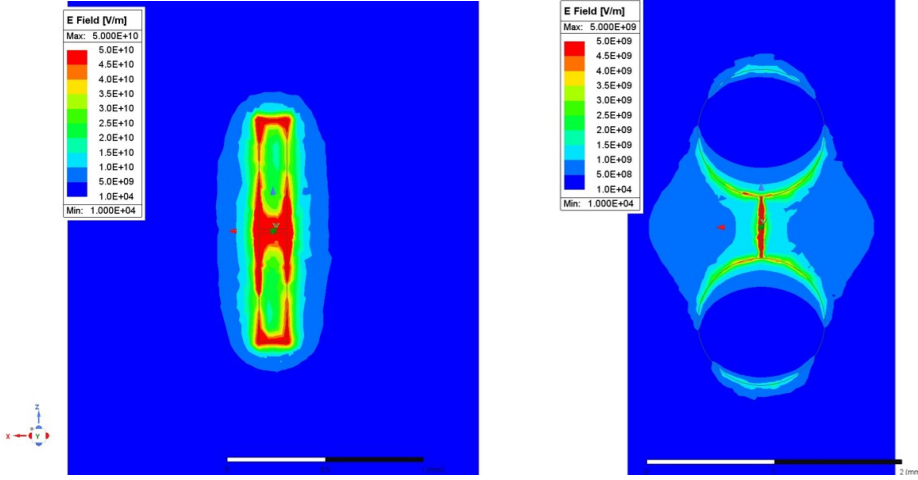


Figure 3.6: Comparison of electromagnetic field simulations on the surfaces of the two qubits, the Abu-Dhabi (left) and circular (right). We observe a higher EM field distribution on the corners. The scale to value of the EM field for the circular pads is an order of magnitude smaller than the Abu Dhabi one.

shows the variation of the capacity, effective distance, and losses as functions of the three geometrical parameters. In general, we tried various values in different ranges. In Figure 3.7 the parameters variation ranges are $r_{pad} = [350, 650] \mu\text{m}$, $l_{tape} = [0, 200] \mu\text{m}$, and $d = [150, 350] \mu\text{m}$.

From this analysis we made the following considerations:

1. The capacity is directly dependent on r_{pad} , l_{tape} , and inversely on d . Increasing the pads areas the capacitance get higher and increasing the distance between the pads becomes smaller.
2. The effective distance is directly dependent on l_{tape} and d , and inversely on r_{pad} . As a consequence, the value of the coupling strength is lower increasing the area, while is higher increasing the distance between the pads and the level of inclination of the lines.
3. The losses are strongly dependent on the radius of the pads: higher radius values correspond to larger areas and less losses. The distance between the pads also influences the losses, although in a limited way; generally, there are smaller losses for closer pads. The losses are only weakly influenced by the tapering; we find that the geometry that minimizes the losses is without tapering.

Considering the minimal influence of tapering on the losses, we conduct a finer variation the parameters for the geometry with straight lines, since this geometry has only two parameters and requires less computational time. In Figure 3.8

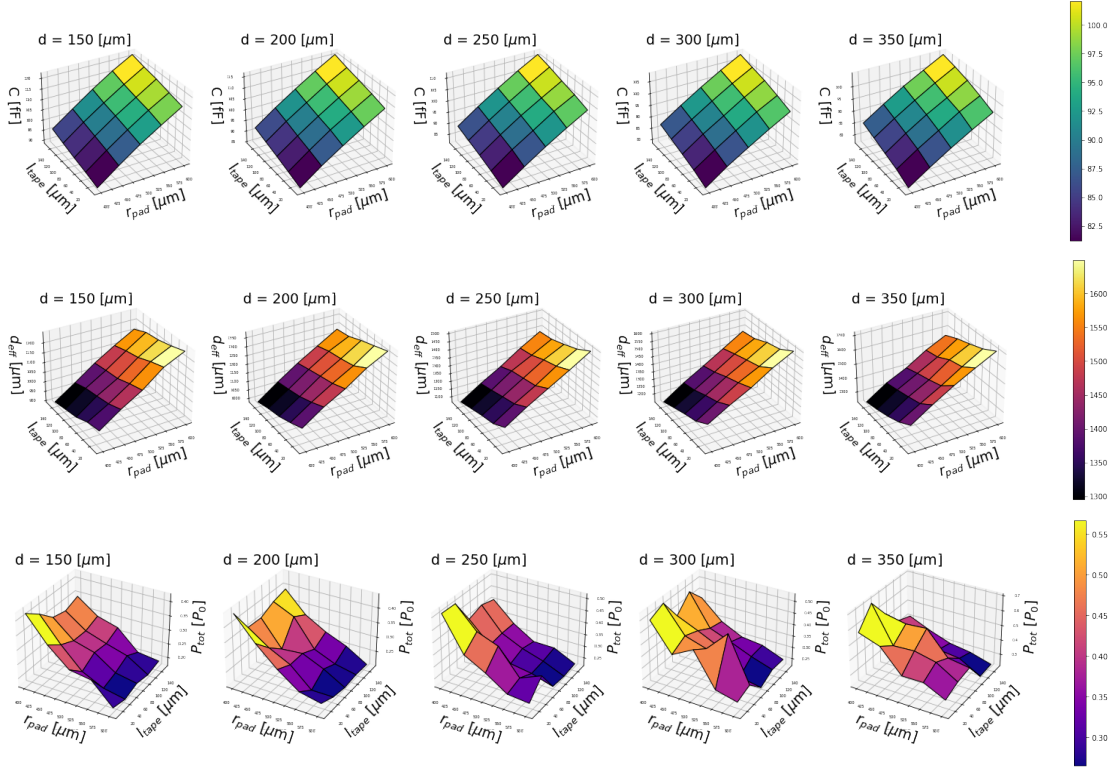


Figure 3.7: Complete analysis of the circular tapered geometry, including variations in the total capacity (upper), effective distance (middle), and losses (lower) as a function of the geometrical parameters. The ranges of the geometrical parameters are $r_{pad} = [350, 650] \mu\text{m}$, $l_{tape} = [0, 200] \mu\text{m}$, and $d = [150, 350] \mu\text{m}$. Note that for the effective distance, the axes are reversed for image display purposes. The variations in results are discussed in the text.

we show the results for the following variation ranges: $r_{pad} = [200, 700] \mu\text{m}$ and $d = [10, 500] \mu\text{m}$. For the capacity and effective distance, we observe the same dependence on the radius r_{pad} and the distance d as in the circular tapered design. The losses are strongly dependent on the radius and weakly on the distance from the pads to the junction.

The previous analyses are performed by fixing the inductance value $L = 10$ nH, as specified by the qubit of Abu Dhabi. But in general, we have the flexibility to set the fabrication parameters of the junction to have a precise inductance. A variation in L corresponds to a change in the qubit frequency. In this analysis, we vary L to observe its influence on the total loss P_{tot} . After, we select the value of L while maintaining the factor $|\Delta/g_{01}|$ constant, even though the chosen value may not be optimal. In Figure 3.9, we show the variation of the losses as a function of the inductance. The latter modifies the value of the losses by almost 20%.

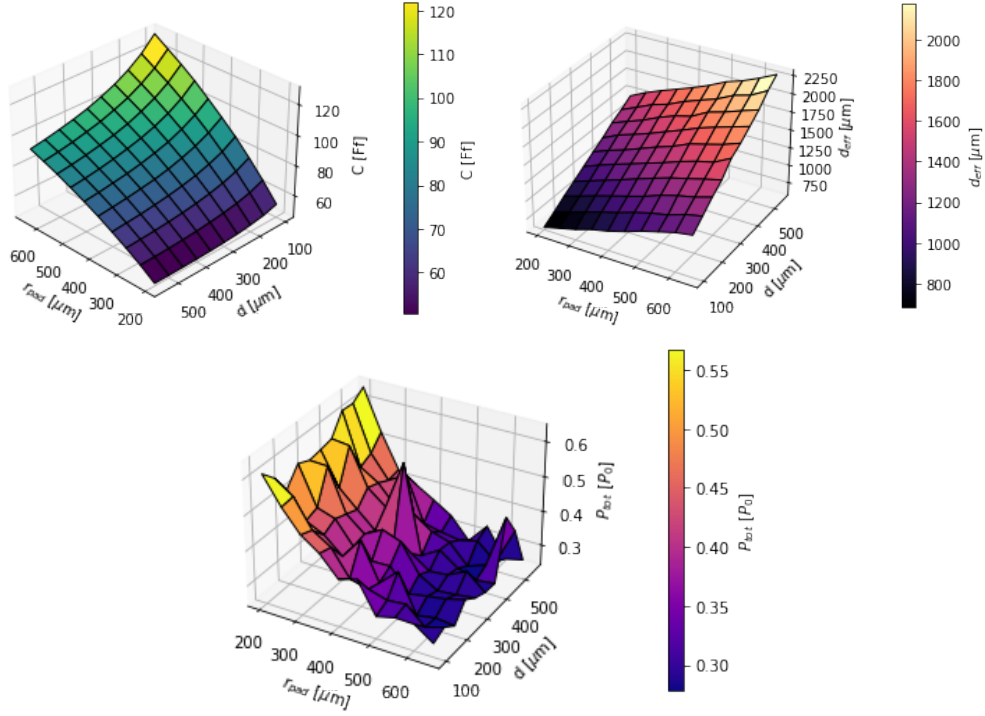
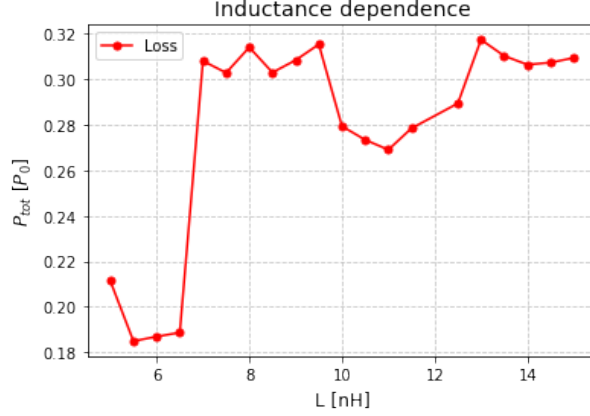


Figure 3.8: Analysis of the circular qubit. The variation of the capacity (first), effective distance (second) and the losses (third) as a function of the radius r_{pad} and the distance of the pad circumference from the center of the junction d .

3.3.3 Circular design

Taking into account all the results, we obtain the optimal design defined by circular pads geometry with a radius of $500 \mu\text{m}$ and a distance between the center of the circle and the junction of $243 \mu\text{m}$, the inductance is set at $L = 7.8 \text{ nH}$ that corresponds to a critical current of $I_0 = 42 \text{ nA}$. The design is selected to minimize losses by maximizing the pad radius while keeping the ratio $|\Delta/g_{01}|$ constant, which is influenced by the effective distance. The most important features of this qubit are reported in Table 3.2, which are compared to the ones of the qubit produced in Abu Dhabi in Table 3.1.

With this qubit design we reduce the total losses of $P_{tot} = 0.31 \cdot P_0$, with an increase of the internal time of $T_{int} = 244 \mu\text{s}$. The value of the ratio is $|\Delta/g_{01}| = 9$ (instead of $|\Delta/g_{01}| = 6.8$), giving a estimation of $T_{purcell} = 84 \mu\text{s}$ lower than the initial design ($T_{purcell}^{(Abu-Dhabi)} = 156 \mu\text{s}$). Considering both the contributions, the lifetime obtained by the simulation is $T_1 = 63 \mu\text{s}$, that is higher than the initial one of $T_1^{(Abu-Dhabi)} = 42 \mu\text{s}$. In Figure 3.6 we see the electric field distribution for the circular design (right) compared to the design of the qubit produced in Abu

Figure 3.9: Losses for different value of the inductance L .

Dhabi (left). As expected, by smoothing the corners, we achieve a more uniform field distribution on the pads with a lower intensity, resulting in a reduction of losses. This design presents also a bigger capacitance $C = 93$ fF and a higher value of the coupling constant $g_{01}/2\pi = 355$ MHz.

Table 3.2: Simulated parameters for the new circular qubit coupled with the cavity.

Variables	Values
I_0 [nA] / L_0 [nH]	42 / 7.8
r_{pad} [μm]	500
d [μm]	243
P_{tot}	$6.51 \cdot 10^{-5}$ ($0.31P_0$)
$T_{purcell}$ [μs]	84
T_{int} [μs]	244
T_1 [μs]	63
C_{tot} [fF]	93
d_{eff} [μm]	1337
$g_{01}/2\pi$ [MHz]	355

3.3.4 Mesh resolution

It is possible to improve the results with a major computational power that allows a finer scan of the parameters and a better resolution of the Mesh. The Mesh is a discretized representation of the geometry that breaks it into small elements to facilitate accurate numerical simulation by solving equations at discrete points. Setting the appropriate mesh is crucial for accurately simulating physical behavior, which plays an important role in our analysis, particularly for calculating the losses that influence the qubit lifetime T_1 (section section 2.5.3).

In these simulations, we used a mesh size on the order of $50 \mu\text{m}$, as shown in Figure 3.10. The variation of the effective distance and the loss as a function of the mesh size for the qubit of Abu Dhabi is shown in Figure 3.11.

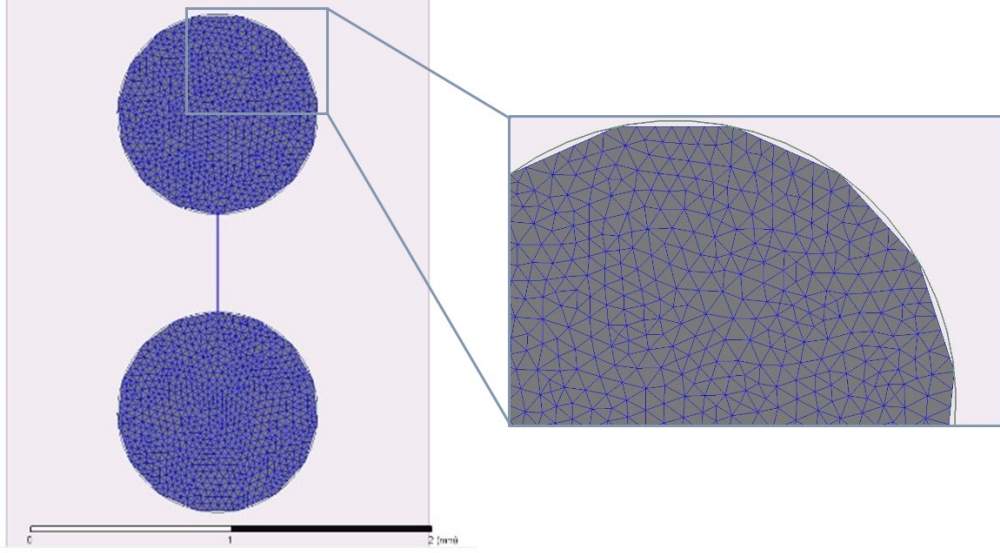


Figure 3.10: Circular qubit design with a mesh size set at $50 \mu\text{m}$.

A mean of the effective distance values obtained from these simulations is $d_{\text{eff}} = 441 \pm 16 \mu\text{m}$, which is influenced only by 3% modifying the mesh size. However, the total losses $P_{\text{tot}} = (2.66 \pm 0.95) \cdot 10^{-4}$ changes significantly with the mesh size (35%). This fluctuation affects the T_{int} value and consequently impacts the qubit lifetime T_1 .

Comparing the simulation results with the experimental results presented in the next chapter in Table 4.1, we notice that while the simulated values of capacitance and coupling constant align well to the experimental results, the value for the simulated lifetime value of $T_1^{\text{sim}} = 42 \mu\text{s}$ differs substantially from the experimentally determined one of $T_1^{\text{exp}} = 8.68 \mu\text{s}$. The different values of the lifetime might originate from an underestimation of the participation ratios due to limitations in our numerical mesh resolution. The large range of scale from millimetres for the pads and nanometres for the edge regions, makes it computationally challenging to resolve the electric field accurately, especially in the edge regions where the fields diverge. This is also true for the losses estimation in the design optimization, where we cannot completely rely on the simulation for the calculation of the losses if we cannot get the meshing size further down. Previous reports on this have been given in [18] and [21], where also potential solutions are proposed, that are currently explored.

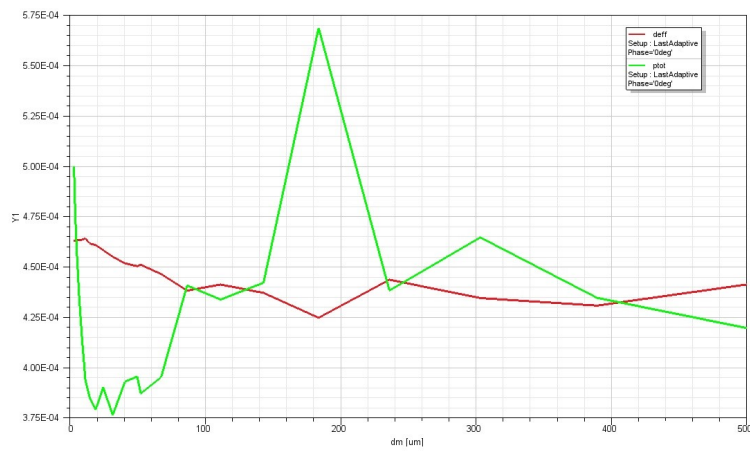


Figure 3.11: This is a plot of the effective distance (red) and the losses (green) as a functions of the mesh size dm simulated for the Abu Dhabi qubit. The Y1 is the value of the two quantities for different mesh sizes. The total losses P_{tot} is given by the value on the graph divided by the factor 0.56 that depends on the pad capacitance, since in ANSYS the loss calculation is made considering $C = 100$ fF. There are mesh values from $2.6 \mu\text{m}$ to $0.5 \mu\text{m}$, while for finer values the pc ran out of RAM memory.

Chapter 4

Measurement

In this chapter, we present the characterization of the TII qubit fabricated in Abu-Dhabi and of the qubit and Josephson junctions fabricated at CNR-IFN in Rome. All measurements are performed at the National Laboratory of INFN in Frascati (LNF).

4.1 Cryogenics

Qubits and Josephson junctions require a cryogenic environment to reach very low temperatures, enabling the transition of aluminum into the superconducting state and reducing noise and decoherence effects.

At LNF, we used a Leiden Cryogenics CF-CS110-1000 ^3He - ^4He dilution refrigerator, capable of achieving temperatures of approximately 10 mK and maintaining that temperature for relatively extended periods.

4.1.1 Dilution refrigerator operation

Dilution refrigerators use the properties of helium isotopes, specifically ^3He and ^4He . These isotopes exhibit distinct behaviors: ^4He acts as a Bose fluid and undergoes a phase transition into a superfluid state below 2.17 Kelvin, whereas ^3He behaves as a Fermi fluid with higher entropy.

When mixed together, ^3He can flow through the superfluid ^4He with little impedance. At low temperatures, the isotopes naturally separate, with ^3He floating on top of ^4He due to its lower density.

The separation process occurs spontaneously, with the ^3He -rich phase becoming purer as the temperature decreases, while the ^4He -rich phase reaches a specific concentration. This behavior is governed by the quantum nature of the fluids, ensuring that ^3He always dissolves in ^4He with a minimum concentration, which is crucial for the success of dilution refrigerators.

A dilution refrigerator typically consists of three main parts: the mixing chamber (MC), the still, and the heat exchangers. The mixing chamber is the coldest stage and contains pure ^3He on top of diluted ^4He . The still heats up and removes vapor ^3He , creating a concentration gradient in the mixing chamber.

To maintain equilibrium, pure ^3He moves downward into the diluted ^4He , resulting in a cooling effect. The vapor ^3He removed from the still is condensed and returned to the mixing chamber to complete the circulation cycle. The returned ^3He gas can be condensed using either wet or dry methods, depending on the presence of liquid ^4He in the cryostat.

4.1.2 Cryostat

The image of the LNF cryostat is depicted in figure 4.1 where the plates composing the device are shown. The cryostat is composed by five plates. Starting with the 50 K plate on the top of the cryostat, the temperature of the system gradually decreases up to the 10 mK plate to the bottom of the cryostat.

The refrigeration process starts with a precooling operation using liquid Nitrogen that bring the temperature from 300 K to 77 K. The liquid Nitrogen flows in the LN pipes, in thermal contact with each plate. Then, a pulse tube, which operates compression and decompression cycles to the ^4He gas, is switched on and brings the temperature down to about 4 K. Finally, circulation of the ^3He - ^4He mixture is activated and the system is cooled down to about 10 mK in the mixing chamber. The devices studied in this work are in thermal contact with the 10 mK plate of the refrigerator.

4.2 Transmon qubit characterization

The transmon qubit characterization consists in the extraction of important parameters from experiment analysis. The transmon qubit considered in this work is the one fabricated at the Technology Innovation Institute in Abu Dhabi. A complete description of the fabrication is made in section 2.7.2.

The parameters are extracted by the Hamiltonian derived in section 2.4. It describes the qubit-cavity system in a dispersive regime keeping into account the third energy level. The Hamiltonian is:

$$\hat{H} = \hbar(\omega'_c + \chi\sigma_z)b^\dagger b + \frac{\hbar}{2}\omega'_{01}\sigma^z \quad (4.1)$$

where ω'_c and ω'_{01} are the frequencies of the cavity and the qubit renormalized by the interaction terms.

$$\omega'_c = \omega_c - \frac{\chi_{12}}{2} \quad \text{and} \quad \omega'_{01} = \omega_{01} + \chi_{01} \quad (4.2)$$

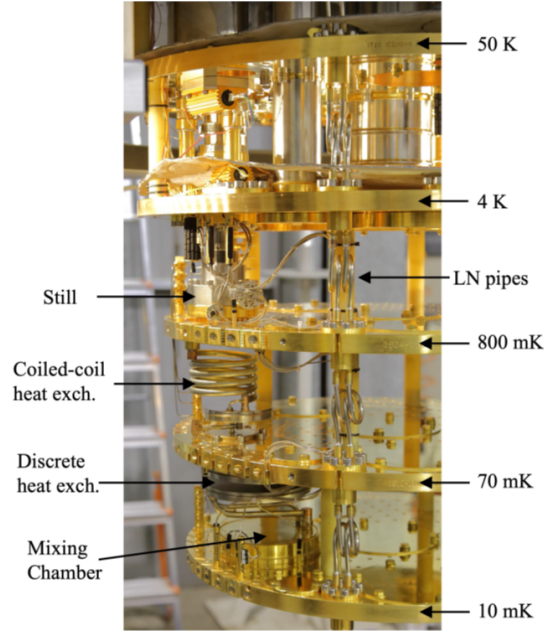


Figure 4.1: Detail of the Leiden Cryogenics CF-CS110-1000 dilution refrigerator, showing the plate temperatures of all the thermalization stages.

The term χ is the total dispersive shift and is defined as

$$\chi = \chi_{01} - \frac{\chi_{12}}{2} \quad (4.3)$$

with χ_{ij} given by

$$\chi_{ij} = \frac{g_{ij}^2}{\Delta_{ij}} \quad (4.4)$$

with $\Delta_{ij} = \omega_{ij} - \omega_c$. The terms g_{ij} and $\omega_{ij} = \omega_i - \omega_j$ are the coupling and the pulse frequency difference between two consecutive qubit levels i and j .

In this section we show some principal techniques for qubit characterization. The results of the analysis are listed in Table 4.1. The characterization procedure is divided in transmon spectroscopy and time domain characterization.

4.2.1 Experimental setup

Full characterization of the qubit was done at the National Laboratory of INFN in Frascati. The experimental setup is shown in Fig. 4.2.

The dashed lines indicate the different temperature stages of the cryostat of a dilution refrigerator. The device is host in the 10 mK stage. Control and readout signals entering Line 1 are attenuated by -20 dB at 4 K and by -30 dB at 10 mK. Including the attenuation of the coaxial cable the total attenuation is -68 dB.

Both input and output ports are filtered with IR and Low-pass filters with 10 GHz cut-off frequency, while an additional 4 GHz high-pass filter is mounted on the input port. The output signal passing through Line 5 is amplified with a High Electron Mobility Transistor by 36 dB at 4 K and with two Field effect transistor by 35 dB and 30 dB at 300 K. Two circulators are used to minimize the reflected noise and decouple the amplification stages.

For time-domain measurements, the qubit control pulses are directly produced by a RF source (ROHDE-SCHWARZ SMA100B). The readout pulse is obtained by the vector modulation of a signal generated by a second RF source (ROHDE-SCHWARZ SGS100A) at the cavity frequency and controlled by a square-wave pulse of width $10 \mu\text{s}$ generated by a wave function generator (KEYSIGHT 33500B) triggered by the SMA100B.

Both the control and readout pulses are transmitted to Line 1 through a combiner. After amplification, the readout pulse is down-converted and I and Q quadratures are acquired with a 16-bit ADC board at 1GS/s rate, and post-processed to determine the qubit state.

For cavity and qubit spectroscopy, the generation and acquisition of the readout pulse is replaced by the S21 measurement with Vector Network Analyzer (VNA).

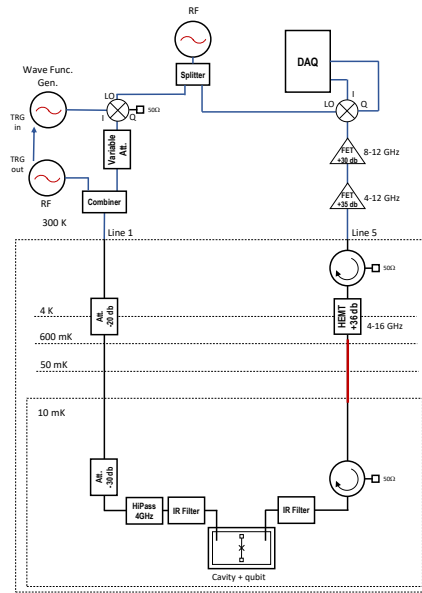


Figure 4.2: Scheme of the experimental setup used for the transmon characterization.

4.2.2 Transmon spectroscopy characterization

The first type of characterization is a spectroscopy. It is implemented analyzing the absorption spectra of the Vector Network Analyzer (VNA) and is divided in cavity and qubit spectroscopy [22].

Cavity spectroscopy

The cavity spectroscopy consists of an analysis of the absorption spectra S21 for different power of the probe. To explain the behavior of the system we rewrite the Hamiltonian from the resonator point of view:

$$H_c = \hbar(\omega_c - \frac{\chi_{12}}{2} + \chi\sigma_z)b^\dagger b + \frac{\hbar}{2}(\omega_{01} + \chi_{01})\sigma_z \quad (4.5)$$

In Figure 4.3(left) we show the resonator absorption as a function of the probing power. This is obtained taking the transmission spectra using the VNA, for different values of the VNA power.

From Figure 4.3(right) we see the transmission for the higher (orange) and the lower (blue) VNA power. In this characterization the qubit has no external excitation, so it remains in the $|0\rangle$ state with eigenvalue $-\frac{\hbar\omega_q}{2}$.

In Figure 4.3(left), the power of the VNA increases the number of photons $N = b^\dagger b$ inside the cavity. The rise of the power causes a shift of the frequency. In particular, we observe two different features on the figure:

- At low power the qubit is coupled to the cavity, this coupling cause a shift of the frequency of the system. Considering ω_c the bare cavity frequency, we have a shift from this frequency to the frequency of the dressed cavity-qubit system ω'_c . This shift is given by

$$\omega_c - \omega'_c = \chi + \frac{\chi_{12}}{2} \quad (4.6)$$

This is seen in equations 4.2 and in the Hamiltonian 4.5. In both equations there is a term depending on σ_z . We notice a shift of the transmission peak to lower frequencies increasing the power of the probe, due to a second order effect.

- For too high power, the number of photons is so high as to induce the transition of the junction to the normal state. In this case we observe only one resonance at the bare cavity frequency ω_c .

This two features are distinct in Figure 4.3(right), the peaks in the spectra correspond to the cavity system (orange) and the qubit-cavity (blue) system. From the spectra at lower power we find the value of the dressed cavity frequency $\nu'_r =$

$\omega'_r/2\pi = 7.279$ GHz. It is given by the center of the peak interpolated with a Lorentzian function.

From high power we see the peak corresponding to the cavity resonance. Interpolating the spectrum with a Lorentzian function we calculate the bare frequency of the cavity $\nu_c = \omega_c/2\pi = 7.269$ GHz and the loaded quality factor of the cavity $Q_{cav} = 42055$. It is given by $Q_{cav} = \frac{\omega_c}{\Delta\omega}$ with $\Delta\omega$ the full width half maximum. Then the shift of the cavity frequency is $(\chi + \frac{\chi_{12}}{2})/2\pi = -10.2 \pm 0.1$ MHz (equation 4.6).

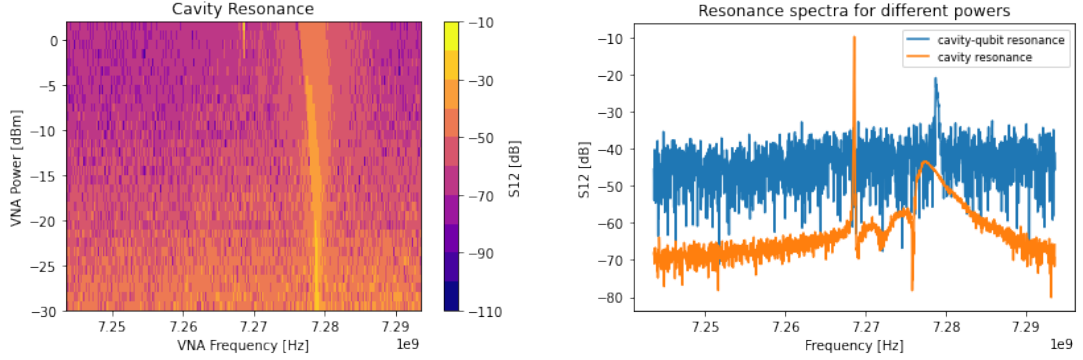


Figure 4.3: Left: resonance absorption spectra S21 (horizontal axis) for different power of the probe. Right: the S21 spectra at the lower (blue) and the higher VNA power (orange).

Qubit spectroscopy

In this case we implement a two tones qubit spectroscopy [23]. The first tone is given by a probe signal with a fixed power and a fixed frequency at the cavity frequency ω'_c . The second tone is a pump signal at the qubit frequency ω_{01} , that changes the state of the qubit between $|0\rangle$ and $|1\rangle$.

Again, for this measurements we rewrite the Hamiltonian but from the qubit point of view:

$$H_q = \hbar(\omega_c - \frac{\chi_{12}}{2})b^\dagger b + \frac{\hbar}{2}(\omega_{01} + \chi_{01} + 2\chi b^\dagger b)\sigma_z \quad (4.7)$$

The state of the qubit σ_z and the photons number $N = b^\dagger b$ inside the cavity are multiplied, where N depends on the power of the probe signal [23]. On one hand, as shown by Equation 4.5, the cavity frequency is influenced by the state of the qubit: the frequency shifts by 2χ when the qubit changes from ground to excited state. On the other hand, as shown in Equation 4.7, the qubit frequency shifts by $2N\chi$.

The figure 4.4(left) displays the transmission spectra as a function of the pump frequency. These spectra are obtained with the VNA measuring the transmission

near the dressed cavity frequency, for various pump frequency values.

The transmission peaks exhibit drops when the pump signal is resonant with the qubit. Indeed, this induces Rabi oscillation of the qubit, which shifts the cavity resonance. Moreover, the qubit frequency shifts depending on the number of photons inside the cavity, and thus on the probe power. As a consequence, we observe different drops corresponding to the various frequencies shift of the qubit.

The plot in Figure 4.4b show a section of Figure 4.4a, where we observe the transmission drops. In general if the total dispersive shift is $2N\chi$, the shift between every drop is 2χ , in this way measuring the frequency difference between two consecutive drops we are able to determine the value of the dispersive shift χ . We calculate χ taking the frequency difference between all nearby peaks and taking the mean value of this differences. The value of the dispersive shift is $\chi/2\pi = -3.42$ MHz. We see this shift dependence of the qubit frequency on N , calculating the energy level in the Hamiltonian:

$$\begin{aligned} E_{n=0} &= \frac{\hbar}{2}(\omega_{01} + \chi_{01}) \\ E_{n=1} &= \frac{\hbar}{2}(\omega_{01} + \chi_{01} + 2\chi) \\ E_{n=2} &= \frac{\hbar}{2}(\omega_{01} + \chi_{01} + 4\chi) \\ &\vdots \\ E_{n=N} &= \frac{\hbar}{2}(\omega_{01} + \chi_{01} + 2N\chi) \end{aligned}$$

making the difference $E_n - E_{n=0}$ we find the total shift in frequency $2N\chi$, while making the difference between two nearby levels we find the frequency shift 2χ .

The first drop of figure 4.4(right) corresponds to the energy without terms depending on $b^\dagger b$. Interpolating with a Lorentzian function the we obtain $(\omega_{01} - \chi_{01})/2\pi = 6.419$ GHz with ω_{01} the non-shifted frequency of the qubit. Combining χ with equation 4.6 we estimate $\chi_{12}/2\pi = -13.6 \pm 0.3$ MHz. The coupling $\chi_{01}/2\pi = (\chi + \frac{\chi_{12}}{2})/2\pi = -10.2 \pm 0.2$ MHz. The qubit frequency is $\nu_{01} = \omega_{01}/2\pi = 6.429$ GHz.

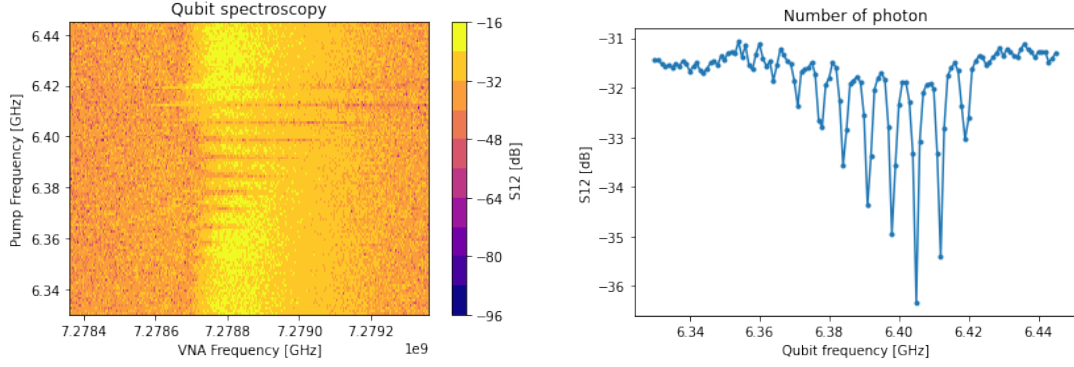


Figure 4.4: Left: spectra S21 as a function of the probe signal (vertical axis) and of the pump. Right: a mean of the vertical spectra in right figure.

From the spectroscopy we are able to estimate other parameters from the Hamiltonian 4.1. The value of $\Delta_{01}/2\pi = \nu_{01} - \nu_c = -839$ MHz and coupling $g_{01}/2\pi = \sqrt{\chi_{01}}\Delta_{01}/2\pi = 92.5 \pm 1$ MHz. The coupling for the 2nd and 3rd levels is [15] $g_{12}/2\pi = g_{01}\sqrt{2}/2\pi = 152$ MHz and $\Delta_{12}/2\pi = g_{12}^2/(\chi_{12}2\pi) = 1260$ MHz. The anharmonicity is given by

$$\alpha = (\Delta_{01} - \Delta_{12})/2\pi = \nu_{01} - \nu_{12} = 421 \pm 40 \text{ MHz} \quad (4.8)$$

The capacity of the qubit is given inverting the relation

$$h\alpha = E_c = \frac{e^2}{2C} \quad (4.9)$$

therefore $C = \frac{e^2}{2\alpha h} = 46 \pm 5$ fF. We estimate also the critical current I_0 and the Josephson inductance L_0 using the definitions of Φ_0 , E_c (equation 2.20) and E_j (equation 2.7):

$$I_0 = (2\pi E_j)/\Phi_0 = 25 \text{ nA} \quad \text{and} \quad L_0 = \Phi_0/(2\pi I_0) = 13 \text{ nH} \quad (4.10)$$

4.2.3 Time domain transmon characterization

Unlike the spectroscopy measurements where we constantly send signals and measure the scattering parameters, in time domain measurements we need to carefully send signals to the system with accurate timing and proper duration. It is important to define two different type of signals:

- The driving (or excitation) pulse: this pulse is sent at the qubit frequency and it is needed to control the qubit. The pulse drive (excite) the qubit to the eigenmode states or to a superposition of them.

- The readout pulse: it is sent at the cavity frequency. This pulse does not change the qubit state but it works on the cavity and allow us to measure the readout, i.e. the I and Q signals.

The principal experiments for the time domain characterization are the Rabi oscillation experiment, in which we determine the correct driving pulse for the qubit, the Ramsey characterization to extract the decoherence time T_2 , and the T_1 measurement, to extract the lifetime of the qubit T_1 .

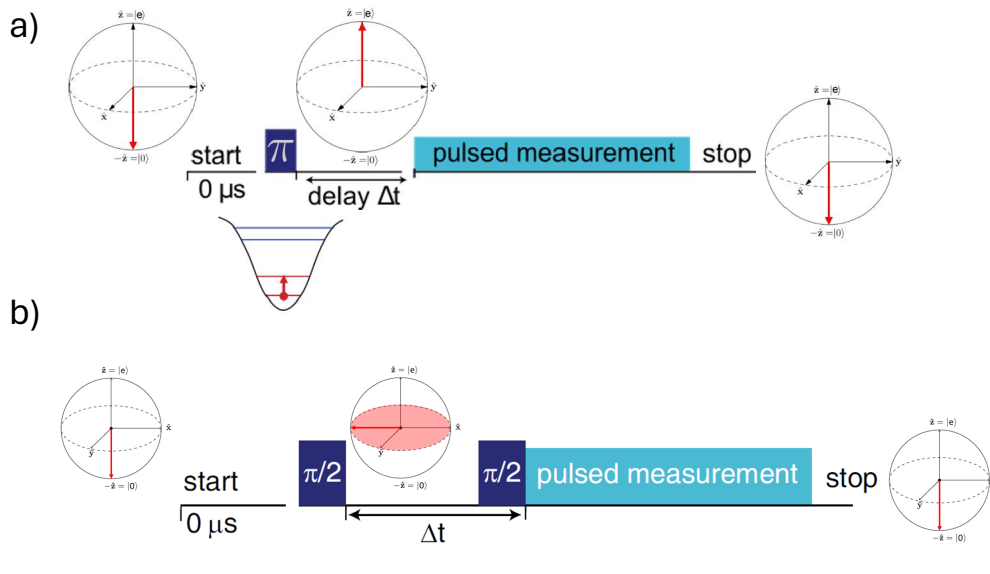


Figure 4.5: A scheme of (a) the T_1 measurement and (b) the Ramsey measurements.

Rabi Characterization

From the Rabi characterization, we define the key parameters for qubit control. This technique determines the appropriate driving pulse to transition the qubit from $|0\rangle$ to $|1\rangle$ (a π -pulse), or into the superposition state $|\psi\rangle = \frac{|0\rangle+|1\rangle}{2}$ (a $\frac{\pi}{2}$ -pulse), where $|0\rangle$ and $|1\rangle$ contribute equally. The driving pulse is characterized by its amplitude, determined by the signal power, and its duration. The Rabi measurements we conduct involve several steps, wherein we vary the pulse duration while keeping the amplitude constant, or vary the amplitude while maintaining a fixed pulse duration.

The steps are as follows:

1. Taking the qubit in the $|0\rangle$ state.
2. Exciting the qubit for different time lengths at a fixed power (or different power at the same time length) of the driving pulse.

3. Waiting a time t .
4. Measuring the readout.

Examples of Rabi oscillations are shown in Figure 4.6 (up-right and down-right), derived respectively from the Chevron plot and from the plot with different powers, explained below. The Rabi oscillation readout is given by the amplitude of the signal measured from the I and Q mixer outputs as $AMP = \sqrt{I^2 + Q^2}$ as a function of the time. Every point of the graph is obtained by exciting the qubit with the same pulse repeatedly and considering a mean value. This corresponds to having a mean of the count of the qubit excites in $|1\rangle$ or stays in $|0\rangle$ at a precise t after the pulse, seen as a probability of the qubit excitation. The amplitude is interpreted as the ground state population P_g , where the higher value of AMP corresponds to $P_g = 1$, and the lowest one to $P_g = 0$.

Figure 4.6 (upper-left) shows the Chevron plot of the Rabi measurements. This is taken by measuring different Rabi oscillations for different pulse frequencies with the same signal power. As we expected, no Rabi oscillations occur when moving away from the qubit frequency. On the other hand, Figure 4.6 (lower-left) represents the Rabi oscillations as a function of the signal power. These plots are made by measuring the Rabi oscillation for different powers at the qubit frequency $\nu = 6.419$ GHz. Examining the oscillation, the correct pulse for driving the qubit is chosen.

T1 measurements

From the Rabi analysis, we have obtained all the necessary information to control and drive the qubit. The next step is to determine the lifetime of the qubit, denoted as T_1 .

The experiment to estimate T_1 involves the following steps, as illustrated in Figure 4.5(a):

1. Exciting the qubit from the state $|0\rangle$ to $|1\rangle$ with a π -pulse.
2. Waiting for a certain delay time Δt between the π -pulse and the readout pulse, which varies for each repetition.
3. Measuring the ground state population.

Similar to the Rabi characterization, the ground state population P_g is derived from the I and Q output signals.

The purpose of this measurement is to drive the qubit to the excited state and observe its return to the ground state. The time taken for this return represents the total lifetime of the qubit. Figure 4.7 illustrates an example of T1 measurements, where we extract T_1 by fitting the curve as an exponential decay. In this instance, we find the value $T_1 = 8.68 \pm 0.82 \mu\text{s}$.

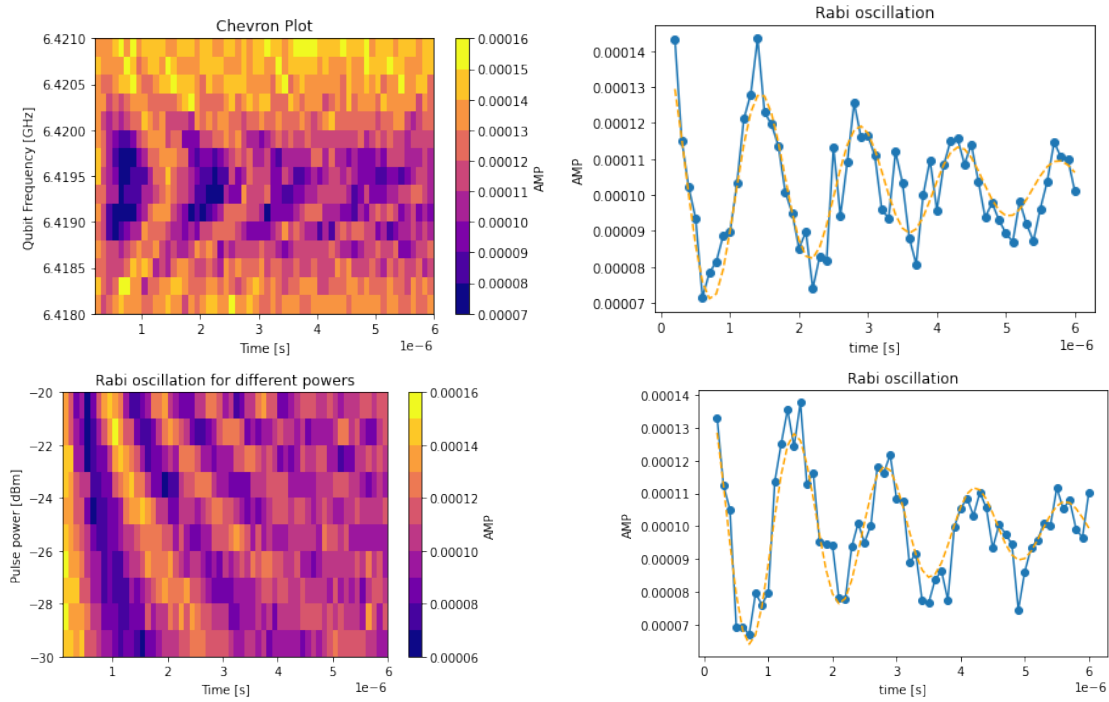


Figure 4.6: (up-left): Chevron plot acquired with excitation power $P = -93$ dBm. (down-left): Rabi oscillation dependence on the excitation tone power, with excitation frequency = 6.419 GHz. On the right are examples of Rabi oscillation extracted from the left graphs. The y-axis represents the amplitude of the signal, and the x-axis represents the delay time between excitation pulse and qubit readout.

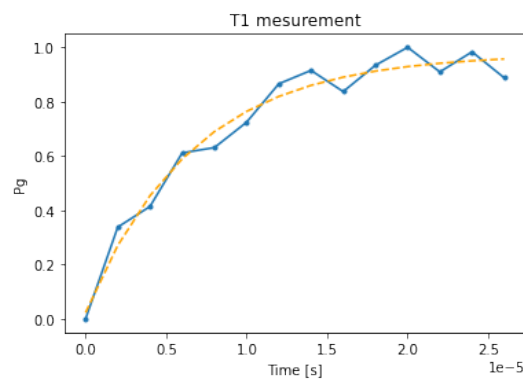


Figure 4.7: T1 measurements, with the state population on the y-axis and the delay time after the π -pulse on the x-axis.

Ramsey Characterization

Ramsey measurements are conducted to determine the decoherence time T_2 . For this type of measurement, we drive the qubit with two $\frac{\pi}{2}$ -pulses separated by a certain delay time Δt , as illustrated in Figure 4.5(b). The steps for each repetition are as follows:

1. Driving the qubit to the superposition state $|\psi\rangle = \frac{|0\rangle+|1\rangle}{2}$ with a $\frac{\pi}{2}$ -pulse.
2. Waiting for a certain delay time Δt , which varies for each repetition.
3. Driving the qubit with another $\frac{\pi}{2}$ -pulse to return it to another eigenstate.
4. Measuring the ground state population P_g .

Similar to the Rabi experiment, P_g is obtained from the I and Q outputs.

After the first $\frac{\pi}{2}$ -pulse, the qubit begins to precess on the Bloch sphere until the second $\frac{\pi}{2}$ -pulse brings it to another eigenstate. With a perfectly calibrated driving pulse (at the same frequency as the qubit), we expect an exponential decay due to decoherence with characteristic time T_2 , as shown in Figure 4.8(up-left). If the driving frequency is detuned from the qubit frequency, we observe an exponential decay convoluted with a sinusoid (Figure 4.8(down) and (up-right)). By interpolating the graphs and averaging the values, we obtain an estimate of $T_2 = 2.30 \pm 0.11 \mu s$.

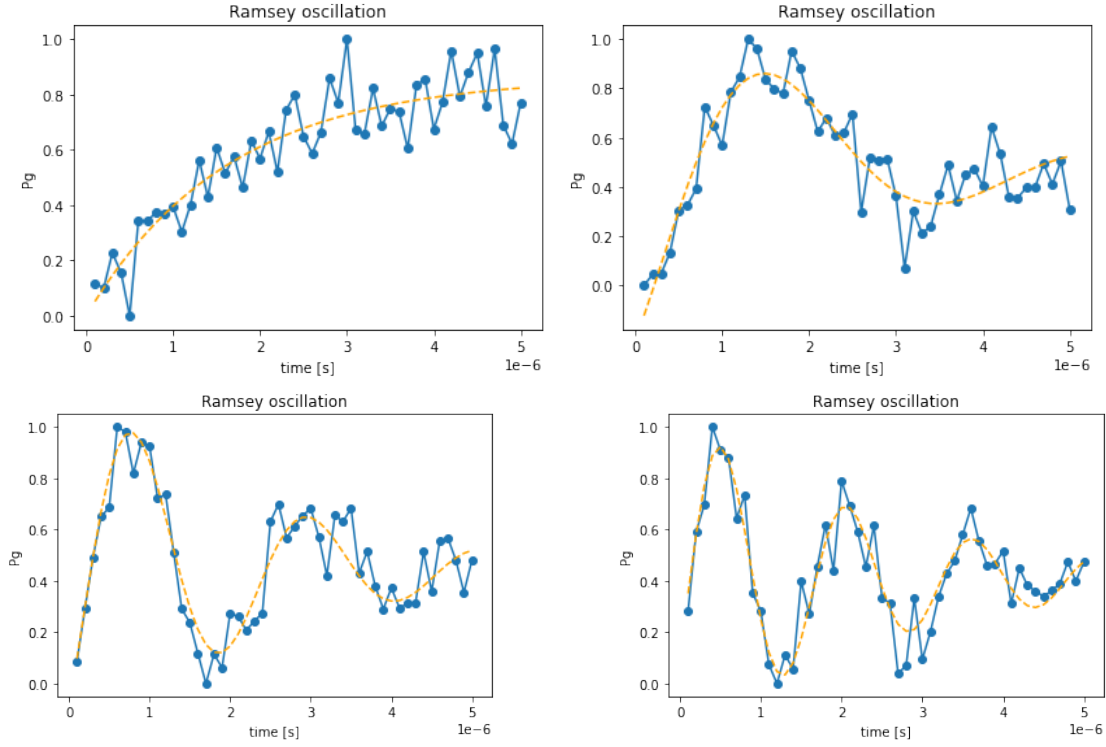


Figure 4.8: Ramsey oscillation for a pulse on resonance (up-left) and for detuned pulses. The detuning between the driving frequency and the qubit frequency is (up-right) 200 kHz, (down-left) 400 kHz, (down-right) 600 kHz. The y-axis represents the ground state population P_g , and the x-axis represents the delay time between the two $\frac{\pi}{2}$ -pulses.

From T_1 and T_2 , we calculate the pure dephasing time T_φ using the relation: $T_\varphi^{-1} = T_2^{-1} - \frac{T_1^{-1}}{2}$. We obtain $T_\varphi = 2.65 \pm 0.15 \mu\text{s}$. Table 4.1 summarizes the results obtained from the qubit characterization.

Variables	Values
$\chi/2\pi[MHz]$	-3.41 ± 0.08
$\chi_{01}/2\pi[MHz]$	-10.2 ± 0.2
$\chi_{12}/2\pi[MHz]$	-13.6 ± 0.3
$\alpha[MHz]$	421 ± 84
$g_{01}/2\pi[MHz]$	92.5 ± 1
$C[fF]$	46 ± 5
$T_1[\mu s]$	8.68 ± 0.72
$T_2[\mu s]$	2.30 ± 0.11
$T_\phi[\mu s]$	2.65 ± 0.15
$L_0[nH]$	13 ± 2
$I_0[nA]$	24.7 ± 1.3

Table 4.1: Summary of the experimental qubit-cavity parameters

4.3 DC characterization of Josephson junctions

In this section we describe the setup used to characterize Josephson junctions. In particular, the aim is to find the critical current I_0 of the JJ and prepare the setup used to find the I_0 of the transmon qubit in the next section.

The sample is a chip composed of several JJs that are set on the sample holder as shown in Figure 4.9. The fabrication process and images of single junctions are shown in Section 2.7.1.

In this case, we consider only 4 JJs. As shown in Figure 4.10, the junctions are connected to the PCB of the sample holder using 10 wires, each bonded at the head of a junction. Each wire corresponds to a different channel, totaling 10 channels, which are utilized to study the current (I) and the potential (V) across the junctions. Two wires are linked to one head of each junction j , corresponding to channels V_j^+ and current I_j^+ . Conversely, two wires are connected to the other head and are common for all junctions, corresponding to channels V^- and I^- .

The holder PCB is connected to two USB-C ports and every pin of the USB-C corresponding to a channel of the JJs. The measure of the JJs is made in two different environments. The results are summed in Table 4.2.

- At low temperature ($T = 15$ mK), we study the I-V characteristic in order to measure the critical current I_c , the retrapping current I_r , the critical voltage V_c and make an estimation of the normal resistance R_0 .
- At room temperature ($T = 300$ K), we measure the normal resistance R_0 .

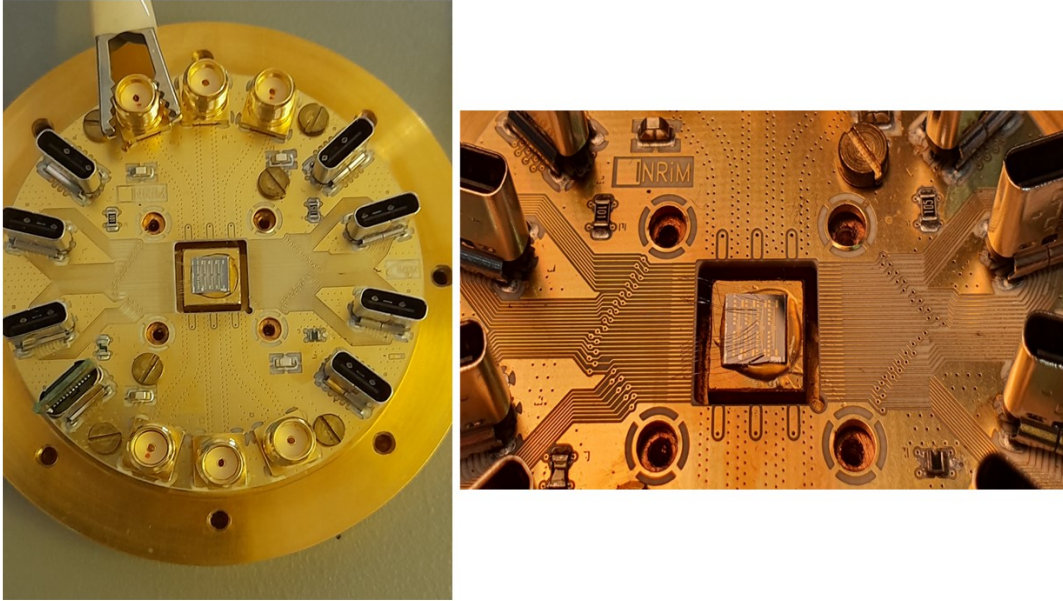


Figure 4.9: The image shows the chip with the measured junctions placed on the sample holder. There are a total of 8 USB-C connectors on the sample holder, but we only use the two in the middle on the left side.

Low temperature measurements

The experimental setup at low temperature is shown in Figure 4.11 (left). The measurements are made by biasing the JJs with a DC current, provided by a waveform generator (KEYSIGHT 33500B) set at a frequency of $f = 62.8$ Hz. At room temperature, a resistance of $R = 1$ k Ω is set to measure the bias current. The sample holder with the junctions is placed inside the cryostat at the 10 mK plate. The USB ports are coupled with two PCBs that connect the junctions to the external environment. The input signal is filtered at 300 K and 4 K using two low-pass filters with a 100 kHz cut-off frequency. The output signal is amplified by two Stanford Preamplifiers and acquired with a 16-bit ADC board at a rate of 1 MS/s.

The value of the current is calculated by measuring the voltage across the resistance. It is given by $I = \frac{\Delta V}{R}$, where ΔV is the voltage difference across the resistance. For every junction j , the current flows from the channel I_j^+ to I_j^- , and the voltage is measured as the difference between potential at V_j^+ and V_j^- channels.

For every junction, we measure the I-V characteristics several times to perform a statistical analysis. From each cycle, we extract the principal parameters. Since the IVC is symmetric, we study the parameter values in the first quarter of the

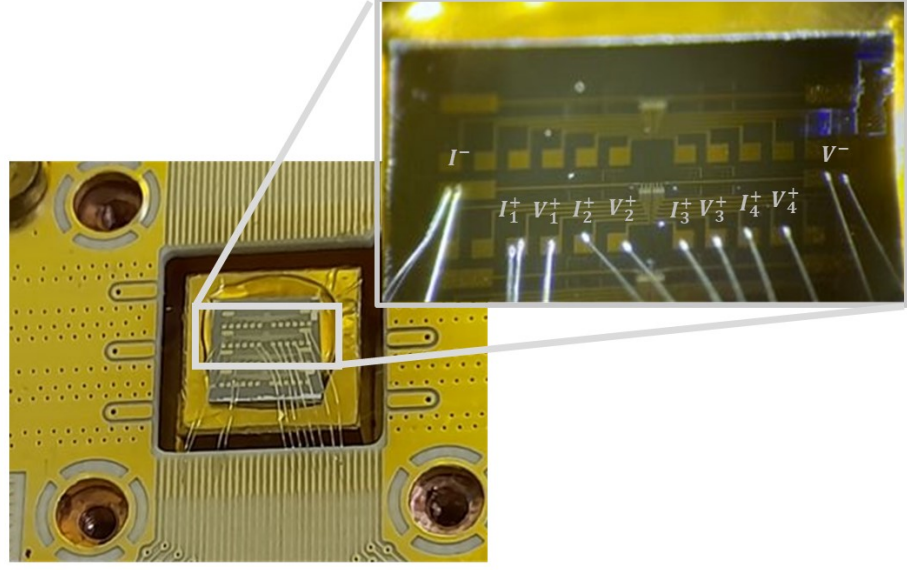


Figure 4.10: Image of the junctions and pin connections. The four JJs are connected via 10 bondings from the junctions to the PCB of the sample holder. Each bonding corresponds to a different channel.

graph and the absolute values of the parameters in the third quarter to increase the statistics. The IVC of the second junction is shown in Figure 4.13. The I and V signals, along with a single cycle of the signal as a function of time, are shown in Figure 4.12.

In Figures 4.13 and 4.12, the blue crosses/lines represent the critical current value I_0 , the red ones represent the retrapping current I_r , and the green ones represent the critical voltage V_c . Referring to Figure 4.13, the values of I_0 and I_c are determined when the voltage exceeds a certain threshold, defined as $200 \mu\text{m}$, located in the middle of the voltage range between zero and the maximum value of the voltage. The value of V_c is identified as the minimum in the upper part, aimed at avoiding self-heating which could inflate the actual value.

The normal resistance R_0 , depicted by the yellow line, is calculated as the ratio between the voltage difference and the current difference between the points of maximum and minimum potential, expressed as:

$$R_0 = \frac{V_{\max} - V_{\min}}{I_{\max} - I_{\min}} \quad (4.11)$$

The parameter values are summarized in Table 4.2.

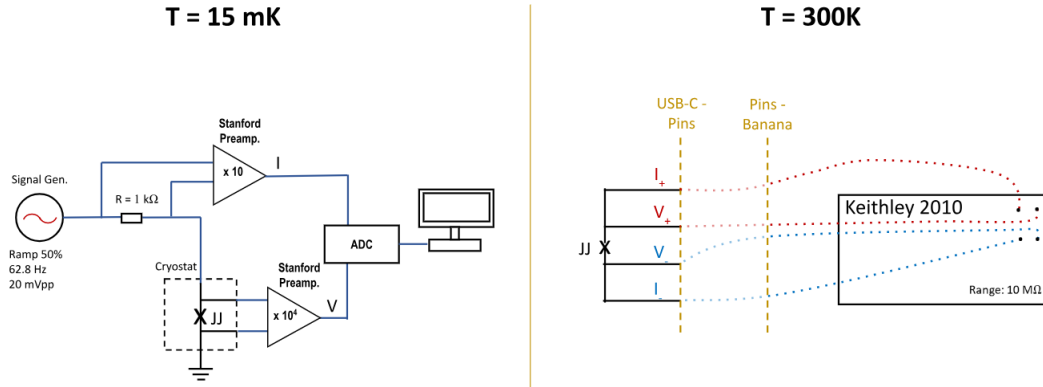


Figure 4.11: Experimental setup at low temperature (left) and at room temperature (right).

Room temperature measurements

At room temperature, the 4-probe measurements are conducted using the Keithley 2010 Multimeter. The experimental setup at low temperature is depicted in Figure 4.11(right). The junctions are biased by a DC current I_{DC} , the voltage difference across the junction, $\Delta V = V_+ - V_-$ is measured with two cables specially designed to ensure stable contact from pins to banana entries. The ratio between these values yields the normal resistance of the junctions, $R_0 = \frac{\Delta V}{I_{DC}}$. The values of R_0 are listed in the second-last column of Table 4.2. Except for the first junction, the normal resistance R_0 measured at room temperature closely matches the resistance measured at low temperature.

We estimate the value of the critical current of the junction from the resistance measured at room temperature with the Ambegaokar-Baratoff formula. It is given by Equation 2.4 at $T = 0$: $I_0(0) = \frac{\pi \Delta(0)}{2eR_0} = \frac{\pi}{4} \frac{V_c}{R_0}$. The value of V_c does not depend on the oxidation of the JJ and it is nearly constant for junctions of the same dimension. Considering $V_c = 340 \mu\text{V}$, an estimation of the I_0 for each junction is reported in the last column of Table 4.2. Except for the first junction, the values are compatible.

	$I_0[\mu\text{A}]$	$I_r[\mu\text{A}]$	$V_c[\mu\text{V}]$	$R_0^{(15\text{mK})}[\Omega]$	$R_0^{(300\text{K})}[\Omega]$	$I_0^{est} [\mu\text{A}]$
JJ1	3.0 ± 0.2	0.38 ± 0.07	328 ± 3	73 ± 1	28	9.5
JJ2	2.9 ± 0.2	0.28 ± 0.06	340 ± 2	82 ± 1	87	3.1
JJ3	1.7 ± 0.1	0.03 ± 0.01	340 ± 3	114 ± 3	113	2.4
JJ4	1.8 ± 0.1	0.11 ± 0.03	348 ± 3	124 ± 2	115	2.3

Table 4.2: Principal parameters estimated of the Josephson junctions

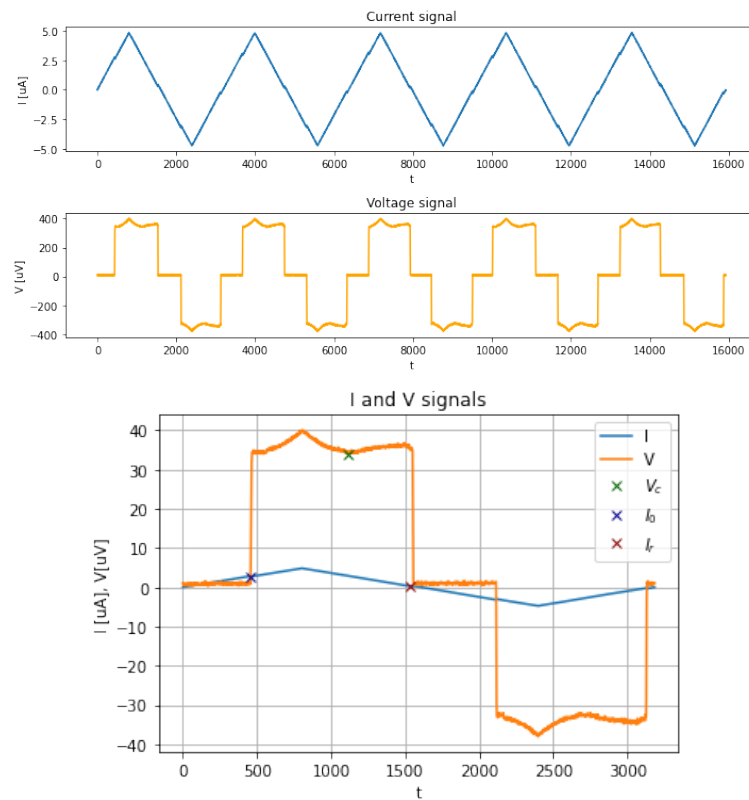


Figure 4.12: (upper) Total current and voltage signal. (lower) A single cycle of the I and V signal. This figure is used to estimate the principal values of the JJ. The value of the voltage is $10\times$, this is done for visual reason, to compared it with the current signal.

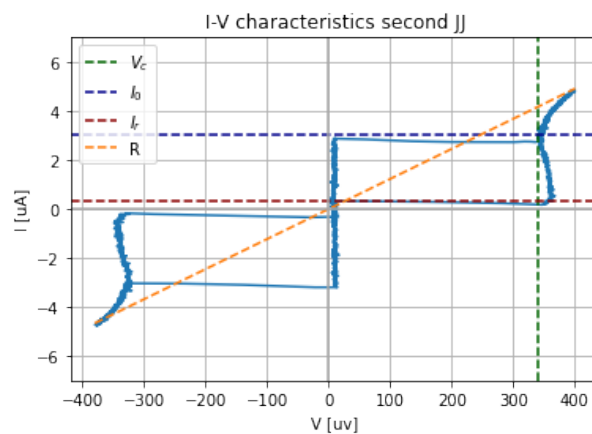


Figure 4.13: I-V charateristics for the second JJ. The lines represent the value of the parameters on the positive region. The parameters extracte are reported in table 4.2.

4.4 DC characterization of the circular qubit

In this section, we describe the DC current measurement with the new circular qubit discussed in Section 2.7.3 and fabricated at INFN-CNR. The details of the dimensions and parameters are listed in Table 3.2. The aim of this measurement is to determine the value of the critical current of the qubit I_0 , important to estimate the resonant frequency of the qubit. The setup is identical to that described in Figure 4.11 (left), with the addition of a filter at 10 mK.

Two qubits are placed on the sample holder, and the conductive pads are bonded to the holder with 8 connections: two for each pad of the two qubits. These connections are used for the 4-wire measurements of current for current I and potential V . Specifically, I_1^+ , V_1^+ , I_1^- , and V_1^- represent the current and potential of the upper pad (+) and the bottom pad (-) for the first qubit. Similarly, I_2^+ , V_2^+ , I_2^- , and V_2^- are the connections for the second qubit. The I and V are linked to two USB-C connections on the sample holder, one for each qubit. The sample holder is placed on the mixing chamber at 10 mK in the cryostat. The USB-C ports are connected to two PCBs; the wires of the PCBs are connected to the filter placed at the 10 mK plate of the cryostat. Afterward, the device is connected to the ADC boards through twisted and coaxial cables. An image of the devices is shown in Figure 4.14, and details about the connections are shown in Figure 4.15.

Regarding the JJ, the current I is measured by taking the potential difference across the resistance $R = 1 \text{ k}\Omega$ and making the ratio between this value and the resistance. The device is biased with the current through the I channels, and the measurement of the potential difference across each qubit is made through the V channels.

This measurements highlighted a problem in the JJ fabrication. In fact, one qubit behaves as a short circuit and the second as an open one. The chip fabrication will be repeated soon as well as the critical current characterization. Moreover, once the we will have working devices, the characterization at room temperature will also be repeated, this will allow us to give a fast feedback to tune the fabrication process, in particular the oxidation time, in order to fabricate the JJs with the desired critical current, and therefore the qubit resonating frequency of the design.

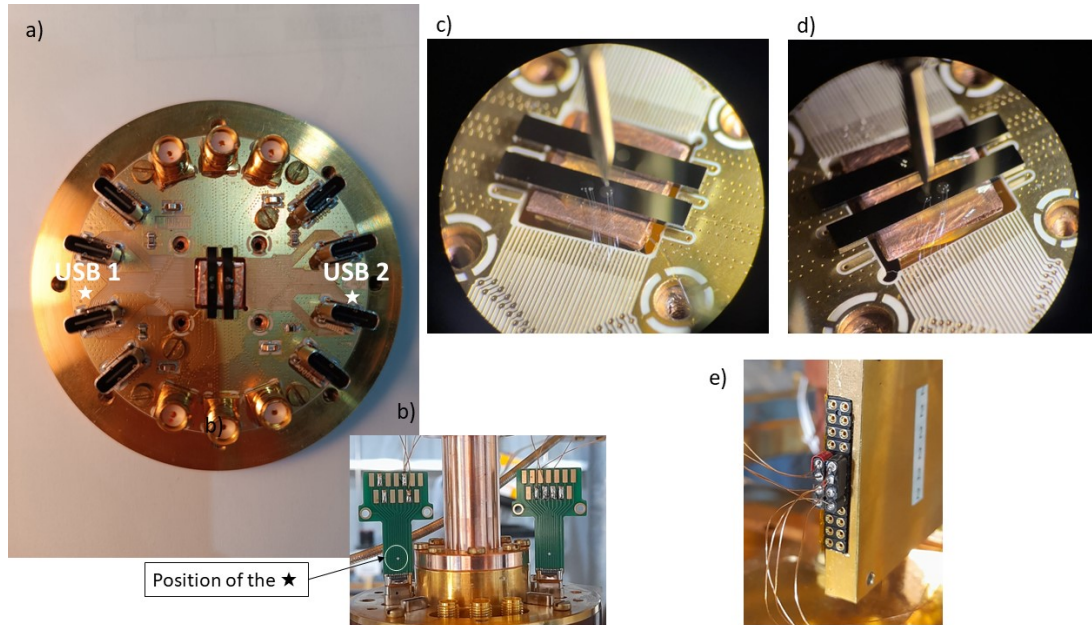


Figure 4.14: (a) The sample holder of the qubits in which USB-C connectors for the PCBs are mounted. (b) The PCBs connected to the holders USB. Wires connect the PCBs to the 10 mK filter. The star on figure a) and on the PCBs is used to identify the correct position of the PCBs. (c) and (d) show the bonding between the qubit pads and the holder, (c) connected USB1 and (d) to USB2. (e) The connection between the PCBs and the 10 mK filter. In figures (c) and (d), we define the lines that connect the pads to the sample holder starting counting from the left. More details about connections are provided in Figure 4.15.

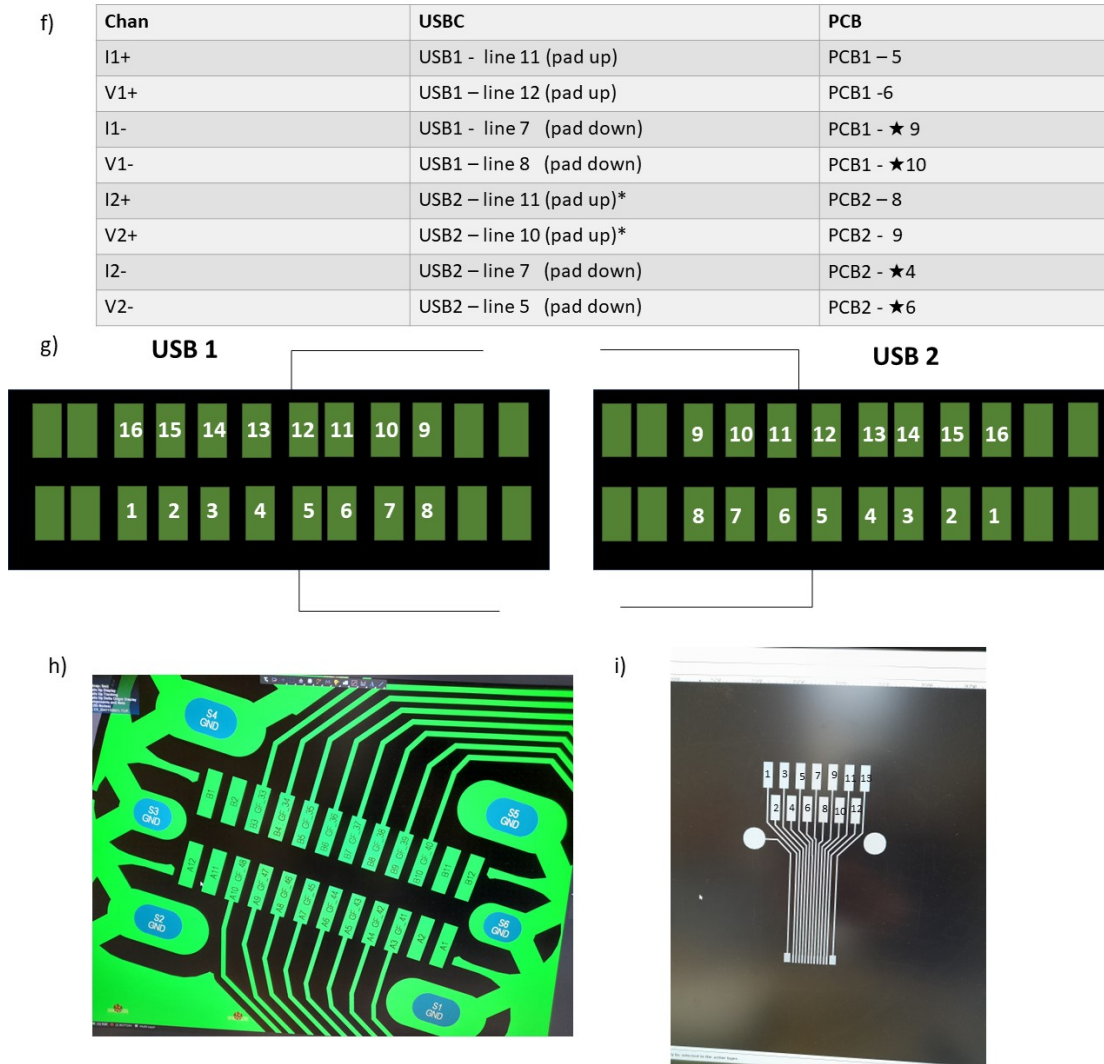


Figure 4.15: The qubits are bounded to the PCB of the sample holder with a precise line, counted from the left of the holder. The lines are connected to two USB-Cs connectors, one for every qubit. The USB-Cs are coupled with two PCBs that relates the device to the external environment. (f) The table that defines the connections. The first column refers to the channel, the second column defines the correlation between the lines of the of sample holder PCB with the ports of the USB1 and USB2. The scheme of the connection of the USB pins and the lines of the sample holder is represented in (g), the green rectangles correspond to the USB pins and the numbers refer to the lines. The third column refers to the corresponding port of the PCB1 and PCB2 coupled respectively to USB1 and USB2. The figure (i) pictured the scheme of the PCB ports. The information of the third column is the number of the PCB (PCB1 or PCB2) and the number of the pin of the PCB, as shown in (i). The star define what side of the PCB we consider. The PCB is after connected to the 10 mK filter. Figure (h) is a real scheme of a USB port.

Chapter 5

Conclusion

In this thesis work, we provide a complete characterization of the transmon qubit fabricated in Abu Dhabi, effectively extracting the parameters that describe it with a qubit and cavity spectroscopy and a time domain characterization. These parameters include the capacity between the pads $C^{\text{exp}} = 46 \pm 5$ fF, the critical current of the junction $I_0^{\text{exp}} = 25 \pm 1$ nA, the qubit-cavity coupling $g_{01}^{\text{exp}}/2\pi = 93 \pm 1$ MHz, and the lifetime $T_1^{\text{exp}} = 8.7 \pm 0.7$ μ s.

After, we develop a method to extract similar information using electromagnetic simulation with ANSYS software. Specifically, we investigate electromagnetic losses on the device that decrease the coherence of the qubit, providing a quantitative description by calculating the sum of participation ratios contributions from different spatial regions. The parameters extracted from simulations are the pads capacity $C^{\text{sim}} = 56$ fF, the qubit-cavity coupling $g_{01}^{\text{sim}}/2\pi = 97$ MHz, and the lifetime $T_1^{\text{sim}} = 42$ μ s.

We compare the parameters extracted from the experimental analysis with the simulations, noting compatibility in the values of capacitance and coupling constant, while the simulated lifetime differs substantially. This discrepancy may originate from an underestimation of the participation ratios due to limitations in our numerical mesh resolution. Currently, we are exploring potential solutions proposed in [18] and [21].

Starting with the Abu Dhabi qubit design, we modify the shape and size of the pads and explore other simple geometric shapes. Analyzing the distribution of the electromagnetic field, we observe significant field concentration at the corners of the pads, leading to increased total electromagnetic losses. To address this, we smooth the corners of the pads and add non-straight lines to increase the area, achieving a better distribution of the field.

A geometry with two circular pads is selected. The pads are circles with a radius of 500 μ m and a distance of 243 μ m between the circumference of the pad and the center of the Josephson junction. The junction has an inductance $L = 7.8$ nH, corresponding to a critical current $I_c = 42$ nA. The total capacity is $C = 93$ fF,

and the qubit-cavity coupling is $g_{01}/2\pi = 355$ MHz. The relaxation time is $T_1 = 63$ μ s, higher than the simulated time for the Abu Dhabi qubit ($T_1^{(\text{Abu Dhabi})} = 42$ μ s). The larger pad dimensions allow for greater distribution of the electromagnetic field, resulting in a significant reduction in losses. The new design presents a loss of $P = 0.3 \cdot P^{(\text{Abu Dhabi})}$. However, the results for the losses are still imprecise, and we are currently adjusting the mesh resolution to improve the accuracy of the loss values.

A parallel study is also conducted by implementing DC measurements to extract the principal parameters from four Josephson junctions fabricated at CNF-IFN in Rome. We extract values from the IVC of the junctions, and the results are shown in Table 4.2. We find critical current values of a few μ A, critical potential of hundreds of μ V, and junction normal resistance of tens of ohms. We compare the resistance value with a 4-probe measurement made at room temperature and find good agreement for 3 of the 4 junctions, making this a reliable method for characterizing large junctions at room temperature.

The same measurements are made for two qubits fabricated at CNR-IFN in Rome with the circular design proposed, highlighting a problem in the JJ fabrication: one qubit behaves as a short circuit and the second as an open one. The chip fabrication will be repeated soon as well as the critical current characterization. The aim is to give a fast feedback to tune the fabrication process and produce JJs with the desired critical current and as a consequence, the qubit resonating frequency.

Bibliography

1. Kjaergaard, M. *et al.* Superconducting qubits: Current state of play. *Annual Review of Condensed Matter Physics* **11**, 369–395 (2020).
2. D’Elia, A. *et al.* Stepping closer to pulsed single microwave photon detectors for axions search. *IEEE Transactions on Applied Superconductivity* **33**, 1–9 (2022).
3. Rettaroli, A. *et al.* Josephson junctions as single microwave photon counters: Simulation and characterization. *Instruments* **5**, 25 (2021).
4. Chen, S. *et al.* Detection of hidden photon dark matter using the direct excitation of transmon qubits. *International Center for Elementary Particle Physics (ICEPP), The University of Tokyo, 7-3-1 Hongo, Bunkyo-ku, Tokyo 113-0033, Japan* (2019).
5. Martinis, J. M. Superconducting phase qubits. *Quantum information processing* **8**, 81–103 (2009).
6. Wang, C. *et al.* Towards practical quantum computers: Transmon qubit with a lifetime approaching 0.5 milliseconds. *npj Quantum Information* **8**, 3 (2022).
7. Likharev, K. K. *Dynamics of Josephson Junctions and Circuits* (Gordon and Breach Science Publishers, 1986).
8. Ambegaokar, V. & Baratoff, A. Tunneling between superconductors. *Phys. Rev. Lett.* **10**, 486–489 (1963).
9. Gross, R. & Marx, A. *Applied Superconductivity: Josephson Effect and Superconducting Electronics* © Walther-Meißner-Institut —Garching (Oct. 2005).
10. Lisenfeld, J. Experiments on superconducting Josephson phase quantum bits /, 9–14.
11. Krantz, P. *et al.* A Quantum Engineer’s Guide to Superconducting Qubits. *Research Laboratory of Electronics, Massachusetts Institute of Technology, Cambridge, MA 02139, USA* (2020).
12. Vool, U. & Devoret, M. H. Introduction to Quantum Electromagnetic Circuits. eprint: [arXiv:1610.03438](https://arxiv.org/abs/1610.03438) (2017).
13. Naghiloo, M. & Lab, M. Introduction to Experimental Quantum Measurement with Superconducting Qubits. *Washington University in St. Louis* (Apr. 2019).
14. Pozar, D. M. *Microwave Engineering* (John Wiley & Sons, 2011).

15. Koch, J. *et al.* Charge-insensitive qubit design derived from the Cooper pair box. *Phys. Rev. A* **76**, 042319. <https://link.aps.org/doi/10.1103/PhysRevA.76.042319> (4 Oct. 2007).
16. Miller, S. *A tunable 20 GHz transmon qubit in a 3D cavity* Semester Thesis. Zurich, June 2018.
17. Wenner, J. *et al.* Surface loss simulations of superconducting coplanar waveguide resonators. *Applied Physics Letters* **99**. Department of Physics, Zhejiang University, Hangzhou 310027, China, 113507 (July 26, 2011).
18. Martinis, J. M. Surface loss calculations and design of a superconducting transmon qubit with tapered wiring. *npj Quantum Information* **8**, 26. ISSN: 2056-6387. <https://doi.org/10.1038/s41534-022-00530-6> (Mar. 2022).
19. Deng, H. *et al.* Titanium Nitride Film on Sapphire Substrate with Low Dielectric Loss for Superconducting Qubits. *Journal of Applied Physics* **123**. Received 16 May 2022; revised 15 December 2022; accepted 11 January 2023; published 6 February 2023, 052208 (2023).
20. ANSYS, Inc. *HFSS Fields Calculator Cookbook* Release 17.0. ANSYS, Inc. (2015).
21. Wang, C. *et al.* Surface participation and dielectric loss in superconducting qubits. *Applied Physics Letters* **107**, 162601. ISSN: 0003-6951. <https://doi.org/10.1063/1.4934486> (Oct. 2015).
22. Gao, Y. Y., Rol, M. A., Touzard, S. & Wang, C. Practical guide for building superconducting quantum devices. *PRX Quantum* **2**, 040202 (2021).
23. Schuster, D. *et al.* Resolving photon number states in a superconducting circuit. *Nature* **445**, 515–518 (2007).